Institut für Festkörperphysik

FRIEDRICH-SCHILLER-UNIVERSITÄT JENA

Annual Report 2008

Institut für Festkörperphysik

Friedrich-Schiller-Universität Jena

Annual Report 2008

Editors: Prof. Dr. Paul Seidel
Prof. Dr. Carsten Ronning
Uta Bornkessel

Institut für Festkörperphysik
Friedrich-Schiller-Universität Jena
Max-Wien-Platz 1
D-07743 JENA

Tel.: +49 (0) 3641 / 947301, 947411
Fax: +49 (0) 3641 / 947302, 947412
e-mail: Paul.Seidel@uni-jena.de
home page: http://www.ifk.uni-jena.de/

Prof. Dr. Paul Seidel
director
Tel.: +49 (0) 3641 / 947410, 947411
Fax: +49 (0) 3641 / 947412
e-mail: Paul.Seidel@uni-jena.de
home page: http://www.physik.uni-jena.de/~tief

Prof. Dr. Carsten Ronning
Tel.: +49 (0) 3641 / 947300, 947301
Fax: +49 (0) 3641 / 947302
e-mail: carsten.ronning@uni-jena.de
home page: http://www.nano.uni-jena.de/

Prof. Dr. Werner Wesch
Tel.: +49 (0) 3641 / 947330, 947301
Fax: +49 (0) 3641 / 947302
e-mail: Werner.Wesch@uni-jena.de
home page: http://www.physik.uni-jena.de/~exphys/

Dr. Bernd Schröter
Tel.: +49 (0) 3641 / 947440, 947411
Fax: +49 (0) 3641 / 947442
e-mail: bernd.schroeter@uni-jena.de
home page: http://www.physik.uni-jena.de/~layer/

Prof. Dr. Friedrich Huisken
Tel.: +49 (0) 3641 / 947354, 947301
Fax: +49 (0) 3641 947308
e-mail: Friedrich.Huisken@uni-jena.de
home page: http://www.astrolab.uni-jena.de/

PD Dr. Heinrich Metzner
Tel.: +49(0) 3641 / 947 353
Fax: +49(0) 3641 / 947 302
e-mail: Heiner.Metzner@uni-jena.de
home page: http://www.physik.uni-jena.de/inst/exphys/

Preface

Since 1996 there is an annual report of the Institute of Solid-State Physics at the Friedrich Schiller University Jena available. The research and teaching activities achieved in 2008 will be summarized in this issue. For the first time there will be an electronically distributed version instead of a paper-printout. As the preceding reports the 2008 edition is addressed to the interested scientific community and to our colleagues within the university and from outside. We also document the use of the financial support and we would like to take the opportunity to thank all institutions for this support.

The research topics of the IFK cover different fields of solid state physics and range from fundamental questions to largely applied developments. The experimental solid state physics groups concentrate to new fields like semiconducting nanowires and diamond-like materials besides the traditional ion beam modification and analysis of semiconductors and optical materials. As topics LEDs and lasers were realized from nanowires. Research activities on chalcopyrite semiconductors and CdTe for thin-film solar cells and optoelectronic devices are performed in the CIS-lab of the institute. In the low temperature department essentially high-T_c superconducting layers and superconducting devices like SQUIDs are studied and applied. Numerous applications of low-Tc-SQUIDs in precision measurement technique provide important contributions for instance in high energy physics and fundamental physics. This includes the cooling technology with self made cryocoolers as well as ultra-low temperature research. We started to install a new helium refrigerator system to enhance the liquid helium production in 2009.

The SFB/TR7 “Gravitational wave astronomy” investigated materials for the optics of future cryogenic detectors. The main focus here is on low materials which provide a low thermal noise at temperatures below 20 K.

Thin films of metals and group-IV semiconductors (silicon, silicon carbide, germanium) are deposited by molecular beam epitaxy and are characterized by a variety of surface physics methods in the thin solid films group. As a common interest within our institute investigations on carbon and silicon nanotubes were forced within the last years. The research group on laboratory astrophysics/cluster physics is devoted to fundamental astrophysical questions that can be answered by laboratory experiments, with particular emphasis on spectroscopy. A topic was emission in Ge-doped silicon quantum dots.

The permanent scientific staff of the IFK is strongly involved in teaching duties. The modularisation of the physics courses and the new bachelor and master studies instead of the physics diploma give rise to strong enhancement of effort but also the chance of a new quality. The solid state physics in combination with the materials science will play an important role within this education.

Many institutions contributed to the scientific output of the institute. The activities would be impossible without substantial financial support - equipment as well as additional scientific and technical staff - by: Thüringer Kultusministerium (TKM), Bundesministerium für Bildung und Forschung (BMBF), Bundesministerium für Wirtschaft und Technologie (BMWi), Bundesministerium für Umwelt, Naturschutz und Reaktorsicherheit (BMU), Deutsche Forschungsgemeinschaft (DFG), Europäische Gemeinschaft (EU), Nagelschneider-Stiftung, Helmholtz-Zentrum Berlin, Gesellschaft für Schwerionenforschung Darmstadt (GSI), Deutsches Elektronensynchrotron Hamburg (DESY), industrial partners and - last but not least - the Friedrich-Schiller-Universität. We express our gratitude to all these institutions.

Prof. Dr. Paul Seidel

Contents

Departments of the institute

Experimental Solid State Physics

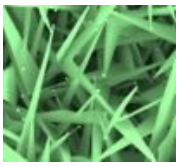

Prof. Dr. C. Ronning

- Synthesis, doping and functionization of semiconductor nanowires
- Semiconductor physics: doping using ion beams
- Growth and functionalization of diamond-like materials
- Ion beam analysis

Recent work of the research group in the field of semiconductor nanowires focuses both on the growth of desired nanostructures as well as on the modification of semiconductor nanowires for the use as photonic devices. This included in 2008 the successful realization of light-emitting diodes and the observation of laser oscillations within single ZnO nanowires. The latter results have been realized in collaboration with M.A. Zimmler and Prof. Dr. F. Capasso from the Harvard University – a collaboration, which will be intensified in 2009 and 2010 by the support of DAAD.

In the area of semiconductor nanowires the group holds further successful collaborations within the SPP-Program "Nanowires and Nanotubes" of the DFG. This includes PL-investigations of surface treated single ZnO nanowires together with Dr. T. Voss (Uni Bremen), life-time measurements of ZnS:Mn nanostructures with Prof. Dr. W. Heimbrodt (Univ. Marburg), the electrical doping of III-V-nanowires with Dr. W. Prost (Uni Duisburg), as well as the growth of desired nanostructures together with Prof. Dr. R. Adelung (U Kiel).

Besides those supported collaborations by funding agencies, the group works also on the electrical functionalization of Si nanowires for different kind of memory devices or solar cells together with Dr. A. Colli / Prof. Dr. A. Ferrari (University of Cambridge, UK) and PD Dr. S. Christiansen (IPHT Jena)

In the past year the group moved from Göttingen to Jena, which included not only the move of two nanowires growth systems, but also a low energy ion accelerator. This system will be build up in the first part of 2009, and will be used in future for the growth of diamond-like materials and their surface treatment. The biocompatibility and bioactivity of such thin films and the influence of both the structure and chemistry of the surface will be investigated soon.

Finally, it is worth to mention that the group also works in the area of ion beam doping of ZnO (in collaboration with Prof. Dr. M. Grundmann, Uni Leipzig) and the ion beam analysis of thin high-*k* materials (Dr. C. Wenger, IHP Frankfurt/Oder) and SiN passivation films for solar cells (CIS Erfurt).

Ion Beam Physics

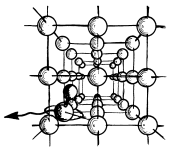

Prof. Dr. W. Wesch

- Modification of solids by ion implantation and succeeding processes and ion beam analysis (RBS, PIXE, ERD, NRA)
- Ion beam synthesis of buried nanostructures
- Investigation of the effect of high electronic excitation on structural modification of crystalline and amorphous semiconductors
- Simulation of processes of ion-solid interaction

The ***Ion Beam Physics*** Group deals with problems of modification of solids and synthesis of buried nanostructures by means of ion beams and combined secondary processes. The studies cover fundamental processes of ion-beam induced structural modification in new semiconductors and insulators being relevant for future electronic, optoelectronic and photonic device technologies, as e.g. ternary III-V semiconductors, wide gap semiconductors and insulators (collaborations with the Australian National University Canberra, the University of Pretoria, South Africa and the University Lisboa, Portugal). The structural changes in AlGaAs, Si and Ge caused by ion irradiation are also investigated by classical molecular dynamics computer simulations. At the same time the formation of ferromagnetic nanocrystals and layers in Si and GaAs by ion-beam induced non-equilibrium processes (collaboration with the University Aveiro, Portugal) and the specific modification of optical materials as $LiNbO_3$ and $KTiOPO_4$ as well as ion beam enhanced chemical etching to produce high aspect ratio microstructures for optical application of these materials (collaboration with the Institute of Applied Physics, Jena) are studied.

Beside these activities on materials modification utilizing ion beams with conventional energies (several 10 keV to several MeV), the effect of high electronic excitation under swift heavy ion irradiation (several 100 MeV) on structural modification of crystalline semiconductors (ion track formation) as well as on plastic deformation in amorphous semiconductors is studied in collaboration with the Australian National University Canberra (supported by the DAAD and the Australian Research Council).

Low Temperature Physics

Prof. Dr. P. Seidel

- Superconductivity within thin layers and layer systems
- Josephson effects, proximity effect, tunnel effects and quantum effects in superconducting devices
- DC-SQUID's and their application in measurement, e.g. biomagnetism, NDE, MRX
- cryogenic measurements on optical components (mechanical quality factor)
- Dynamics of superconducting Josephsonarrays and qubits
- cryogenic engineering (cryocoolers, cryogenic storage)

The ***low temperature physics*** group works on the following fields:

- preparation, characterization, modelling and application of Josephson junctions and SQUIDs (precision and magnetorelaxation measurements with LTS SQUIDs, non-destructive evaluation and biomagnetism with HTS SQUIDs, intrinsic Josephson junctions)
- low temperature physics and cryogenic engineering (development of new kinds of pulse tube cryocoolers, investigations on a new concept for regenerators, cryogenic storage)
- experimental work within the SFB/TR on cryogenic measurements of the Q-factor of optical components including grating optics
- thin film technologies for insulators and other materials

The research is carried out in cooperations with other research groups in Thuringia (TU Ilmenau, IPHT Jena, SQUID GmbH Jena, SUPRACON Jena, Polyoptik Bad Blankenburg, Innovent e.V. Jena). Within common activities the group works together with the Gesellschaft für Schwerionenforschung Darmstadt, DESY Hamburg, TARGET Systemelectronic GmbH Solingen and the Zentrum für Raumfahrttechnologie und Mikrogravitation Bremen.

With industrial partners there exist some resarch activies e.g. with Air Liquide (France), Northrop Gruman (USA), AEG Infrared Moduls GmbH Heilbronn and the TransMIT center for adaptive cryotechniques Gießen. A long tradition of co-operation exists with the Institute of Electrical Engineering (IEE) of the Slovak Academy of Sciences Bratislava, the Universities of Moscow (Russia), Kharkov (Ukraine), Glasgow (U.K.) and Vienna (Austria), the Tohoku University Sendai and the University of Osaka (both in Japan).

Laboratory Astrophysics/Cluster Physics

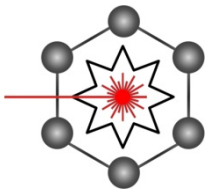

Prof. Dr. F. Huisken

- Photoluminescence studies of silicon and germanium nanocrystals produced by CO_2 laser pyrolysis
- Cavity ring-down spectroscopy of neutral and ionized polycyclic aromatic hydrocarbons (PAHs) in supersonic jets
- Study of astrochemical reactions in liquid helium nanodroplets

The Joint ***Laboratory Astrophysics/Cluster Physics*** Group at the Institute of Solid State Physics results from a cooperation between the Max-Planck-Institute for Astronomy, Heidelberg, and the Friedrich-Schiller-University, Jena. Inaugurated in February 2003, it is conducted by Prof. Dr. Thomas Henning and Prof. Dr. Friedrich Huisken.

The research of the Joint Laboratory Astrophysics and Cluster Physics Group is devoted to fundamental astrophysical questions that can be answered by laboratory experiments, with particular emphasis on spectroscopy. The electromagnetic radiation reaching us from stellar objects is modified in a characteristic manner by interstellar molecules and dust particles. Many of these “fingerprints” are still far from being understood. In order to determine the species causing the modification of the electromagnetic signals detected by telescopes and satellites, comprehensive laboratory studies are urgently needed.

The laboratory is equipped with modern molecular and cluster beam machines as well as laser systems to contribute to the clarification of such fundamental questions. For this purpose, the molecules, clusters, and nanoparticles of interest are prepared in vacuum chambers under conditions coming close to those encountered in the interstellar space (low temperature and low density).

Physics of Thin Films

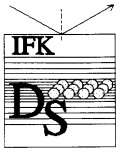

Dr. B. Schröter

- Analyses of surfaces, layers and nanostructures using AES, XPS, LEED, RHEED, XPD, STM, AFM, and SEM
- Deposition of thin films of semiconductors and of metallic nanoparticles using molecular beams at ultrahigh vacuum conditions
- Chemical vapor deposition and characterization of carbon nanotubes
- Growth of graphene and carbon nanotubes on silicon carbide

The group **„Physics of thin films“** at the institute of solid-state physics is engaged in the research on nanostructures, solid surfaces and thin films of semiconductor materials like silicon carbide and gallium aluminum arsenide as well as on carbon nanotubes and organic molecules on semiconductor surfaces.

For analyses of the chemical composition and bonding at surfaces and in thin films we use surface analysis methods like photoelectron spectroscopy (XPS, UPS) and Auger electron spectroscopy (AES). The crystalline structure can be determined by electron diffraction (LEED, XPD, and electron channeling). Scanning tunneling microscopy (STM), atomic force microscopy (AFM) and scanning electron microscopy (SEM) are used for high-resolution imaging of nanostructures and surfaces.

Molecular beam epitaxy (MBE) in ultra-high vacuum (UHV) is the preferred technique to grow nanostructures and semiconductor heterostructures (Si, Ge, SiC, GaAs, AlAs, and InGaAs) for electronic and optoelectronic applications. Our particular interest is to understand and to control the impact of the substrate surface preparation and of the growth conditions on the structure and the properties of thin films and nanostructures.

Carbon nanotubes have been produced on solid substrates by chemical vapour deposition (CVD) using methane and ethanol as precursor gas. Metallic nanoparticles acting as catalyst have been prepared by physical vapor deposition of Fe, Co or Ni in UHV utilizing our in-situ surface characterization methods.

Extensive characterization of the CVD samples by SEM, AFM and Raman spectroscopy revealed high-quality single-wall carbon nanotubes of diameters between 1 and 2 nm. The amount of residual catalyst and amorphous carbon species has been determined to be very low. Post-growth purification techniques like heating in vacuum, in air or in hydrogen atmosphere could further improve the nanotube material. Successful experiments to functionalize nanotubes by organic molecules have been the first step to investigations on future biochemical sensors.

Our long-time experience in silicon carbide research has been used to grow graphene as well as carbon nanotubes on single-crystalline SiC substrates.

The carbon nanotube research is strongly supported by the cooperation with the Astrophysics Institute, the Institute of Applied Physics and the Institute of Photonic Technologies.

Photovoltaics

PD Dr. H. Metzner

- Preparation and development of $Cu(In,Ga)(Se,S)_2$ - based thin film solar cells
- Preparation and development of CdTe-based thin film solar cells
- Investigation of epitaxially grown heterostructures for photovoltaics

The research of the ***photovoltaics*** group is directed to three different fields:

- Preparation and development of $Cu(In,Ga)(Se,S)_2$ - based thin film solar cells (CIGS). The research aims at a better understanding of the materials science of the CIGS chalcopyrite semiconductor and the improvement of existing and the development of novel cell concepts. To this end, a complete baseline on a form factor of 10x10 cm^2 is available as well as various characterization tools including AM 1.5 solar simulation and spectral response.

- Preparation and development of CdTe-based thin film solar cells. The research aims at a better understanding of the materials science of the II-VI semiconductor CdTe and the improvement of existing and the development of novel cell concepts. To this end, a complete baseline on a form factor of 10x10 cm^2 is available as well as various characterization tools including AM 1.5 solar simulation and spectral response.

- Investigation of epitaxially grown heterostructures for photovoltaics. The research aims at a better understanding of the materials science of heterostrucures between silicon and CIGS and the development of novel cell concepts. To this end, a complete system for molecular beam epitaxy (MBE) is in operation which includes the *in situ* analysis by means of electron diffraction (RHEED).

The photovoltaics group collaborates with other university groups, research institutions, and the photovoltaic industry in numerous research projects.

The IFK photovoltaics group is member of the following institutions which include:

- **“Solar Input” e.V.**

a collaboration of photovoltaic industry and research institutions located in Thuringia,

- **“PV-Uni-Netz”**

a collaboration of photovoltaic research groups at 12 German universities.

Ion Beam Induced Bending and Alignment of Semiconductor Nanowires

C. Borschel, R. Niepelt, S. Geburt, C. Gutsche[a], I. Regolin[a],

W. Prost[a], F.J. Tegude[a], D. Stichtenoth[b], D. Schwen[c], and C. Ronning

a) Institute for Semiconductor Technology, University of Duisburg-Essen, Lotharstr. 55, 47057-Duisburg

b) II. Institute of Physics, University of Göttingen, Friedrich-Hund-Platz 1, 37077 Göttingen

c) Department of Materials Science and Engineering, University of Illinois @ Urbana-Champaign, 1304 W.Green St., Urbana, IL 61801, USA

Introduction

Semiconductor nanowires (NW) have been grown extensively[1] and have been utilized as functional devices in recent years[2] based on controlled growth methods and neat assembling techniques.

When NWs grow epitaxially, their orientation depends on the substrate surface orientation as well as their preferred growth direction. Thus, their orientation cannot be chosen freely during growth, demanding possibilities for post-growth alignment in case special orientations are needed. Ion beam irradiation is known to drive morphology changes in nano-sized structures and may thus serve the purpose.

Experimental

Gallium arsenide (GaAs) nanowires were grown on top of <100> GaAs substrates using metal-organic chemical vapor deposition (MOCVD).[3] The resulting wires of about 10-20 µm length grow preferentially in the <111> direction. They adopt the epitaxial relation of the substrate, thus, they grow with an angle of about 35° of the substrate surface.

The GaAs NWs were irradiated with increasing fluences of Ar, Xe, and S ions, each with different energies. In the low energy cases, the ions are stopped within the top half of the NWs, whereas in the high energy case, ions are implanted close to the bottom of the NWs.

Results

Scanning electron microscopy images illustrate exemplarily the results of the irradiation for the low (fig. 1) and the high (fig. 2) energy case.

While the NWs keep straight for small fluences (~10^{13}/cm^2) like the non-irradiated samples, bending occurs at higher fluences. For the low energy case, a down-bending can be observed, which increases with ion fluence.

In the case of high energy implantation the NWs start to bend upwards, but at some point, the direction of the bending is reversed at the tip. For high fluences, the NWs tend to align towards the direction of the incident ion beam.

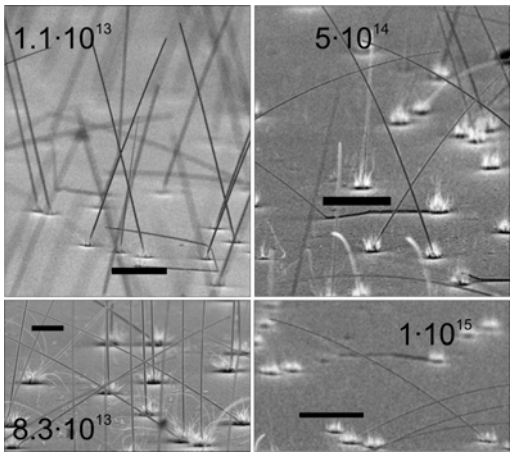

Fig. 1: NWs irradiated with different fluences of 35 keV Ar ions (in ions/cm^2). Scale bars are 5µm.

Discussion

In the collision cascades during ion irradiation, large numbers of defects are created (at the order of ~10^3 per ion). These lead to a volume expansion of the irradiated ma-

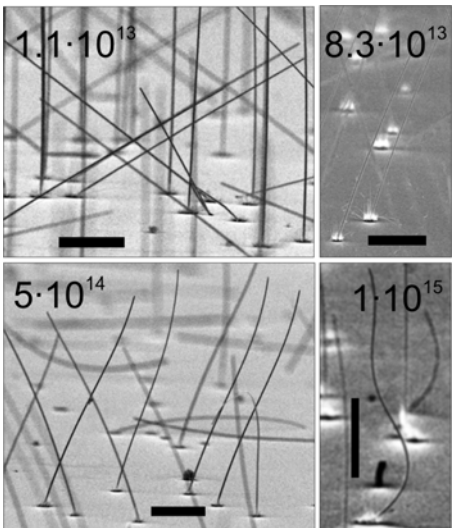

Fig. 2: NWs irradiated with different fluences of 210 keV Ar ions (in ions/cm^2). Scale bars are 5µm.

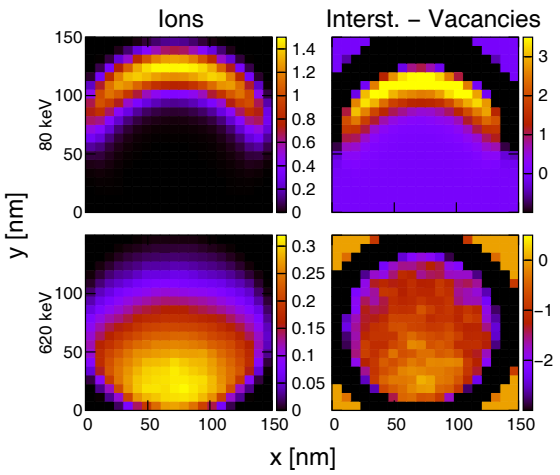

Fig. 3: Distribution of implanted ions and defects, for the low (top) and the high (bottom) energy case.

terial. Simulations of the irradiation were done with a new "3d-version" of TRIM[4,5], to obtain the distributions of ions and defects for the profile of the NW as illustrated in fig. 3. Because the majority of vacancies (vac) and interstitials (int) annihilate at RT implantation in GaAs[6], we plot the difference of int–vac in the right column. There is a forward bias of the ints with respect to the vacs due to the knock-on processes in the collision cascade. This results in an excess of ints at the bottom of the cascade and vacs at the top.

In the low energy case, only the top part of the NWs is affected, inducing volume expansion only there and thus a bending momentum down towards the surface.

In case of high energy irradiation, defects are created in the whole wire, but the volume expansion due to ints appears at the bottom. Thus, an upward bending momentum is induced. After some bending, the angle between wire and ion beam changes dramatically at the tip, shortening the projected range of the implanted ions. Further damage is now created closer to the top of the wire, which leads to opposite bending of the NW tip and, thus, straightening of the wires. At high fluences a self-alignment of the NW towards the incident ion beam direction is observed.

Conclusion and Outlook

Ion beam induced bending of nanowires was observed and it is illustrated, that ion beams can be utilized for post-growth alignment of nanowires. The formation of vacancies and interstitials has been identified as the driving mechanism for the bending.

Simple models for the alignment process of the nanowires are presented. In order to obtain a more precise understanding of the alignment, it is planned to perform ion irradiation and SEM characterization in-situ using a dual-beam FIB.

References

1. N. Wang, Y. Cai and R.Q. Zhang, Mater. Sci. Eng. R **60,** (2008), 1-51.
2. C.M. Lieber and Z.L. Wang, MRS Bulletin **32**, (2007) 99-108.
3. I. Regolin, V. Khorenko, W. Prost, F.J. Tegude, D. Sudfeld, J. Kästner, G. Dumpich, K. Hitzbleck and H. Wiggers, J. Appl. Phys. **101**, (2007) 054318.
4. J.F. Ziegler, J.P. Biersack and U. Littmark, *The stopping and ranges of ions in solids*, Pergamon Press, New York, 1985. (See also: www.srim.org)
5. D. Schwen, M. Huang, and R.S. Averback, J. of Nucl. Mater. (2008), submitted.
6. E. Wendler, Nucl. Instr. Method. B **147**, (1999), 155.

Synthesis of ZnO-Nanowires by VLS-Mode

M. Kozlik, C. Borschel, S. Geburt, R. Niepelt, M. Gnauck, C. Ronning

The synthesis of nanowires (NW) is done by a simple vapour transport process in a horizontal tube furnace. A complete computer controlled 3-zone tube furnace with a maximum temperature of 1350 °C and tuneable temperature gradient as well as an high-temperature furnace with a maximum temperature of 1500°C have been installed at the NW-Lab in the institute (see figure 1).

Fig. 1: This picture shows the installed 3-Zone-Furnace and the High-Temperature-Furnace.

In the centre of the tube at the hottest point, the source material is placed and vaporized by heating of the furnace. The two ends of the tube are connected on one side with a gas inlet and on the other side with a pressure control system. So a vectored gas flow can be realized within the tube and the direction can be changed by a cross valve. The gas support is regulated by two mass flow controllers (100sccm/10sccm). Argon, nitrogen, oxygen, hydrogen or simple air are the available gases. So the vapour can be transported to a colder point of the tube where it condensates at the walls or placed substrates.

The basis of the NW synthesis is the vapour-liquid-solid-mechanism, which was described by Wagner and Ellis in 1964 [1] and is illustrated in figure 2. It deals with metal islands on a substrate (wafer) which acts as nuclei for the whisker. By heating and supply with a semiconductor vapour a liquid alloy is formed, because the melting point is degraded compared to the originally metal. The crystallisation of the nanowire starts by oversaturation of the liquid with the semiconductor material. So the metal (e.g. gold) conduces as a catalyst and forms a drop on the top of the wire. The size of these drops affects the diameter and the growth time determines the length of the NWs. There are three different principles for the absorption of the semiconductor to the wire: the semiconductor steam reacts at the surface of the drop, semiconductor atoms on the drop surface diffuse to the semiconductor-metal-interface or the semiconductor atoms hit the wafer and diffuse to the semiconductor-metal-interface. A second (lateral) growth can be achieved by increasing the temperature and the pressure which leads to a deposition of the semiconductor at the wall. The growth rate can be ramped up with higher substrate temperature or more gas supply, because the amount of the source material is increased.

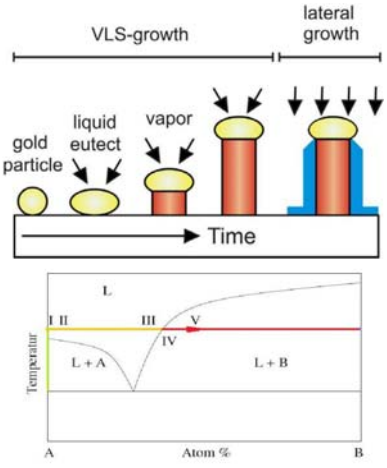

Fig. 2: This graphic shows the Principe of the VLS-Mode: (I) Metal cluster, (II) adsorption, (III) liquid alloy, (IV) nucleation, (V) growth

We used p-type Si (100) substrates with a natural oxide film which are coated with a gold layer. The substrate was cooked in acetone, rinsed with ethanol and finally blown dry with nitrogen. Either a vapour deposition processor or a sputter coater (Jeol JFC-1200 Fine Coater) was used to deposite the gold catalyst, which forms droplets at high temperature.

The source material was ZnO powder (Alfa Aesar: 99.99%) which can be mixed with carbon (Alfa Aesar: 99.99%) for carbon-assisted growth (CAG) [2]. The aim of CAG is to reduce the sublimation point by the reduction of ZnO (sublimes at 1800°C) to Zn (Boiling point at 907°C):

$$ZnO + C \rightarrow Zn + CO$$
$$ZnO + CO \rightarrow Zn + CO_2$$
$$CO_2 + C \rightarrow CO$$

The samples were characterized with a scanning electron microscope (SEM) and representative images are shown in figure 3.

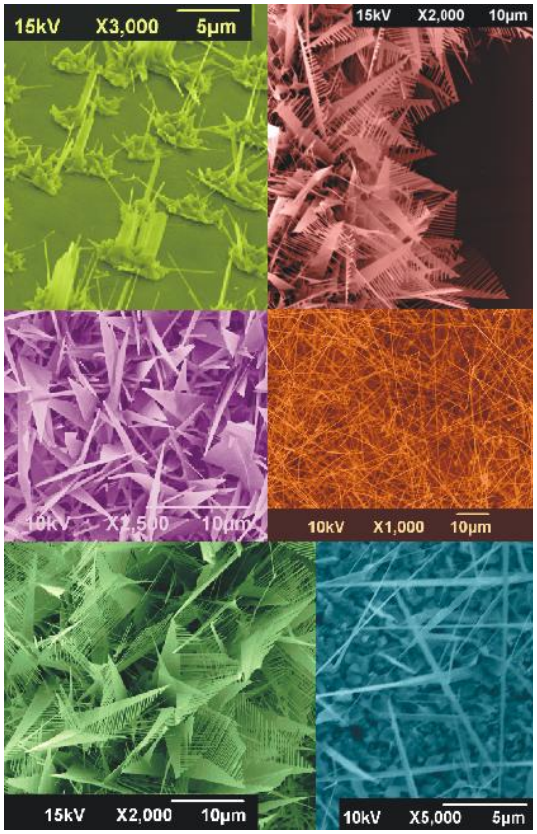

Fig. 3: These are SEM-figures of several samples grown under different conditions.

Both growth mechanisms are clearly visible: VLS and lateral growth on the sides. By changing the growth parameters one can obtain different reproducible nanostructures. Therefore one can see long nanowires, nanosails and other shapes [3, 4]. The direction is determined by the crystal structure. Because one direction grows faster compared to another one, it is possible to get a variety of forms. There is often a metal drop on the top of the wire, which is a relic of the catalyst.

Interesting aspects for research in the future are the catalytic effect of other material instead of gold, because of plasmonic effects. It would be also exciting to look on the properties of the growth of other source materials and their growth parameters.

References:

[1] R.S. Wagner et al., Appl. Phys. Lett. **4** (1964) 89.
[2] J. Wang et al., Mater. Lett. **59** (2005) 2710.
[3] C. Ronning et al., Georgia Augusta **4** (2005) 82.
[4] C. Ronning et al., Phys. unserer Zeit **37** (2006) 34.

Rare earth doped ZnO nanowires

S. Geburt, S. Müller[1], D. Stichtenoth[1], J. Wang[2], Q. Li[2] and C. Ronning

[1]*II. Physikalisches Institut, Georg-August-Universität Göttingen*

[2]*Chinese University of Hong Kong, Hong Kong*

Introduction

ZnO nanowires (NWs) offer unique properties for optoelectronics, e.g. as UV-emitting light source[1] or as waveguides[2]. Lasing action could be observed[3] under high power optical excitation. Nevertheless, 300 kW/cm² is necessary to reach the transition from amplified spontaneous emission to stimulated emission.

To lower the threshold, the quasi-2-niveau-laser system of the ZnO has to be modified to a 4-niveau-system, which could be done by introducing optical active elements. Rare earth elements (RE) are well known to be useful dopants for laser mediums, e.g. in Nd:YAG lasers. Therefore, RE doped ZnO nanowires could lead the way to a nano-scaled lasing device.

Experimental

ZnO NWs were synthesized using the VLS mechanism with diameters around 40 nm and length up to 5 µm. The doping with rare earth elements (RE) during growth of the NWs failed[4] due to the high melting point of the RE and RE compounds and low solubility of RE in ZnO. Therefore, ion implantation offers an alternative and very good controllable method for doping[5]. A box-like profile matching about the diameter of the nanowires was simulated by SRIM using 4 different energies (5 - 55 keV). After transfer to clean Si substrates, the NWs were implanted with Eu, Tm, Yb and Xe with fluences ranging from $1.7 \cdot 10^{13}$ cm^{-2} to $5.2 \cdot 10^{15}$ cm^{-2} (0.01 to 3.3 at.-%). After implantation, the nanowires were annealed at 700 °C for 30 min in oxygen atmosphere.

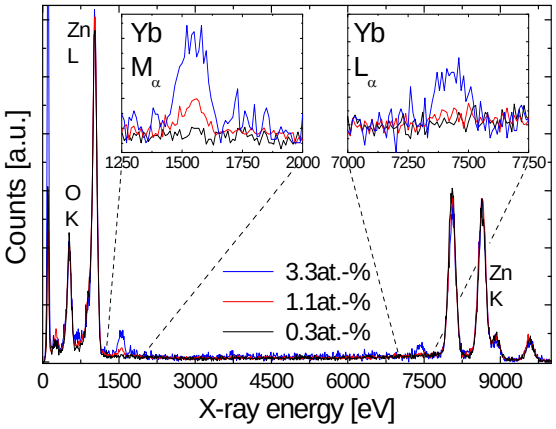

Fig. 1: EDX spectra of Yb implanted ZnO nanowires (0.3 to 3.3 at.-%).

Results and discussion

The stoichiometry of the implanted nanowires was examined by EDX and EELS in the TEM. RE related X-ray energies could be detected from the doped ZnO NWs with concentrations above 1 at.-%. (see Fig. 1). The samples with low concentrations showed no EDX or EELS signal due to the detection limit. The intensity of the signals increase with higher concentrations revealing a successful doping with the desired concentrations. No out-diffusion of the RE atoms occurred during annealing.

Electron microscope techniques (SEM, TEM) were used to study the morphology changes do to the ion implantation. The NWs showed an increase of surface roughness ascending with the fluence. This arises from massive sputtering after ion impact; the sputter yields were calculated to 6-12 atoms/ion by SRIM, which results in a removal of up to 100 monolayers at the highest fluence. Nevertheless, the atomic lattice was recovered by annealing and no amorphisation as well as no other phases or RE

clusters could be found in high resolution TEM pictures.

The subsequent photoluminescence (PL) studies at low temperatures reveal the recovery of the near band edge emission of the ZnO NWs at 3.37 eV (see Fig. 2). Two broad bands show up between 1.5 and 2.75 eV, which can be attributed to remaining defects. A sharp peak at 1.26 eV could be assigned to the intra-4f-luminescence of Yb implanted ZnO NWs. To rule out the possibility that the Yb emission emanate from RE atoms in the top SiO_2 layer covering the substrate, a clean Si substrate was identically implanted and annealed as described before, but showed no luminescence.

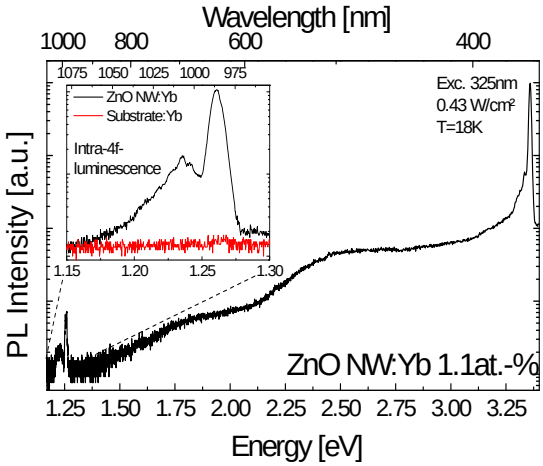

Fig. 2: PL spectra of Yb implanted ZnO NWs. Inset: comparison between implanted NWs and Si reference sample.

The RE luminescence intensity was examined as a function of doping concentration. In the case of Eu and Yb, the intensity increases with the concentration. A derivation from the linear relation could be understood as an efficiency decline resulting from energy transfer between the RE atoms. The mechanism becomes more efficient with shortened distance between the RE atoms, therefore energy transfer to non radiative sites ("killer centers") has to be take into account as well.

The luminescence intensity decreases with increasing temperature, but could be still observed at room temperature.

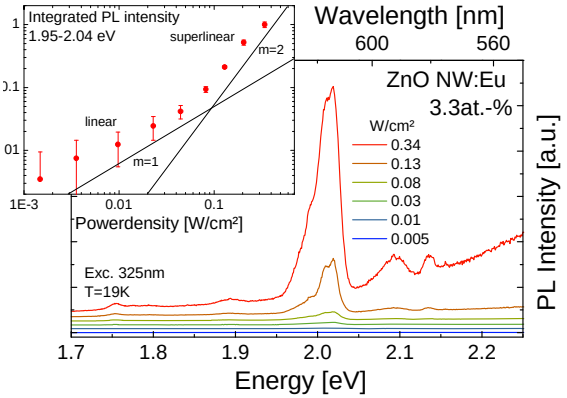

Fig. 3: Power dependent PL spectra of Eu doped ZnO NWs. Inset: PL intensity as a function of power density of the excitation source.

The PL intensity rises linear with increasing excitation power (see Fig. 3). Above a threshold of about 0.1 W/cm², a superlinear progression could be detected, which is equivalent to a gain in luminescence intensity. This can be explained by the achievement of population inversion of the RE atoms. Spontaneous emitting RE atoms stimulate other ones to deexcite by releasing a photon. This process is known as spontaneous amplified emission or random stimulated emission. Unfortunately, gain due to laser oscillations is not possible considering the undersized diameter of the NWs[2,3].

Acknowledgements

Financial support from DAAD grant G_HK013/05 and DFG SPP1165 Ro1189/7-1,2

References

[1] Yang et al., AFM, Vol. 12, 323-331, 2002
[2] Voss et al., NL, Vol. 7, 3675-3680, 2008
[3] Zimmler at al., APL, Vol. 93, 051101, 2008
[4] Geburt at al., JNN, Vol. 8, 1-8, 2008
[5] Ronning et al., APL, Vol. 84, 783-785, 2004

In-situ observation of surface oxide layers on medical grade Ni-Ti alloy during straining

A. Undisz*, F. Schrempel, W. Wesch, M. Rettenmayr*

** Institut für Materialwissenschaft und Werkstofftechnologie, Friedrich-Schiller-Universität Jena*

Due to its unique properties known as shape memory or pseudo elastic behavior Ni-Ti alloys have been established as material for medical implants designed for endoscopic or transcathetral surgical treatment techniques. Thereby the surface oxide layer plays an important role concerning the biocompatibility of the material. If the surface oxide layer is scratched, tissue and body fluid will get in permanent contact with the material beneath the oxide layer and allergenic or inflammatory reactions are probable. Therefore the surface oxide layer of Ni-Ti alloys is studied during pseudo elastic deformation of the base material.

The investigations were carried out using commercial Ni-Ti wires and sheets typically applied for medical implants. The surface oxide layer on the material was generated by annealing under air atmosphere at 540°C. To attain different oxide layer thicknesses the annealing times were set between 2 and 60 minutes.

The surface oxide layers of the Ni-Ti sheets were investigated by means of Rutherford backscattering spectrometry (RBS). Exemplarily, Fig. 1a shows the concentration profiles after annealing for 5 and 60 min, respectively. The untreated sample shows a very thin natural oxide layer (not shown). After annealing the oxygen concentration is significantly increased. Irrespective of the annealing time the surface concentrations of Ti and O are approx. 33 at.% and 65 at.%, respectively, indicating that mainly stoichiometric TiO_2 has formed. The concentration of the residual Ni on the surface of the sheets is approx. 2 at.% independent of the annealing times. Beneath the surface the Ni concentration drops to an undetectable amount. Furthermore the Ni concentration exhibits a concentration maximum of up to 65 at.% beneath the oxide layer that is significantly higher than in the base alloy.

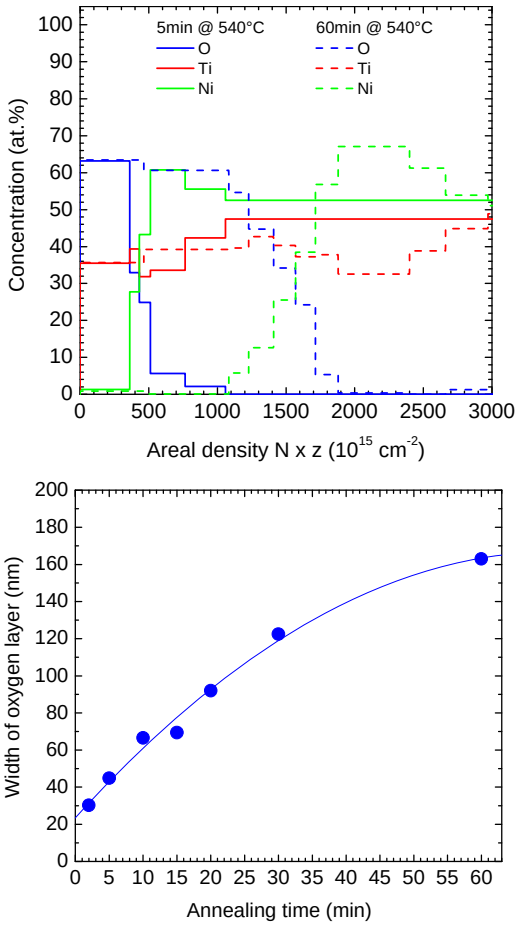

Fig. 1: Concentration profiles for the Ni-Ti surface after annealing for 5 and 60 min (top) and surface oxide layer thickness (FWHM) as a function of the annealing time (bottom). The thickness is calculated from the concentration profiles using the atomic density of rutile.

The oxide layer thickness increases from 30 nm after 2 min annealing up to 160 nm after 60 min annealing (see Fig. 1b). Its growth follows a parabolic growth law revealing that it is controlled by diffusion.

In tensile straining experiments the heat treated wires were deformed stepwise up to approx. 8% absolute strain while observing the surface in the Scanning Electron Microscope (SEM). After the maximum strain of approx. 8% was applied, the wires were unloaded and investigated similarly as during the loading process.

A complex Lueders-like deformation behavior with localized high deformation of the material has been identified as an important factor for the formation of cracks in the surface oxide layer. Two different types of cracks under tensile strain were detected (see Fig. 2): (i) cracks perpendicular to the loading direction are caused by the longitudinal elongation; (ii) cracks along the loading direction are caused by the transversal contraction of the material.

For thin surface oxide layers (< 80nm) solely the first type of cracks was found. This type of cracks can close during unloading. However, for surface oxide layer thicknesses above 80 nm the two crack types occur simultaneously, resulting in flaking of oxide particles. Beneath the flaked oxide particles the metallic material with increased Ni concentration of up to 65 at.% can get in persistent contact to tissue and body fluids.

The study shows that the transversal contraction is more critical for the integrity of the surface oxide layer than the longitudinal elongation of the wires during straining. For the application of Ni-Ti alloys for medical implants the mechanical stability of the surface oxide layer needs to be optimized to avoid the damage. Under the conditions in the present work, the protective function of the surface oxide layer is assumed to be best for thicknesses between 60 nm and 70 nm. In this range the surface oxide layer has a large thickness to protect the material without the occurrence of flaking of oxide particles during the applied deformation.

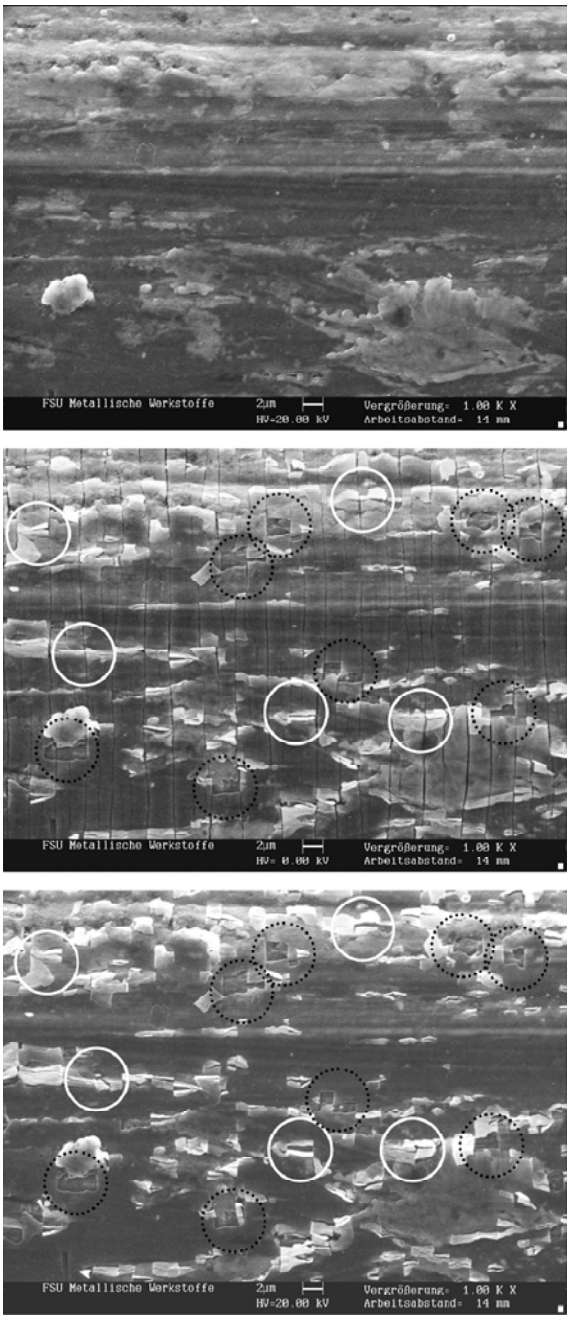

Fig. 2: SEM pictures of the Ni-Ti wire annealed for 20 min before loading (top), for the strained wire with cracks in the oxide layer perpendicular and longitudinal (white circles) to the loading direction accompanied by flaking of oxide particles (black circles) (middle) and after unloading, where the flaking of oxide particles is visible (black circles) (bottom). The loading direction is parallel to the scale bar. The cracks perpendicular to the loading direction disappear, whereas cracks longitudinal to the loading direction widen (white circles).

For details and refs. see A. Undisz et.al., J. Biomed. Mater. Res. A (2009), http://dx.doi.org/10.1002/jbm.a.31946.

Fabrication of ridge waveguides in zinc-substituted lithium niobate by means of ion-beam enhanced etching

H. Hartung*, E.-B. Kley*, A. Tünnermann*, Th. Gischkat, F. Schrempel, W. Wesch

** Institut für Angewandte Physik, Friedrich-Schiller-Universität Jena*

Low loss lithium niobate waveguides commonly fabricated by titanium diffusion, proton exchange or ion implantation are widely used in integrated optics. However, because of the very small index change the confinement of the light is weak and the mode size is large. Another approach for the confinement of the waveguide mode is the use of a ridge structure. Due to the large index contrast to the surrounding air, ridge waveguides offer higher confinement and smaller mode sizes, which results in more efficient devices. Additionally small curvature radii are possible enabling large scale integrated systems.

An essential requirement on the fabrication of ridge waveguides is a surface roughness as small as possible, because its attenuation strongly increases with increasing roughness of the top and side surfaces of the ridge. Furthermore the preferred shape of the waveguide is a rectangular one which is optimal for the realization of modulation devices.

High quality ridge waveguides have been fabricated by the combination of Liquid Phase Epitaxy (LPE) and Ion Beam Enhanced Etching (IBEE). The fabrication process is schematically illustrated in Fig. 1. A thin film of zinc doped lithium niobate with a thickness of 3.6 µm was grown on x-cut lithium niobate by means of LPE using a melt of 20 mol.% $LiNbO_3$, 80 mol.% $LiVO_3$ and ZnO at a deposition temperature around 830°C. The zinc substituted film has the advantage of a reduced photo refractivity compared to bulk lithium niobate. Additionally a slab waveguide is created due to the increased refractive index of the layer in comparison to the bulk material. For a LPE-layer having a zinc concentration of 6.2 mol.% the refractive indices at a wavelength of 514.5 nm increase by 0.0055 and 0.0037 for the ordinary and the extraordinary index, respectively.

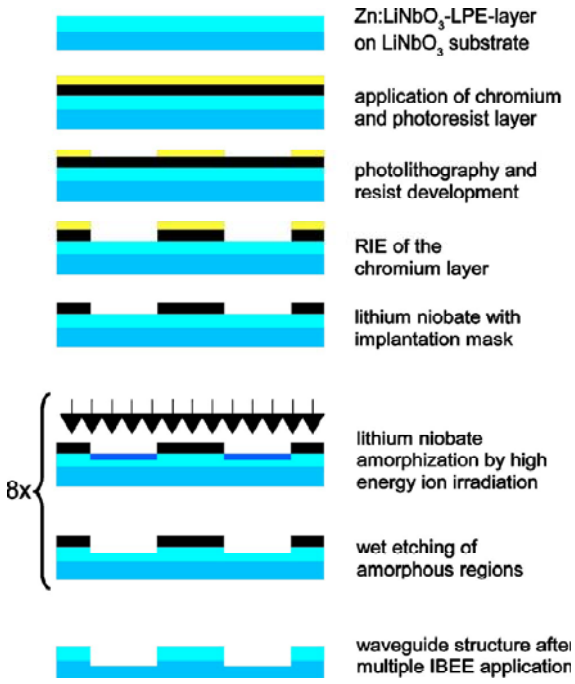

Fig. 1: Fabrication process of the waveguides in a zinc-substituted lithium niobate layer.

Subsequently ridge waveguides with widths between 4 and 8 µm were fabricated by IBEE. In this process selective ion irradiation of the crystalline lithium niobate causes the formation of defects, and as a consequence, the chemical resistance is reduced. Thus the irradiated regions can be removed by wet chemical etching without affecting the non-irradiated areas. First a chromium mask with a thickness of 450 nm was fabricated by a standard photolithographic process. The lithium niobate was multiple irradiated with 60, 150, 350 and 600 keV argon ions to such an extend, that an

amorphous layer within the non-covered regions starting at the surface down to a depth of approximately 450 nm was produced. Subsequently, the amorphous lithium niobate was etched for 10 min in a 3.7% solution of hydrofluoric acid at a temperature of 40°C. Because the chromium mask is not affected by the etching process the IBEE technique was applied for eight times, which results in a ridge depth of 3.7 µm.

Figure 2 shows a SEM picture of the end facets of the fabricated waveguides. The side wall angle is close to 90°, which supports the high selectivity of the process. The side wall roughness is estimated to be about 4 nm rms promising low attenuation values.

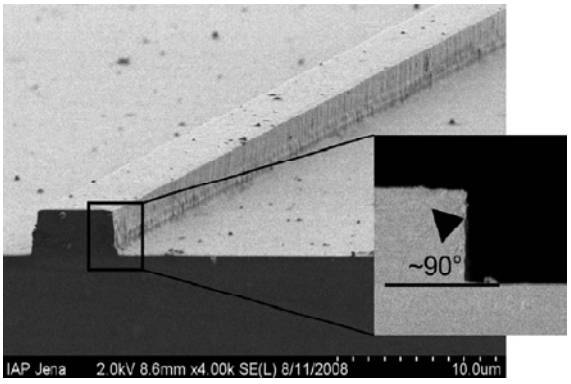

Fig. 2: SEM picture of the end facet of the waveguides.

The waveguide losses were determined by the measurement of the entrance and the output power of polarized laser light with a wavelength of 1064 nm. From the ratio the attenuation values were calculated taking into account the fresnel losses as well as the overlapping integral of the fiber and the waveguide output mode fields.

The slab waveguide fabricated by means of LPE, having a thickness of 3.6 µm, shows single mode guiding. The ridge waveguides etched into this layer does not guide for a width smaller than 5 µm. Waveguides with a width between 5.3 and 8.0 µm show single mode behavior. The attenuation decreases with increasing waveguide width. A minimum attenuation of 0.9 dB/cm for both, TM and TE polarization, is obtained for a ridge with a width of 6.7 µm. Figure 3 shows the geometry, the recorded output field of this waveguide and the simulated mode profile.

At further increase of the ridge width the attenuation increases because of the coupling into higher modes.

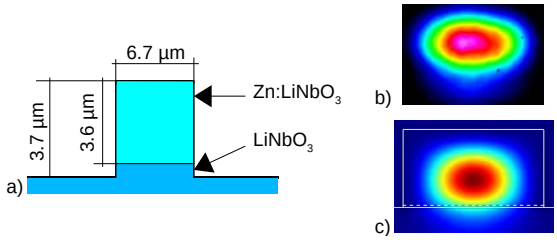

Fig. 3: Geometry (a), (b) measured (b), and simulated (c) mode profile of the fabricated waveguide at a wavelength of 1064 nm TE-polarization.

In conclusion a technology for fabrication of low loss ridge waveguides on lithium niobate has been demonstrated. The application of ion beam enhanced etching satisfies the essential specifications of the ridges, low roughness and a side wall angle close to 90°. This opens a promising way to realize fast, low loss integrated photonic devices like e.g. phase shifting devices or intensity modulators in lithium niobate for high power and SHG application.

For details and references see H. Hartung et.al., Opt. Lett. 33 (2009) 2320.

The authors would like to thank B.Martin, E.Würfel, A.Lorenz and C.Dubs for their contributions, regarding thin film growth and waveguide measurement. This work was funded by the Deutsche Forschungsgemeinschaft under priority program 1157, priority program 1199/2-1 and the Gottfried-Wilhelm-Leibniz-Programm.

Patterning of $LiNbO_3$ by means of ion irradiation using electronic energy deposition and wet etching

Th. Gischkat, H. Hartung*, F. Schrempel, E.-B. Kley*, A. Tünnermann*, W. Wesch

** Institut für Angewandte Physik, Friedrich-Schiller-Universität Jena*

The selective damage by ion irradiation and subsequent wet etching is an excellent method to pattern lithium niobate ($LiNbO_3$) crystals. Commonly, the defects are formed due to nuclear energy deposition of keV-ions. However, the crystal is also damaged by an energy transfer due to inelastic collisions between the ions and the electrons of the target atoms if a specific value of that electronic energy loss is exceeded.

Figure 1a shows the defect concentration for the irradiation of x-cut $LiNbO_3$ with 5 MeV Si-ions at various ion fluences.

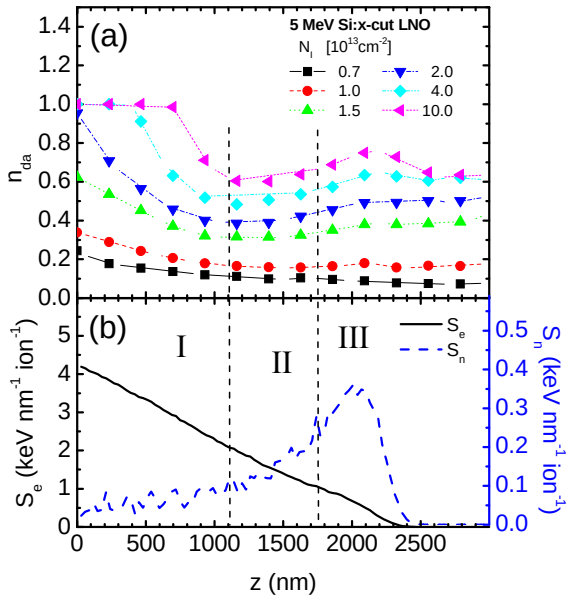

Fig. 1: Defect concentration n_{da} versus depth of x-cut $LiNbO_3$ after irradiation with 5 MeV Si-ions at room temperature with different ion fluence (a). Electronic and nuclear energy loss S_e and S_n, versus depth calculated by SRIM2003 (b).

Three regions of damage can be distinguished: a damaged surface layer (I), a buried damaged layer (III) located at a depth of about 2200 nm as well as a transition layer (II) in between. Comparing the defect distribution with the calculated energy loss distribution of the ions (Fig. 1b) it is obvious that the buried damaged layer is a consequence of the nuclear energy loss of the ions.

The damage close to the surface can be attributed to the electronic energy deposition by the Si-ions. The amount of damage produced depends on the depth, i.e. on the electronic energy deposition, as well as on the ion fluence. In Fig. 2a the defect concentration taken at the surface is depicted

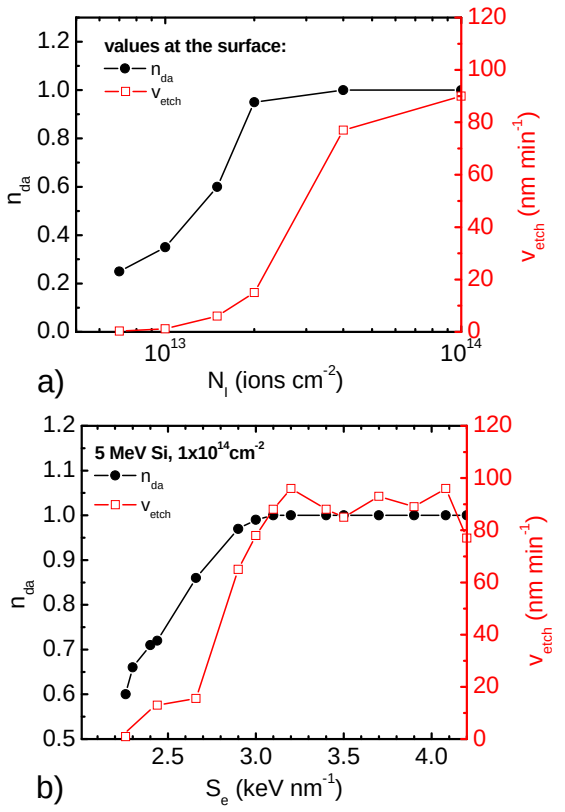

Fig. 2: Defect concentration n_{da} and etching rate v_{etch} taken at the surface versus the ion fluence (a) as well as the defect concentration n_{da} and etching rate v_{etch} versus the electronic energy loss S_e for the irradiation with 1×10^{14} cm^{-2} Si-ions (b).

versus the ion fluence.

The defect concentration increases with increasing ion fluence up to the amorphiza-

tion. With further increasing ion fluence the amorphous layer broadens to larger depths. For 1×10^{14} cm^{-2} a 700 nm thick amorphous layer is produced. This ion fluence is 10 times lower compared to the fluence which is necessary to produce an amorphous layer with similar thickness due to nuclear energy deposition.

The thickness of the amorphous layer is determined by the depth where the electronic energy deposition is below a certain value (Fig. 1a). This value is higher for lower ion fluences. Fig. 2b shows the defect concentration taken at different depths versus the corresponding electronic energy deposition for the irradiation with 1×10^{14} cm^{-2} Si-ions. In this case the crystal is amorphous down to a depth where the electronic energy deposition is below 3 keV nm^{-1}. With decreasing energy loss, i.e. with increasing depth the defect concentration decreases down to 0.6 for an electronic energy loss of about 2.3 keV nm^{-1}.

The etching behavior of $LiNbO_3$ damaged due to the electronic energy loss is similar to the etching behavior of that material damaged by nuclear energy loss. In Fig. 2a and b the corresponding etching rates are depicted versus the ion fluence and the electronic energy deposition, respectively. In both cases the etching rates are correlated with the defect concentration. The etching rate amounts to about 100 nm min^{-1} for amorphized material. With decreasing defect concentration the etching rate decreases drastically. For a defect concentration below 0.6 the etching is negligible.

According to the damage distribution the etching rate decreases with increasing depth. In all cases the etching stops at the end of region I at the latest. It seems that in region II the damage is not sufficient for remarkably etching. As a consequence region III was not reached for etching in a 3.7% HF-solution at an etching temperature of 40 °C for several hours. The expected etching rates in region III are below 5 nm min^{-1} according to the low damage well below the amorphization.

As example x-cut $LiNbO_3$ was patterned with a photonic crystal structure using a 2 µm thick silicon mask and irradiation with 5 MeV Si-ions at an ion fluence of 1 x 10^{14} cm^{-2} (see fig. 3).

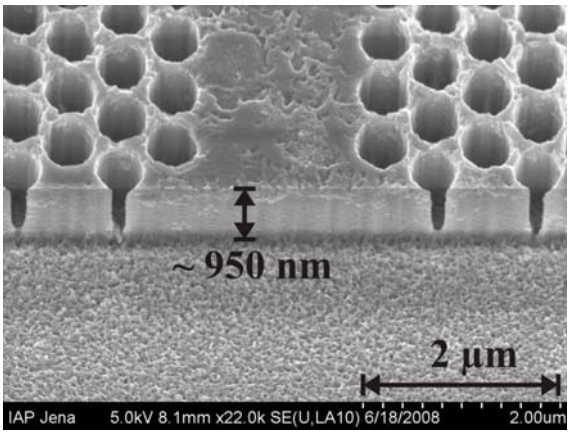

Fig. 3: SEM picture of a hexagonal arrangement of holes in x-cut $LiNbO_3$ fabricated by the IBEE technique using the electronic energy loss.

The holes which are hexagonally arranged have a depth of 950 nm after etching in 3.7% HF at 40°C for 30 min. The sidewalls of the holes are nearly vertical indicating high contrast. The diameters of the etched holes are about 450 nm which is quite similar to the width of the mask holes.

As a consequence the defect formation by electronic energy loss of high energetic ions enables the fabrication of deep structures with high aspect ratios very easily.

For details and refs. see Th. Gischkat et.al., Microelectron. Eng. (2009): http://dx.doi.org/10.1016/j.mee.2008.11.031.

The authors want to thank the Deutsche Forschungsgemeinschaft (DFG) for financial support (Contract No. KL1199/2-1).

Annealing behavior of lithium niobate irradiated with He-ions at 100 K

Th. Gischkat, F. Schrempel, Th. Höche*, W. Wesch

** Leibniz-Institut für Oberflächenmodifzierung e.V., Permoserstrasse 15, D-04318 Leipzig*

In order to investigate the formation and the annealing of defects, x- and z-cut lithium niobate ($LiNbO_3$) crystals were irradiated with 200 keV He-ions at a temperature of 100 K. Investigations were done using Rutherford-Backscattering Spectroscopy (RBS) and High Resolution Transmission Electron Microscopy (HRTEM) immediately after the irradiation, after warming to room temperature as well as after thermal treatment at 250°C.

Fig. 1 shows the defect concentration as a function of depth for x- and z-cut $LiNbO_3$, respectively. The ion fluence was 1×10^{16} cm^{-2}. A damaged layer is produced and the maximum of the defect distribution is located at a depth of about 600 nm.

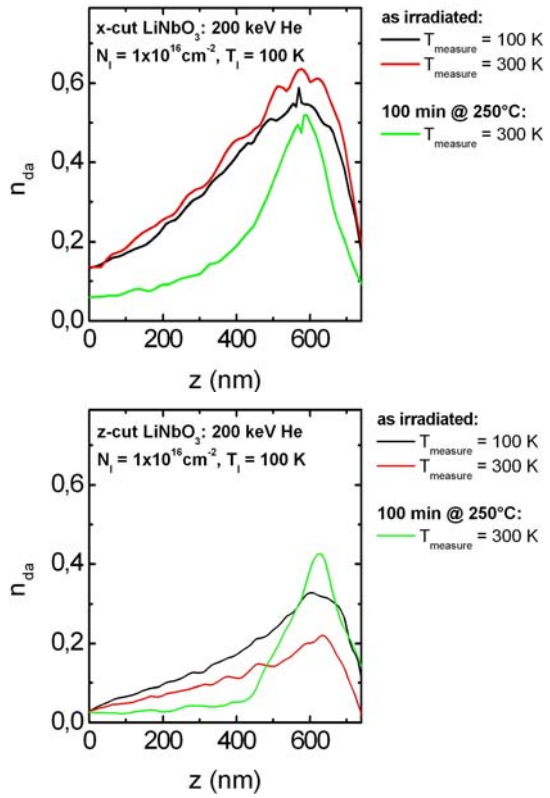

Fig. 1: Depth distribution of the defect concentration n_{da} for x-cut (top) and z-cut (bottom) $LiNbO_3$ irradiated with 200 keV He-ions.

Considering the as-irradiated samples measured at 100 K the crystal is apparently more damaged for x-cut compared to z-cut $LiNbO_3$. In contrast TEM-investigations (not shown) show no differences between the different cuts. This confirms the assumption that the different defect concentration measured by RBS channeling is a consequence of the preferential arrangement of displaced Nb-atoms on vacant octahedral sites [1]. Due to their position in the lattice these sites cause different dechanneling of the analyzing He-ions along different crystal axis. At 100 K about 20% of the Nb-atoms occupy such vacant octahedral lattice sites.

After warming to room temperature the difference between x- and z-cut is increased. This indicates that, as a consequence of thermally enhanced mobility of the atoms, randomly distributed Nb-atoms move to vacant octahedral sites. Thereby the percentage of displaced Nb-atoms localized on the vacant octahedral sites amounts to 40%.

After thermal treatment for 100 min at 250°C the defect concentration near to the surface decreases for x- and z-cut indicating the annealing of defects. A completely different behavior is observed within the damaged layer. Whereas for x-cut the defect concentration decreases it increases for z-cut $LiNbO_3$. Fig. 2 shows the defect concentration taken in the maximum of the depth distribution versus the annealing time for thermal treatment at 250°C. For x-cut $LiNbO_3$ the defect concentration decreases continuously with increasing annealing time indicating the annealing of defects. On the contrary, for z-cut irradiated with high fluences (1×10^{16} cm^{-2}) the defect concen-

tration increases drastically after thermal treatment for 120 min. For longer annealing times the defect concentration also decreases. Finally a saturation of the defect concentration can be observed.

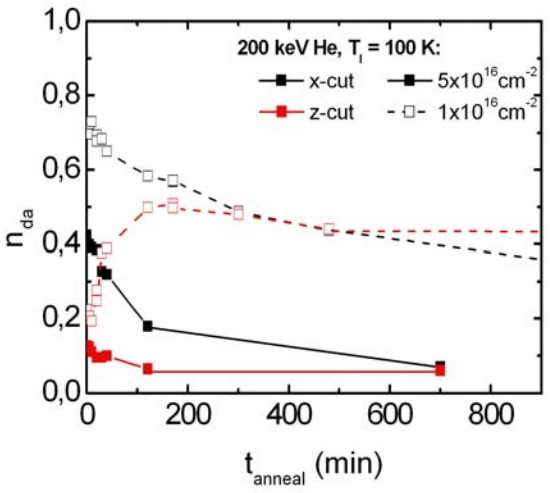

Fig. 2: Defect concentration of 200 keV irradiated $LiNbO_3$ versus annealing time for thermal treatment at 250°C.

The corresponding TEM-image in fig. 3 shows that in the damaged layer dislocation loops are formed, which is probably a consequence of the redistribution and agglomeration of point defects. The dislocation loops are localized at a mean depth of about 635 nm with equal spacing of about 120 nm. Apparently, the dislocation loops are nearly aligned perpendicular to the z-cut surface but parallel to the x-cut surface (sketches in fig. 3) indicated by the stress field around the dislocations. The TEM-image of x-cut material shows cracks within the sample which can be explained by the superimposed stress field of the dislocation loops aligned parallel to the surface. Eventually, the apparent decrease and increase of the defect concentration for x- and z-cut, respectively, after thermal treatment can be explained by different dechanneling of the analyzing ions due to different lattice strain for different crystal axes.

A different annealing behavior is observed for the samples irradiated with low fluences

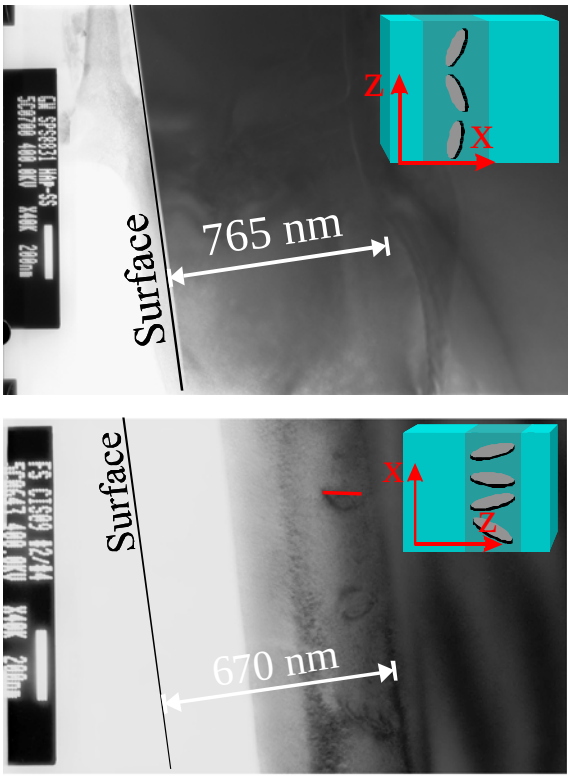

Fig. 3: Cross-section TEM-images of x-cut (top) and z-cut (bottom) $LiNbO_3$ irradiated with 1 x 10^{16} cm^{-2} He-ions at 100 K and subsequently thermal treated at 250°C for 100 min. The sketches show schematically the position and orientation of the dislocation loops in the damaged region.

(5 x 10^{15} cm^{-2}). The maximum of the defect distribution decreases simultaneously with increasing annealing time for x- and z-cut $LiNbO_3$ indicating the annealing of defects. Obviously at low defect concentration the point defects anneal but do not agglomerate into dislocations.

For details see Th. Gischkat et.al., Nucl. Instr. and Meth. B (2009), in print.

[1] G. Götz, H. Karge, Nucl. Instr. and Meth. 209/210 (1983) 1079.

The authors want to thank the Deutsche Forschungsgemeinschaft (DFG) for financial supporting (contract number KL1199/2-1). Access to the high-resolution TEM facilities at MPI for Microstructure Physics Halle granted by U.M. Gösele is gratefully acknowledged.

Influence of ion energy and ion species on ion channeling in $LiNbO_3$

T. Steinbach, F. Schrempel, Th. Gischkat, and W. Wesch

Ion irradiation of $LiNbO_3$ causes the formation of defects due to nuclear as well as electronic energy deposition ε_n and ε_e, respectively. This effect is utilized for Ion Beam Enhanced Etching (IBEE), a powerful patterning technique for fabricating new photonic devices in $LiNbO_3$ [1]. However, the defect formation is influenced by the orientation of the crystal. If the irradiation is performed along a low index crystallographic direction (on-axis) the defect distributions are strongly affected by ion channeling [2].

In order to investigate the effect of ε_n and ε_e on damage formation, $LiNbO_3$ crystals were irradiated on- and off-axis using Si and Cu ions with energies ranging from 550 keV to 2 MeV. To achieve comparable defect concentrations in the maximum of the defect distributions, the ion fluences were chosen to $3x10^{14}$ and $7x10^{13}$ cm^{-2} for Si and Cu ions, respectively.

As an example, Figure 1 shows the relative defect concentration for on- and off-axis irradiated $LiNbO_3$ with Si ions using ion energies of 1 MeV and 2 MeV.

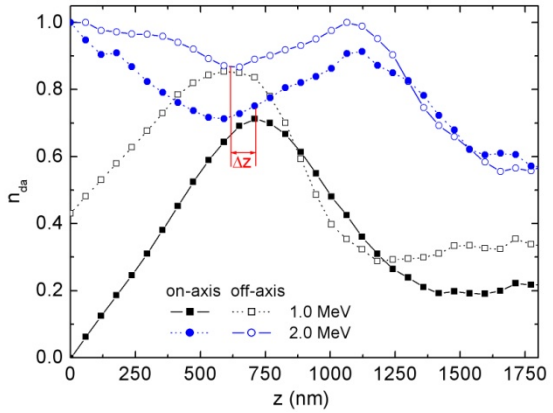

Fig. 1: Relative defect concentration versus depth for x-cut $LiNbO_3$ irradiated with Si ions with ion energies of 1 and 2 MeV. The fluence amounts to $3x10^{14}$ cm^{-2}.

For on-axis irradiation at low ion energies (squares in Fig. 1), where ε_n dominates the formation of defects, the defect distribution is shifted to larger depths (see Δz in Fig. 1) compared to off-axis irradiation. On the other hand for irradiation with high ion energies (circles in Fig. 1) apart from the damage peak caused by nuclear energy deposition an increased defect concentration at the surface of the crystal is obtained. Additionally to the formation of an amorphous layer at the surface, a decrease of the peak shift Δz, i.e. the difference of the depth of the defect maxima for on- and off-axis irradiation, is observed.In Table I the measured peak shifts Δz are summarized for all ion species and ion energies used for the irradiation.

Tab. 1: Shift of the maximum of the defect distribution Δz as well as the electronic energy deposition ε_e at the surface for the irradiation of x-cut $LiNbO_3$ with Si and Cu ions of various energies at an ion fluence of $3x10^{14}$ and $1x10^{14}$ cm^{-2}, respectively.

Ion	E_{ion} (keV)	ϵ_e (eV Å^{-1})	Δz (nm)
	No surface damage		
Cu^+	1000	124	165 ± 10
	1400	145	205 ± 10
Si^+	550	100	95 ± 5
	750	126	115 ± 10
	1000	153	125 ± 10
	With surface damage		
	1250	180	120 ± 10
	1500	202	95 ± 15
	2000	250	25 ± 10

Figure 2 shows the measured shifts Δz from Table I as a function of the square root of both the ion energy and the ion mass. For the energy range where the nuclear energy deposition dominates the defect formation, the peak shifts indicate a square-root dependence ($\Delta z = A\sqrt{E_{ion} m_{ion}}$

(black line in Fig. 2)). In this case, the surface is nearly free of defects (cp. closed squares in Fig. 1) because the ions are prevented from close collisions with the target atoms [2]. Thus, the penetration range of the impinging ions is increased.

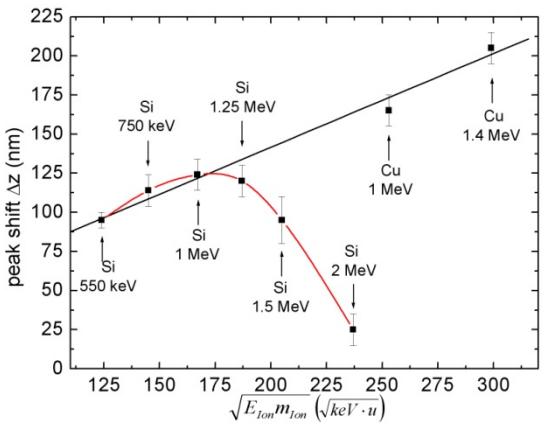

Fig. 2: Peak shift Δz as a function of the square root of the ion energy E_{ion} and ion mass m_{ion} for x-cut $LiNbO_3$ irradiated with different ion energies and ion species.

However, when defect formation at the surface occurs due to the high electronic energy deposition in this region, the peak shift decreases (cp. red line in Fig. 2). Hence, with rising ion fluence the ions experience more and more multiple scattering by the resulting defects. Finally, the near-surface region is heavily damaged, all channels are destroyed, and an amorphous surface layer is formed. As a consequence the ions behave like off-axis incident ions and the defects are formed in the same depth as for off-axis irradiation (cp. circles in Fig. 1).

After irradiation, the samples were etched in a HF solution. The etched depth relative to the surface was measured with a Sloan DEKTAK surface profilometer.

Figure 3 shows the final etched depth as a function of the square root of the ion energy for on- and off-axis-irradiation. With rising ion energy the maximum etched depth increases linearly for on- and off-axis irradiation. Compared to off-axis irradiation the maximum etched depth of on-axis irradiation is always clearly higher for all ion energies used. This behavior is reflected in the factor F_{etch}, which is always greater than 1 despite a slightly decrease from 1.4 to 1.3. On the basis of the relation

$$z_{\max}^{on-axis} / z_{\max}^{off-axis} = F_{etch} = \varepsilon_e^{off-axis} / \varepsilon_e^{on-axis}$$

and the mean value of F_{etch} = 1.35 it is obvious that the electronic energy loss in channeling conditions is reduced by a factor of 0.74 compared to off-axis irradiation.

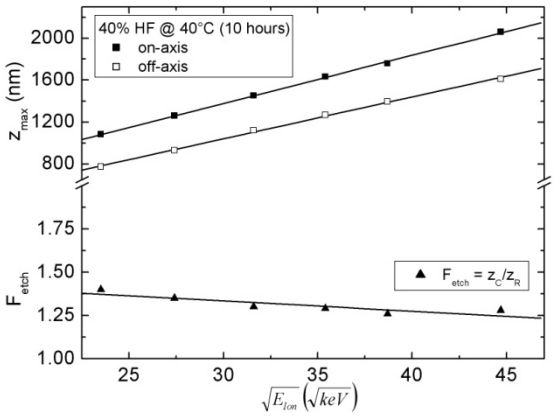

Fig. 3: Maximum etched depth z_{max} after etching in 40% HF solution for 10 h at a temperature of 40 °C for on- and off-axis Si irradiation of x-cut $LiNbO_3$ at different ion energies. Additionally, the factor $F_{etch} = z_{\max}^{on-axis} / z_{\max}^{off-axis}$ is shown.

With respect to the patterning of $LiNbO_3$ by means of ion-beam enhanced etching, the channeling irradiation offers the possibility to produce structures aligned with the crystal axis. Additionally, on-axis irradiation enables an increase in the depth of the structure (approximately 1.35 times for x- axis) without being obliged to increase the mask thickness due to the use of higher-ion energies.

References:

[1] F. Schrempel, Th. Gischkat, H. Hartung, E. B. Kley, W. Wesch, Nucl. Instr. and Meth. B 250, 2006, 164.

[2] F. Schrempel, T. Steinbach, Th. Gischkat, W. Wesch, Nucl. Instr. and Methods B 266, 2008, 2958-2961.

Ion beam synthesis of Mn/Sb clusters in silicon

M. Steinert, W. Wesch, A. Undisz[1], M. Rettenmayr[1], W.C. Nunes[2], R.P. Borges[2], M. Godinho[2], R.M. Rubinger[3], N.A. Sobolev[3]

[1] Institut für Materialwissenschaft und Werkstofftechnologie, Jena, [2]Centro de Fisica da Materia, Universidade de Lisboa, [3]Departamento de Fisica and I3N, Universidade de Aveiro

Adding the spin degree of freedom to conventional semiconductors may be achieved by the formation of diluted magnetic semiconductors (DMS) layers or the synthesis of magnetic clusters embedded in a semiconducting matrix. A promising way is ion implantation in combination with subsequent thermal treatment. We have studied the formation of Mn/Sb nanoclusters by subsequent Mn and Sb implantation into p-Si at high fluences of $1x10^{16}$ cm^{-2} and $2x10^{16}$ cm^{-2}, respectively, at elevated temperatures of 200°C or 350°C to avoid amorphization of Si. In order to achieve depth distributions with a maximum ion concentration of 1.5at% (Mn) and 3at% (Sb) at the projected range R_p = 175 nm, the implantation was performed with energies of 180 keV (Mn) and 350 keV (Sb). Subsequent thermal treatment was done by rapid thermal annealing (RTA) for 30 s at temperatures T_A ranging from 950°C up to 1350°C. The samples were characterized by means of RBS, XTEM, EDX, X-band EMR and SQUID measurements.

Amongst other things, the results of the RBS analysis shows a defect mediated redistribution of the dopants during RTA and indicate the formation of Sb containing clusters (see [1]). The formation of clusters is confirmed by cross-sectional TEM investigations (Fig. 1).

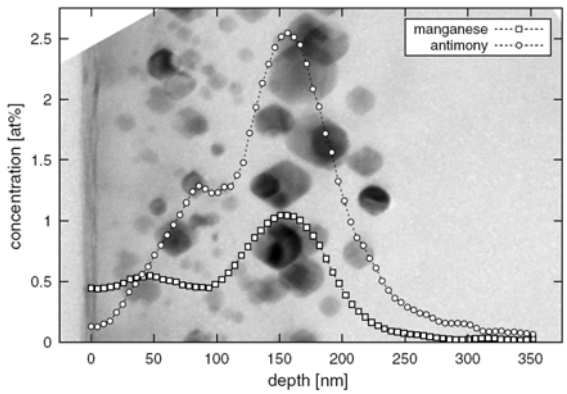

Fig. 1: Comparison of a bright-field TEM image and the RBS depth distribution of dopants of a sample implanted with Mn+Sb (T_I = 350°C, T_A = 1150°C).

The clusters exhibit a broad, dopant-concentration related size distribution with a mean particle diameter d of approximately 20 nm for annealing at T_A = 1150°C. Large particles (d > 25 nm) occur at the maximum of the dopant concentration while the smaller ones (d < 25 nm) are related to lower concentrations, which is due to the process of Ostwald ripening. With the help of EDX line scans the presence of either Sb or Mn and Sb could be detected in both types of clusters (Fig. 2).

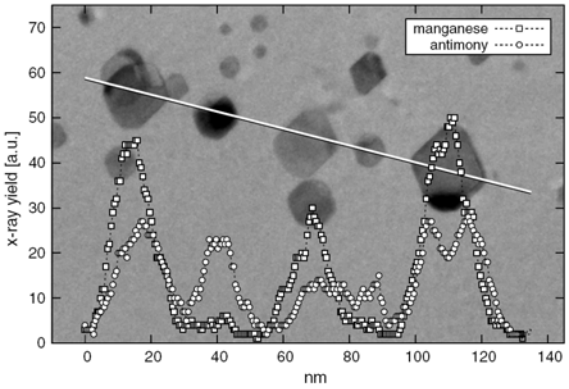

Fig. 2: EDX line scan across some particles within a sample implanted with Sb+Mn at T_I = 200°C and annealed at T_A = 1150°C.

For annealing temperatures above the melting point of bulk Mn an enhanced formation of Mn-containing particles was observed, which is in accordance with the mechanisms of cluster formation in Si formulated by Meldrum et al. [2]. Whereas inside the large particles a shift between the Mn and Sb signal indicating a phase separation between Mn and Sb was measured, no such separation could be detected for the smaller ones. High-resolution TEM analysis shows the smaller clusters to be single crystalline with a hexagonal shape with facets aligned with the Si {111} and {001} lattice planes. In several cases the clusters exhibit plane distances that match that of bulk MnSb [1]. The bright edge to be seen in some clusters is attributed to an open volume formed by the volume contraction during the

solidification process after annealing at temperatures above the melting point of bulk Sb [2].

The EMR spectra measured at 10 K exhibit resonant absorption lines with low intensities depending on the sequence of implantation of the two dopants The implantation sequences Mn+Sb at 350°C and Sb+Mn at 200°C showed a much stronger resonant absorption than the samples implanted with the sequence Mn+Sb at 200°C which is a consequence of different residual damage (see [1]). Temperature dependent EMR measurements showed a decreasing resonant absorption with increasing temperature, a broad absorption band at B ≈ 0.33 T completely disappeared at T ≥ 60 K. (Fig. 3).

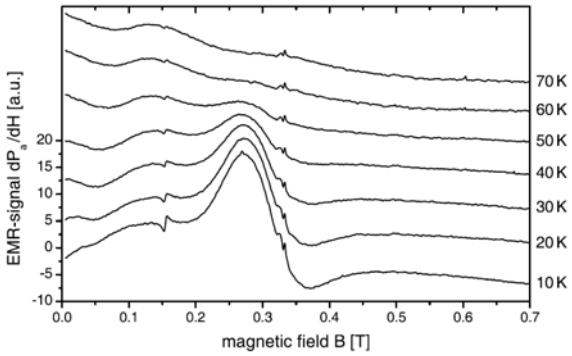

Fig. 3: X-band EMR spectra of a sample implanted with Sb+Mn (T_I = 200°C, T_A = 1150°C) at different temperatures with the external field perpendicular to the Si(100)-surface.

Furthermore, the resonance field exhibits no dependence on the orientation of the sample with respect to the external magnetic field, which could be explained by the existence of randomly oriented magnetic clusters. This assumption is supported by high resolution TEM [1].

To gain more information on the nature of the magnetic order, temperature dependent magnetization measurements in ZFC-FC modes were performed on selected samples (Fig. 4).

The shape of the ZFC and FC curves (data points) with a maximum at T ≈ 60 K in the ZFC curve and Curie-like behaviour at higher temperatures is characteristic for nanoparticle systems. In order to fit the temperature dependence of the magnetization measured, a model of non-interacting superparamagnetic nanoparticles was used [3]. This model provides a good fit for the low temperature part of the ZFC curve with a blocking temperature

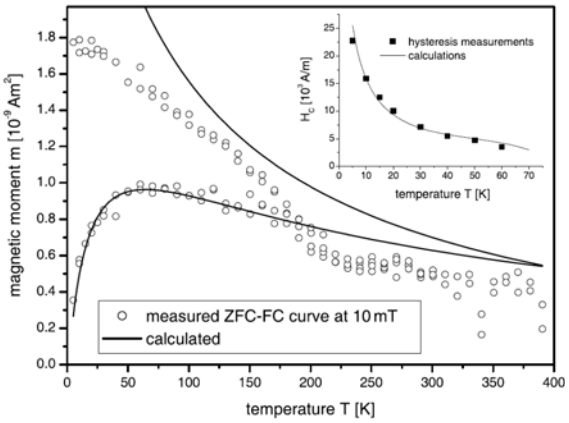

Fig. 4: ZFC-FC curve of a sample implanted with Sb+Mn and annealed at 1150°C. Inset: experimental temperature dependence of the coercive field (dots) and calculated H_c(T) curve.

T_B = 57.3 K (solid lines) which is in agreement with the vanishing EMR absorption for T ≥ 60 K (Fig. 3). The differences between experiment and calculation for the FC curve are an indication of interactions between particles. Furthermore, the deviation of the fit of the ZFC-FC curves from the experimental data at temperatures above 200 K indicates the presence of a phase transition. Possible explanations for this transition are, that at this temperature the particles go from a superparamagnetic to a simple paramagnetic state, or that a ferromagnetic phase with a Curie temperature of 200 K coexists with the superparamagnetism. In the latter case, the sum of the two signals would give rise to the magnetization curves in Fig. 4.

The low-temperature phase was also investigated by measuring hysteresis curves at temperatures between 5 K and 60 K (not shown). From these curves the temperature dependence of the coercive field was extracted and fitted considering the distribution of blocking temperatures obtained from the ZFC simulation (inset in Fig. 4). From this the average nanoparticle size was estimated to be 15 nm. This corresponds to the size of the clusters with atomic plane distances of MnSb found by the HRTEM investigations (see [1]).

References:

[1] M. Steinert, W. Wesch, A. Undisz et al., J. of Phys. D: Applied Physics 42 (2009) 035406.
[2] A. Meldrum, A. Honda, C.W. White, R.A. Zuhr, L.A. Boatner, J. Mater. Res. 16 (2001) 2670.
[3] M. Respaud et al., Phys. Rev. B 57 (1998) 2925.

Radiation damage formation in InP, InSb, GaAs, GaP, Ge and Si due to fast ions

A. Kamarou, W. Wesch, E. Wendler, A.Undisz[1], M. Rettenmayr[1]

[1] Institut für Materialwissenschaft und Werkstofftechnologie, Jena

The high electronic energy deposition caused by the interaction of swift heavy ions with solids leads to the formation of amorphous tracks in crystalline dielectrics, some metals and a few semiconductors. Among the mechanisms of damage formation in solids due to high local electronic energy transfer discussed in literature, the thermal spike model seems to be the most elaborated and useful one. This model suggests that the electronic energy is transferred to the lattice via various processes of electron-phonon coupling, which leads to an increase in the lattice temperature. If this increase exceeds the melting temperature, the material can melt and the following fast cooling down of the molten zone can freeze in the resulting damage and thus leave an ion track behind. This explains the existence of characteristic threshold values of the electronic energy deposition for track formation.

In the present contribution damage evolution and the formation of ion tracks during swift heavy ion (SHI) irradiation in InP, InSb, GaAs, GaP and Ge are investigated for irradiation with Xe or Au ions having specific energies ranging from 0.8 to 3 MeV/u. Based on these experimental results and those obtained by other authors obtained for cluster-ion irradiation of InP, GaAs, Ge and Si, extensive calculations were performed in the framework of the extended thermal spike model [1] which has been modified to perform calculations for cluster ions too (for details see [2]).

Fig. 1 shows the relative concentration of damage, n_{da}, determined from RBS spectra at a depth of 200 nm, versus the ion fluence, for 593 MeV Au irradiation of InSb, InP, GaAs, GaP, and Ge at room temperature. It is clearly to be seen that different semiconductors exhibit different radiation resistance to fast ion irradiation. InP and especially InSb are damaged very efficiently. In InP an amorphous layer ($n_{da} = 1$) is formed at $N_I \approx 10^{13}$ cm^{-2}. In the case of InSb $n_{da}(N_I)$ increases at lower fluences compared to InP, but the formation of a porous structure for fluences $N_I > 5x10^{11}$ cm^{-2} does not provide reliable data on n_{da} at higher fluences.

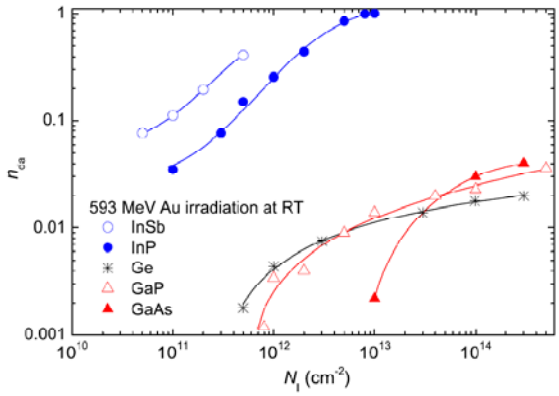

Fig. 1: Relative concentration of damage, n_{da}, at the depth of 200 nm versus the ion fluence N_I for SHI irradiation of various semiconductors.

In contrast to InP and InSb, the materials Ge, GaP and GaAs exhibit a much higher radiation resistance, the values of n_{da} for the maximum fluences used are not higher than 0.05, i.e. only 5% of the lattice atoms are displaced from their regular lattice sites. Therefore, it seems to be impossible to produce high concentration of defects in these materials by means of elemental SHI irradiation. On the other hand, it has been shown previously that irradiation with energetic cluster (C_{20} or C_{60} fullerene) ions leads to the formation of ion tracks provided that the respective energy loss is higher than the threshold of approximately 14, 31, 33, and 37 keV/nm for InP, GaAs, Ge and Si, respectively (see references in [2]). With increasing electronic energy loss, the cross section of the damaged zones (tracks) increases as well. Furthermore, TEM investigations show that in case of cluster irradiation each impinging ion forms

a (visible) track in InP, Ge, and Si, but not in GaAs. In the latter material the surface density of the ion tracks is more than one order of magnitude lower than the ion fluence used. In order to achieve a one to one ratio between track density and cluster ion fluence, GaAs has to be predamaged. This is in agreement with previous results obtained for elemental SHI irradiation of GaAs where ion tracks were detected only in predamaged samples.

Based on our own results and those obtained by other authors for cluster-ion irradiation, the maximum atomic temperature at the ion track axis, as well as the track radii, were calculated in the framework of the extended and modified thermal spike model [1,2]. In order to calculate the thermal spikes caused by elemental and cluster ions the electron diffusivity D_e in Ge and Si for individual or cluster-ion irradiation was approximated by the corresponding values for InP. For the efficiency of the electron-phonon coupling the same formula as previously used for InP was taken, and the only unknown parameter - the mean free time between two successive electronic collisions, τ_e - was determined from the track radii caused by the cluster ions. Because not each C_{60} cluster ion forms a track in GaAs, calculations for irradiation with elemental ions could not be performed for GaAs. Fig. 2 shows the results of the calculation of the maximum atomic temperature as a function of the ion energy for Au irradiation of InP, Si and Ge.

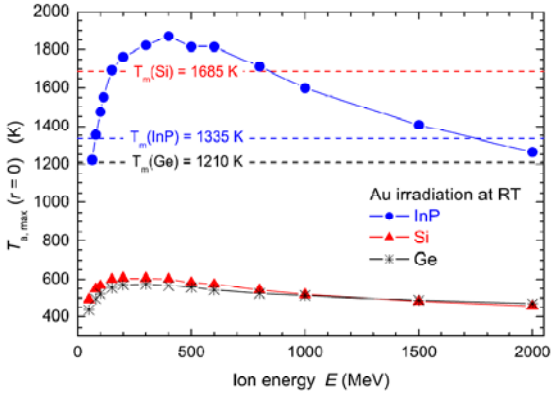

Fig. 2: Dependence of the maximum atomic temperature at the ion track axis (r = 0) on the energy of fast Au ions

In all cases the maximum atomic temperature first increases and then gradually decreases with ion energy. One can also see that only in the case of InP the maximum atomic temperature exceeds the melting temperature (dashed lines) within a broad range of ion energies. In Si and Ge the maximum temperature does hardly exceed 600 K which is far below the melting temperatures of these materials. This explains well why no continuous ion tracks were found in crystalline Si and Ge after irradiation with elemental ions.

The calculated track radii, R_{calc}, are depicted in Fig. 3 versus the experimental ones, R_{exp}, for irradiation of InP, Ge, and Si with either elemental or cluster ions.

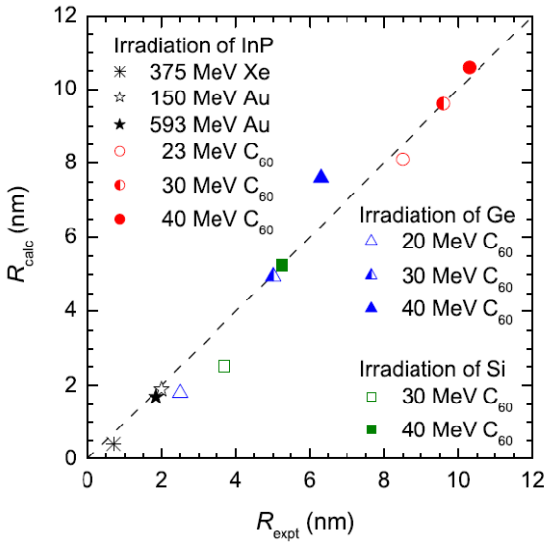

Fig. 3: Calculated versus experimental track radii for elemental and cluster ion irradiation

It is clearly to be seen that the calculated values are in good agreement with the experimental ones. Our results support the thermal spike model of track formation in semiconductors

[1] A. Kamarou, W. Wesch, E. Wendler, A. Undisz, M. Rettenmayr, Phys. Rev. B 73 (2006) 184107

[2] A. Kamarou, W. Wesch, E. Wendler, A. Undisz, M. Rettenmayr, Phys. Rev. B 78 (2008) 054111

Work supported by the DFG, contract no. WE 1707/8-1.

Thermoelastic damping on composite cantilevers

D. Heinert, C. Schwarz, R. Nawrodt, S. Kroker, A. Grib*,
W. Vodel, A. Tünnermann** and P. Seidel

**Physics Department, Kharkov National University, 61077 Kharkov Ukraine*
***Institut für Angewandte Physik, A.-Einstein-Str. 15, 07745 Jena*

Direct observation of gravitational waves demands a highly sensitive detecting setup. Optical detectors measure the influence of a gravitational wave via length changes of the arms of a Michelson interferometer. To detect a typical wave with a relative variation of the arms in the order of 10^{-23} [1] it is necessary to minimize all noise influences of the detector. In the ground based detection frequency band from 100 Hz to 2 kHz thermal noise limits the sensitivity of the detectors.

The fluctuation-dissipation-theorem [2] represents the link between a system's noise and its loss mechanisms. To achieve low noise levels it is necessary to use low loss materials at low temperatures in a detector. Therefore, the subproject C4 of the SFB Transregio 7 concentrates on measuring and understanding of energy losses in the detector's components as, e.g. the beam splitter and the end mirrors, especially at low temperatures.

Optical coatings which provide the functionality of the optics play a major role in the noise budget. For the loss mechanisms in the coatings are widely unknown, the present work investigates the contribution of thermoelastic damping of a coating as one possible loss source.

Cantilever measurements [3] allow the characterization of coating losses. The cantilever - a thin (~100 µm), rectangular monocrystalline plate - is therefore clamped on one end and electrically excited to mechanical vibrations. The amplitude of the oscillation decreases exponentially due to energy dissipation with a characteristic decay time τ^* (time to reach 1/e of the initial amplitude). The losses ϕ can then be calculated via

$$\phi^{-1} = \pi f \tau^*, \tag{1}$$

with the resonant frequency f.

After being measured the cantilever is coated and the measurement is repeated. It is possible to extract the intrinsic coating loss from these two measurements [4].

One typical mechanism of dissipation is known as thermoelastic damping (TED). This effect is caused by a mechanical deformation that induces volume changes in the sample. The compressed regions are slightly heated while the expanded regions cool down. The heat flow from the heated to the cooled regions increases the entropy of the system and leads to dissipation of mechanical energy.

The cantilever can be considered as a one dimensional beam. Zener described the TED for a homogeneous, isotropic beam. For the losses he obtained [5]:

$$\phi = \frac{E\alpha^2 T_0}{C\rho} \times \frac{\omega\tau}{1+\omega^2\tau^2}, \tag{2}$$

with the Young's modulus E, the coefficient of linear thermal expansion α, the mean temperature T_0, the specific heat C, the mass density ρ and the oscillation frequency $\omega/2\pi$.

τ represents a characteristic time depending on the thickness h of the cantilever (see Fig. 1):

$$\tau = \frac{h^2}{\pi^2} \times \frac{C\rho}{\kappa}, \tag{3}$$

and its thermal conductivity κ.

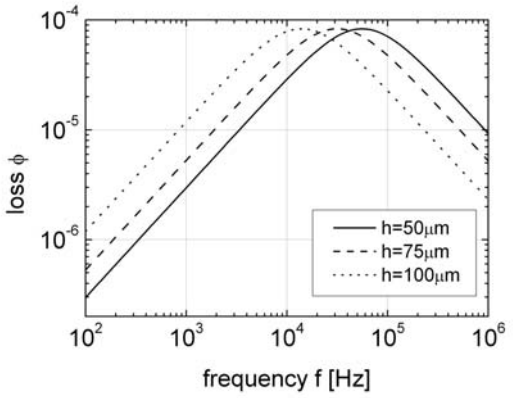

Fig. 1 The diagram shows the thermoelastic losses of a homogeneous silicon cantilever of different thicknesses after Zener. The material properties are taken at T=300 K.

An additional coating layer added to the cantilever will produce an additional TED. In order to determine this influence a numerical approach was used.

The equation of thermal conductivity is solved along the thickness z of the cantilever. The boundary conditions between substrate and coating are chosen to guarantee a continuous transition of temperature as well as heat flow. In contrast the outer boundaries are treated adiabatically with a vanishing heat flow to the environment. The resulting temperature field $\theta(z)$ allows the computation of the heat currents leading to an entropy increase and finally to dissipation:

$$\dot{E}_{diss} = -\frac{\kappa}{T_0} \times \int (\Delta\theta)^2 \, dV \, . \qquad (4)$$

In order to obtain the mechanical loss the maximum mechanical energy stored in the deformation of the sample E_{tot} is determined. The mechanical loss is then given as

$$\phi = \frac{1}{2\pi} \times \frac{E_{diss}}{E_{total}} \, . \qquad (5)$$

Using MATLAB for the numerical computations, the program was successfully tested on two references [6, 7].

The numerical results for a coated and an uncoated Si(100) cantilever at room temperature are given in Fig. 2.

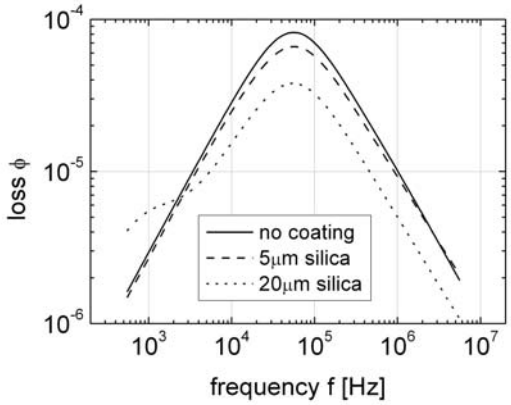

Fig. 2 Calculated TED of a 50 µm thick silicon cantilever coated with silica. The frequency behaviour was calculated using material properties at T=300 K. For coatings thinner than 5 µm only a slight but not significant decrease of losses occurred.

Our investigation of the thermoelastic damping in silicon cantilevers revealed the fact, that thin films will not change the TED significantly. Although at room temperature the measurement itself is dominated by thermoelastic damping of the cantilever the coating's influence on TED can be neglected. Therefore any change between the coated and uncoated sample in the measured losses can completely be interpreted as intrinsic to the coating material.

This work was supported by the DFG under contract SFB Transregio 7.

References

[1] R. Saulson , Fundamentals of gravitational wave detectors, World Scientific, Singapore 1994.
[2] H. B. Callen, T. A. Welton Phys. Rev. 83 (1951), 34.
[3] S. Reid et al., Phys. Lett. A 351 (2006) 205.
[4] S. Kroker 2008, Annual Report 2008.
[5] C. Zener, Phys. Rev. 52 (1937) 230.
[6] J. E. Bishop, V. K. Kinra, Int. J. Sol. Struct. 34 (1997) 1075.
[7] S. Prabhakar, S. Vengallatore, J. Micromech. Microeng. 17 (2007) 532.

4-channel cryogenic Q-factor measurement setup for silicon cantilevers

C. Schwarz, S. Kroker, R. Nawrodt, D. Heinert, R. Neubert, M. Thürk, W. Vodel, A. Tünnermann*, and P. Seidel

** Institut für Angewandte Physik, A.-Einstein-Str.15, 07745 Jena*

Dielectric coatings as being used for high reflectivity optics are known to limit the sensitivity of current gravitational wave detectors [1]. In order to enhance their sensitivity it is planned to run future detectors at cryogenic temperatures [2]. Thus, low loss bulk and coating materials are needed at low temperatures.

Thin silicon flexures (called cantilevers) with a thickness between 50 and 100 µm are well appropriate to investigate the temperature dependence of thin film loss mechanisms. The cantilevers are manufactured at the Institute of Applied Physics. On a standard 4" Si(100) wafer rectangle areas are etched down to a thickness between 50 and 100 µm using dry etching rf plasma technique. The final processing step is to cut the samples out of the wafer in the required geometry. Fig. 1 shows a schematic drawing of a silicon cantilever with characteristic sizes and crystal orientation.

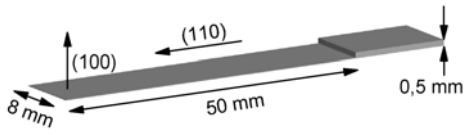

Fig. 1 Schematic drawing of the silicon cantilever used in the experiments. The thickness of the thin part varies between 50 and 100 µm.

The cantilever is clamped at the thick end using a clamp as shown is fig. 2. The combination of a thick end at the cantilever and the use of a ridge clamping structure provides a reduction of external loss mechanisms. Concerning stiffness and thermal conductivity hardened oxygen free copper, stainless steel, aluminium and titanium

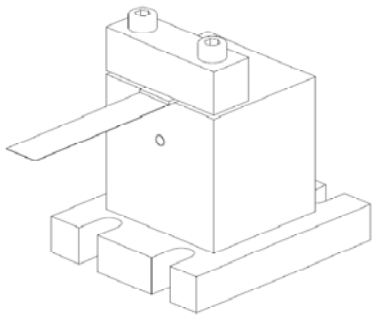

Fig. 2 Schematic drawing of the clamping structure.

were used as clamping block material. The clamping was repeated with one cantilever several times at room temperature comparing the Q-factors obtained. A possible interaction of the cantilever vibration during the ring-down experiment [3] with eigenmodes of the clamps would produce additional external losses. Fig. 3 summarises the measured Q-factors of the cantilever for different modes.

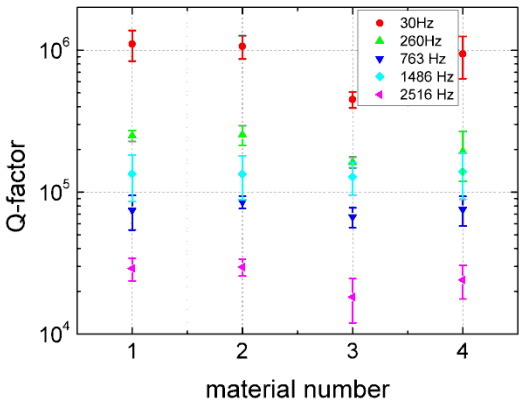

Fig. 3 Comparison of the influence of the clamping material on the measured Q-factor at 300 K.
1 – stainless steel, 2 – cooper, 3 – aluminium, 4 – titanium.

From these investigations it can be concluded that stainless steel and copper are providing good results. Especially for copper – as being a soft material – the results

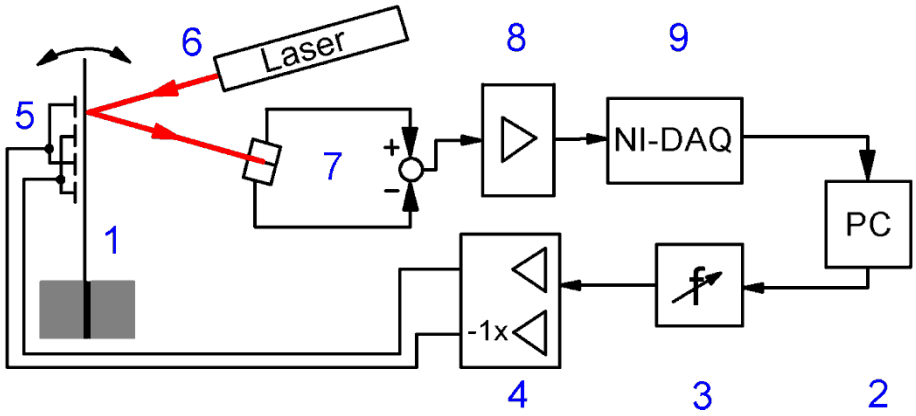

Fig. 4 Schematic drawing of the cantilever read-out system. 1 – cantilever, 2 – PC, 3 – programmable frequency generator, 4 – high voltage amplifier (0 – 1.6 kV), 5 – electrostatic driving plate, 6 – HeNe-laser (λ = 632.8 nm), 7 – split photo diode (differential readout to reduce common-mode), 8 – amplifier, 9 – high speed data acquisition card.

are surprising. Nevertheless, the possibility of using copper enables the planned investigations in a dilution refrigerator due to its high thermal conductivity at low temperatures.

Fig. 4 summarizes the vibration read-out of the cantilever. A laser beam is reflected from the cantilever surface. Its vibration is detected by a split photodiode. A sensitivity of better than 10 nm was achieved.

Due to the fact that a typical cryogenic measurement lasts several weeks the setup shown in fig. 4 was build up 4 times allowing 4 parallel measurements at once. The excitation is shared between the samples. This allows only to excite one cantilever after the other. With ring-down times expected in the range of several 100 seconds this is possible. The setup is mounted on a stiff aluminium plate (see fig. 5) and suspended in a cryostat [4] to reduce seismic vibrations.

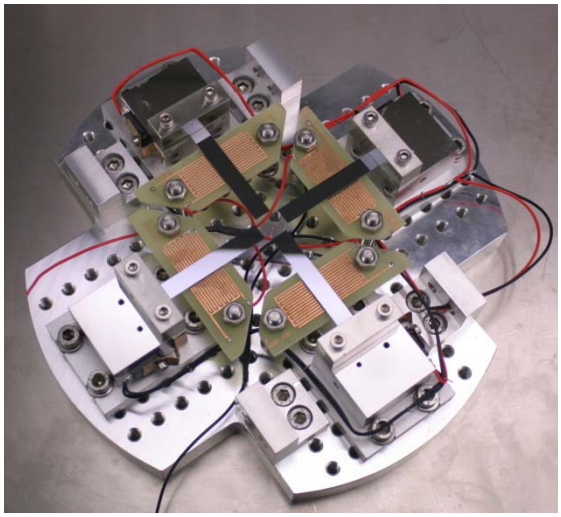

Fig. 5 Photograph of the 4-channel clamping structure equipped with heaters and 4 driving plates to excite the samples.

The first measurements on the setup were done [5]. The novel setup is able to produce 4 times more results using one single cryogenic setup. A similar setup was established at the Institute of Gravitational Research at Glasgow University within a collaboration.

This work was supported by the German science foundation under contract SFB TR7.

References:

[1] G. M. Harry et al., Class. Quantum Grav. 19 (2002) 897.
[2] www.et-gw.eu
[3] S. Reid et al., Phys. Lett. A 351 (2006) 205.
[4] R. Nawrodt et al., Cryogenics 46 (2006) 718.
[5] S. Kroker et al., Annual Report 2008.

Mechanical loss measurements of silicon cantilevers

S. Kroker, C. Schwarz, R. Nawrodt, D. Heinert, R. Neubert, M. Thürk, W. Vodel,
A. Tünnermann*, and P. Seidel

** Institut für Angewandte Physik, A.-Einstein-Str.15, 07745 Jena*

The detection of gravitational waves is one of the biggest challenges in today's science. In interferometric gravitational wave detectors laser interferometry is used to measure the position of test masses coated as mirrors. These test masses are suspended as pendulums to provide a high isolation from external disturbances. In the frequency range of interest for ground based gravitational wave detection (50 Hz – 2 kHz) thermal noise caused by the mirrors and their suspensions sets a limit to achievable detector sensitivity. Thermal noise is related to the mechanical loss [1]:

$$S_x^{\,2} \propto \phi(f,T) \times T, \qquad (1)$$

with the thermal noise spectral density $S_x^2(\phi, T)$, the mechanical loss $\phi(f, T)$, the temperature T, and the frequency f. For minimizing thermal noise of the optics, low mechanical loss substrate materials and optical coatings are desirable and need to be used at low temperatures.

Silicon is a promising candidate as material for the test masses and the suspension due to its excellent thermal properties. Thus, it is necessary to qualify its mechanical loss at low temperatures. Therefore, the project C4 of the SFB Transregio 7 is investigating mechanical losses of silicon bulk material [2] and thin cantilevers. The cantilevers are of important interest as potential structures to suspend the test masses. Furthermore, they can be used to investigate the mechanical loss of coating materials.

The mechanical loss of a silicon cantilever is determined by a ring-down technique. The sample under investigation is excited to resonant vibrations and the subsequent free exponential ring-down is recorded. Fig. 1 represents two different modes of a cantilever under investigation.

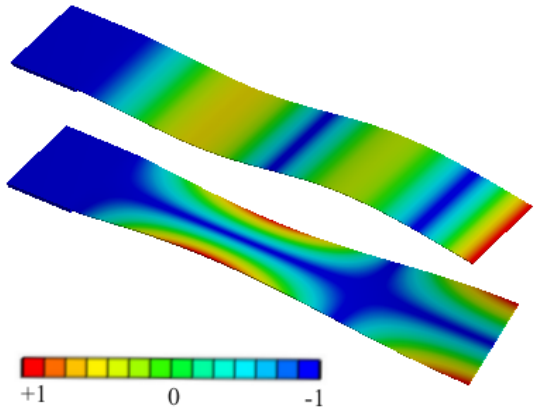

Fig. 1 Typical bending (1.2 kHz, upper shape) and torsional (2.3 kHz, lower shape) mode of a silicon cantilever (50 mm × 8 mm × 137 µm) calculated with the finite element analysis program ANSYS. The colors indicate the normalized deformation.

The mechanical loss can be calculated from the ring-down time τ (time for an amplitude decay to 1/e of the initial amplitude):

$$\phi = \frac{1}{\pi f_0 \tau}, \qquad (2)$$

with the resonant frequency f_0.

The setup is placed in a cryostat to vary the temperature in a range from 5 to 300 K. Details of the measuring technique can be found in [3].

The measured loss ϕ of the sample can be written as:

$$\phi = \phi_{internal} + \phi_{external}. \qquad (3)$$

The largest contribution to the external losses $\phi_{external}$ is gas damping which can be reduced by providing residual gas pressures of $<10^{-5}$ mbar. Clamping losses were inves-

tigated and found to be negligible [3] as well. The internal loss mechanisms $\phi_{internal}$ can also be split in different contributions:

$$\phi_{internal} = \phi_{intrinsic} + \phi_{te} . \quad (4)$$

The intrinsic loss $\phi_{intrinsic}$ arises from different internal processes like contributions of impurities, surface losses of phonon scattering. In contrast, the thermoelastic loss $\phi_{extenal}$ has its origin in the thermal properties of the material itself and is therefore a fundamental loss [4]. While the cantilever is vibrating parts of it are compressed and others are expanded. Compressed parts are heated, expanded parts cooled – a temperature gradient occurs. This gradient causes a heat flux which is the origin of the loss of mechanical energy.

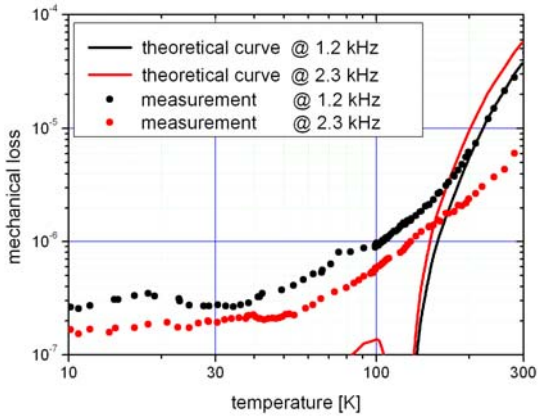

Fig. 2 Experimental results of the loss measurements for two different modes. While the bending mode (1.2 kHz) is limited by thermoelastic loss above 150 K the torsional mode (2.3 kHz) shows lower losses then limited by thermoelastic loss.

Fig. 2 represents the comparison between the theoretical calculations for the thermoelastic loss and the experimental results of the modes shown in fig. 1.
While the bending mode at 1.2 kHz is limited by thermoelastic loss above roughly 150 K the torsional mode is not effected. While in bending modes compressed and expanded regions occur a pure torsional mode has no such parts. In pure torsion no local volume change occurs and thus no thermoelastic contribution.
Theoretical calculations [4] predict to see the thermoelastic contribution clearer at higher measuring frequencies. Fig. 3 shows the results for a 19.5 kHz mode at the cantilever under investigation.

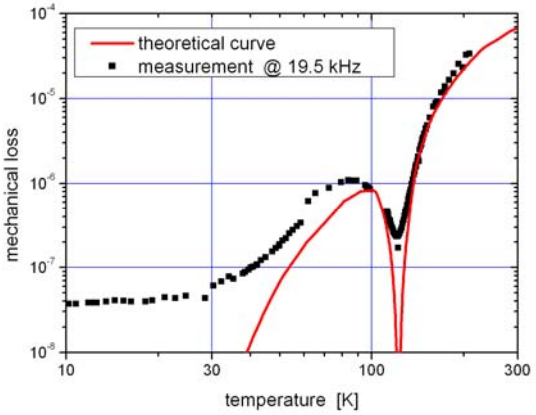

Fig. 3 At higher frequencies the thermoelastic contribution increases. The characteristic dip around 120 K occurs.

Around 120 K silicon has a thermal expansion coefficient of zero. Here, compression and expansion will not lead to heating effects. Thus, no thermoelastic loss occurs.
In all cases below 100 K other loss processes dominate and thermoelastic loss can be neglected. These losses are supposed to be the intrinsic contributions of eq. (4) and within the focus of the current investigations.
The low mechanical losses presented in this report provide the possibility to investigate the mechanical losses of coating materials applied to a cantilever with a high accuracy.

This work was supported by the German science foundation DFG under contract SFB Transregio 7.

References

[1] S. Rowan et al., Phys. Lett. A 347 (2005) 25.
[2] R. Nawrodt et al., J. Phys. Conf. Series 122 (2008) 012008.
[3] C. Schwarz et al. Annual Report 2008.
[4] D. Heinert et al. Annual Report 2008.

Investigation of the mechanical loss of silicon bulk samples

R. Nawrodt, C. Schwarz, D. Heinert, W. Vodel, A. Tünnermann*, and P. Seidel

** Institut für Angewandte Physik, A.-Einstein-Str.15, 07745 Jena*

Low mechanical loss materials are currently under investigation as test mass material for third generation gravitational wave detectors operated at cryogenic temperatures. A low mechanical loss is needed to reduce the thermal noise of the optical components and so to increase the sensitivity of these detectors. Silicon is one of the most promising candidate materials. Besides its excellent thermal and mechanical properties silicon is available in big sizes compared to other potential materials like sapphire. It is expected to use a sample mass between 100 and 500 kg in order to reduce other noise sources (e.g. radiation pressure noise) [1].

A special built cryogenic setup is used to investigate the mechanical loss within a temperature range from 5 to 300 K [2]. The samples under investigation vary in geometry. Typically, substrates with a diameter from 50 to 150 mm and thicknesses between 6 and 180 mm are used. This corresponds to a substrate mass of up to 4 kg. The test mass is suspended as a pendulum within a vacuum chamber to reduce external loss processes as much as possible (see fig. 1).

Fig. 1 Silicon sample ∅ 150 mm × 92 mm Si(100) suspended as a pendulum by means of a 75 µm tungsten wire.

The substrate is exited to resonant vibrations, the exponential amplitude ring-down is recorded and afterwards the mechanical loss determined [2]. Fig. 2 represents a ring-down of an eigenmode of a ∅ 76.2 mm × 12 mm at 15 kHz. The measurement took about 8 hours at 5.6 K. Within this time the setup needs to be thermally and mechanically stable which can be guarantied in the facilities of the SFB Transregio 7.

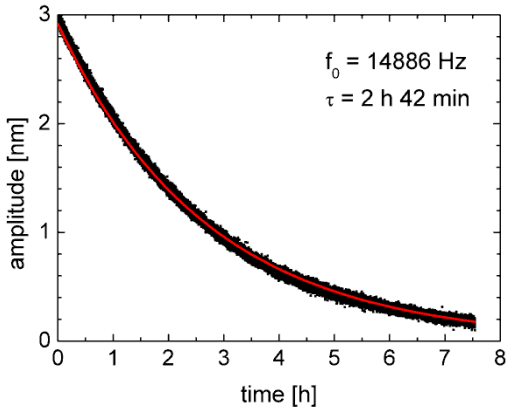

Fig. 2 Exponential ring-down of an eigenmode at 15 kHz of a ∅ 76.2 mm × 12 mm Si(100) substrate at 5.6 K.

The ring-down experiments are repeated at different modes (and therefore different frequencies) and different temperatures. Fig. 3 summarizes the results for the 12 mm thick sample. While decreasing the sample temperature the mechanical loss of the substrate decreases too. Locally there are narrow loss peaks visible. Below 15 K the mechanical loss decreases very fast reaching a

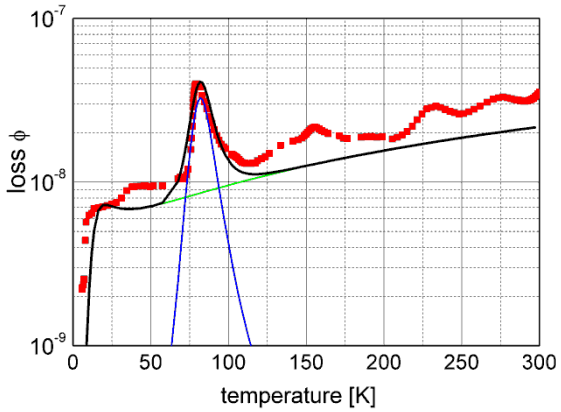

Fig. 3 Mechanical loss spectrum for the 15 kHz mode of the ∅ 76.2 mm × 12 mm Si(100) substrate.

lowest loss of 2×10^{-9} at a temperature of 5.6 K.

At low temperatures the phonon-phonon interaction plays an important role for the losses. The phonon-phonon loss is given by [3]:

$$\phi_{ph-ph} = \frac{CT\gamma^2}{\rho v^2} \times \frac{\omega\tau_{ph}}{1+\omega^2\tau_{ph}^2}, \qquad (1)$$

with the volumetric heat capacity C, temperature T, Grüneisen parameter γ, mass density ρ, sound velocity v, angular frequency ω of the vibration and phonon lifetime τ_{ph}. At temperatures below 10 K the phonon lifetime is limited by the sample geometry. The lifetime can be estimated as $t_{ph} = L/v$ with the characteristic lengths (e.g. thickness) of the sample. Thus, the right hand term in eq. (1) becomes constant for a given mode. The temperature dependence of $\phi_{ph\text{-}ph}$ is then dominated by the left hand term. The heat capacity is proportional to T^3 and thus the phonon-phonon loss should vanish like T^4 at low temperatures which is confirmed by the measurement.

At higher temperatures the phonon lifetime is limited by phonon-phonon scattering providing a frequency dependent loss. Furthermore, local peaks can be observed. These peaks are caused by impurities and microscopical transitions between different states [4]. These mechanisms can often be treated as Debye like relaxation processes [5]:

$$\phi_{relax} = \frac{\Delta}{2} \times \frac{\omega\tau}{1+\omega^2\tau^2}, \qquad (2)$$

with the relaxation strength Δ, the angular frequency ω of the vibration and the relaxation time τ. In the case of Arrhenius like excitations this parameter is dependent of the internal activation energy ΔE, the temperature T and the relaxation constant τ_0:

$$\tau = \tau_0 \times e^{\frac{\Delta E}{k_B T}}. \qquad (3)$$

ΔE and τ_0 are characteristics and can be used to identify the microscopical processes. The peak at around 80 K in fig. 3 for example gives ΔE=140 meV and $\tau_0=2\times10^{-12}$ s. This indicates a vibration of a Si-O-Si complex [6]. The sample under investigation was grown with the Czochralski method. Thus, a high oxygen concentration of 7×10^{17} cm^{-3} is present.

The other smaller loss peaks are caused by other microscopical changes of Si-O-complexes and within the focus of our current investigation.

This work was supported by the German science foundation DFG under contract SFB TR7.

References:

[1] www.et-gw.eu
[2] R. Nawrodt et al., Cryogenics 46 (2006) 718.
[3] H. E. Bömmel, K. Dransfeld, Phys. Rev. 117 (1960) 1245.
[4] A. Zimmer et al., Rev. Sci. Instrum. 78 (2007) 063905.
[5] A. S. Nowick, B. S. Berry, Anelastic Relaxation in Crystalline Solids, Academic Press, New York 1972.
[6] C. C. Lam, D. H. Douglass, Phys. Lett. 85 (1981) 41.

Comparison of the magnetic core diameter and the hydrodynamic diameter of carboxymethyl dextran coated magnetic nanoparticles

M. Büttner, S. Prass, P. Weber
F. Schmidl, G. Glöckl[1], W. Weitschies[1] and P. Seidel

[1] *Ernst-Moritz-Arndt-Universität Greifswald, Institut für Pharmazie, Jahnstraße 17, D-17487 Greifswald*

Introduction

Ferrofluids become birefringent when a magnetic field is applied perpendicular to the optical axis of light impinging the fluid, as the magnetic nanoparticles contained in the ferrofluid tend to align in the direction of the external field (Cotton-Mouton-effect). After switching off the magnetising field one can observe a relaxation of the birefringence. It has also been demonstrated that such magneto-optical relaxation measurements can be used for the determination of the hydrodynamic particle diameter. We compare the results obtained from temperature dependend magneto relaxation measurements [1] which delivers the magnetically active core size with the results of the magneto optical relaxation measurements which delivers the hydrodynamic diameter of the particles in aqueous solution.

Measurement setup

The measurement setup (Fig. 2) for the determination of the magneto-optical relaxation of ferrofluids (MORFF) consists of a laser (L), a polariser (P), aligned orthogonal to an analyser (A) and at 45° to the magnetic field axis ($\vec{H}$), a retardation plate (R) with its slow axis parallel to the polariser, a cuvette containing the sample, and a detector mounted on an optical bench (Fig. 1).

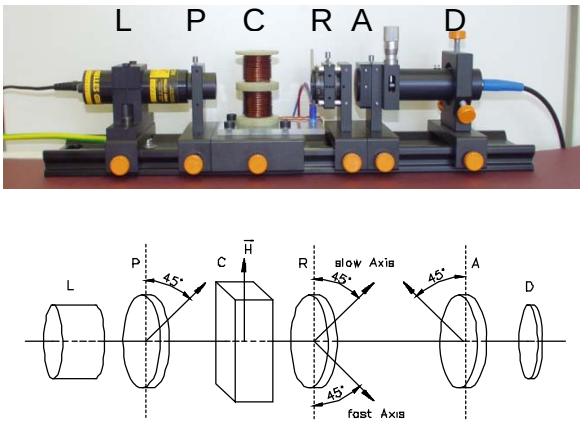

Fig. 1. MORFF measurement setup (optical bench)

The cuvette (C) is placed into a solenoid generating a variable pulsed magnetic field of up to 10 kA/m with differnet magnetisation times in the range of 1ms to 500ms. After switching off the magnetising field the relaxation of the birefringence is recorded by a PIN-photodiode connected to a variable-gain low-noise current amplifier. The sytem is controlled by a PC running LabVIEW®. An PCI-bus compatible, 12-bit multi-function I/O board collects and processes the data and controls the measurement equipment.

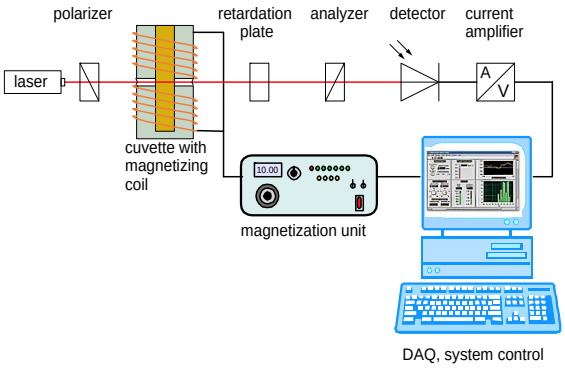

Fig. 2a. MORFF measurement setup (schematic)

Fig. 2b. MORFF measurement setup (photograph)

Investigated sample

We use for our investigations a water-based ferrofluid with a core of iron oxide and a shell of carboxymethyl dextran (pH=5.5) [2]. The iron oxide in the core is a mixture of maghemite Fe_2O_3 (58%) and magnetite Fe_3O_4 (42%) nanoparticles. The samples were fractionated using a magnetic fractionation method.

Results

Tab. 1 shows the magnetically actice core diameter (d_{core}) obtained from the temperature dependent magneto relaxation (TMRX) measurements and the hydrodynamic particle diameter (d_{hyd}) obtained from the MORFF measurements.

sample	***d_{core} [nm]***	***d_{hyd} [nm]***
100mA	**22,4**	**117**
200mA	**20,5**	**85**
400mA	**19,3**	**64**
1A	**15,7**	**53**
initial solution	**21,3**	**103**

Tab. 1. Comparation of the obtained diameters

The differences of the diameters of the samples show that the fractionation was successful. On the increase of the fractionation current the magnetically active core diameter decrease and the hydrodynamic diameter, too. This behaviour shows that the size of the magnetic core of our investigated MNP is directly linked to the hydrodynamic size of the shell in solution. This may result from the way of fabrication of the investigated MNP [3]. The results of the measurements of the initial solution show the average size of all fractions.

Acknowledgement

This work was supported by the EU project BIODIAGNOSTICS 017002.

[1] E. Romanus, T. Koettig, G. Glöckl, S. Prass, F. Schmidl, J. Heinrich, M. Gopinadhan, D. V. Berkov, C. A. Helm, W. Weitschies, P. Weber and P. Seidel, Nanotechnology 18 (2007), 115709.

[2] F. Schmidl, P. Weber, T. Koettig, M. Büttner, S. Prass, C. Becker, M. Mans, J. Heinrich, M. Röder, K. Wagner, D.V. Berkov, P. Görnert, G. Glöckl, w. Weitschies and P. Seidel, J. Magn. Magn. Mat., vol. 311 (2007), pp. 171-175.

[3] K. Wagner, A. Kautz, M. Röder, M. Schwalbe, K. Pachmann, J. H. Clement and M. Schnabelrauch, Appl. Organometal. Chem. 18 (2004), pp. 514-519.

Improvement of the spatial resolution of magnetorelaxation (MRX) measurements

P. Seidel, F. Schmidl, M. Buettner and C. Becker

In the last three years the workgroup of low temperature physics from the department of solid states was a member of the European project: Biodiagnostics (www.EU-Biodiagnostics.org). The objective of the project was to develop new medical diagnostic tools based on the most sensitive detector technologies available today. Our workgroup took part in several work packages. One task was to research and test new possibilities improving the spatial resolution of the existing MRX-system. Another task was to characterise samples of magnetic nanoparticles fabricated by another involved member of the European project Biodiagnostics.

The measurement setup for the determination of the Néel relaxation of immobilised magnetic nanoparticles consists of a single-channel second-order DC-SQUID gradiometer operating at 4.2 K and a Helmholtz coil system to magnetise the sample [1]. Our system allows us to magnetise the samples in x- and in z-direction via two pairs of Helmholtz coils. To ensure a short dead time between the switch off of the coils and the start of the measurement, a custom high power electronic regulates down the magnetic field from 1 mT to less than 10 nT in under 5 ms.

Figure 1 shows a photograph of the magnetic relaxation (MRX) system. The system includes a computer control unit which regulates the magnetisation of the Helmholtz coils, data acquisition, and sample positioning via an X-Y stage.

To reduce the number of external influence on our sensor we choose a setup with a moving sample holder. The computer controlled positioning systems moves a table (11 cm x 21 cm) under the sensor and records the relaxation signal.

To achieve our objective of improving the spatial resolution down to the mm range, we focused on two features: decrease of warm-cold distance and use of a ferromagnetic flux concentrator.

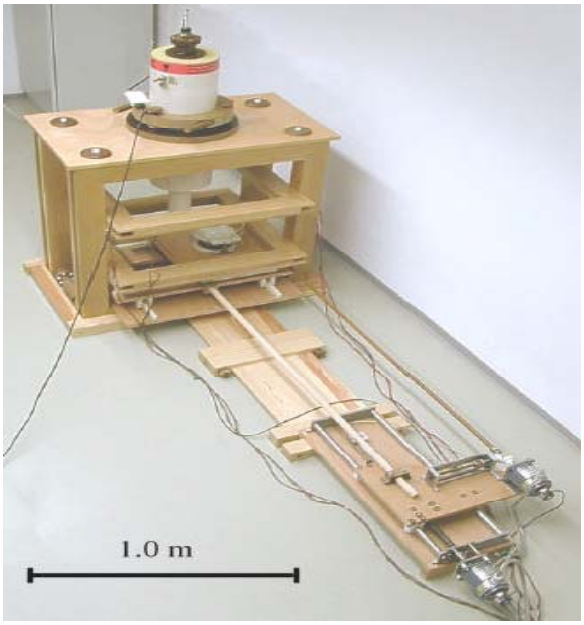

Fig. 1: Photograph of the MRX system for spatial resolved measurements

We used a custom made cryostat. To adapt the SQUID gradiometer to the new cryostat a PTFE adapter was used. The minimally achieved warm-cold distance with this cryostat is 8 mm. In the combination of the cryostat and a ferromagnetic needle as a flux concentrator MRX measurements were performed. With the results of these measurements it was shown, that the spatial resolution improved from 20 mm to less than 5 mm. The disadvantages of this setup can be described as follows.

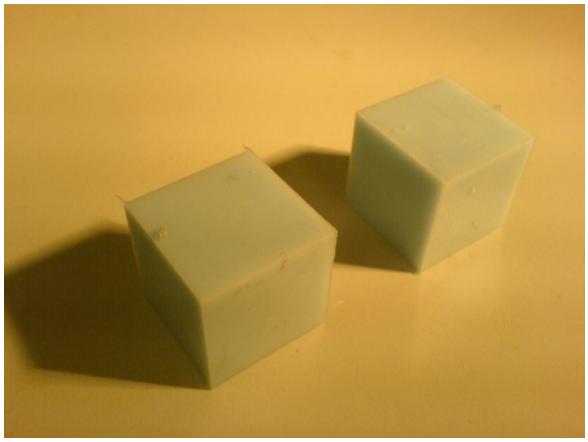

Fig. 2: Cubic phantom samples made of MNPs imbedded in a polymer matrix for spatial resolved MRX measurements.

The new cryostat can hold a liquid helium volume of 1.5 l. In considering of the reduced isolation the refill time decreases from several days down to maximal 5 hours. Only basic measurements can performed in such a small amount of time. After one measurement cycle the cryostat has to be warmed up and evacuated before the next cycle, which slows down the characterisation of the sample.

Another disadvantage is the increased level of low frequency fluctuations in the DC-SQUID signal. Only the sides of the cryostat contain mylar foil and therefore electrical shielding against external noise. This increases the amount of temperature fluctuations through helium bubbles. With no electrical shielding at the bottom, compared to other cryostats, these two influences are the main cause for the higher fluctuations.

We concentrated our efforts on measurements with our MRX system for the group at TU Ilmenau. To test the validity of new algorithms, especially focusing on the sample position spatially resolved measurements are necessary. These measurements were made with our MRX system. We started with phantom experiments of cubic sample with dimensions of 20x20x20 mm^3. These samples made of MNP imbedded in a polymer matrix. Figure 2 shows the cubic sample.

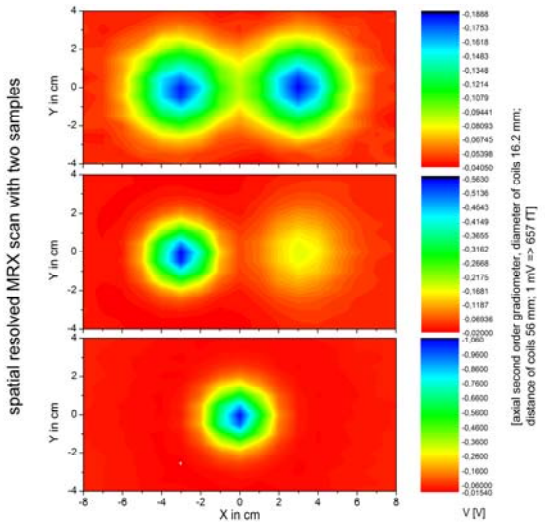

Fig. 3: MRX area scans with different samples positions. At the top the two test samples in the same height are shown. In the middle section were the samples in different height. And at the bottom the two samples arranged directly above each other with different heights. The different colours represent the strength of the magnetic field in the z-direction detecting with the SQUID measurement system in units of voltage.

Furthermore we have already carried out measurements which consisted of two samples of magnetic nanoparticles with different positions in respect to each other. The sample volume of the cylindrical teflon bin were 2x3x3 mm^3. We freeze-dried MNPs from the producer Schering A.G. with name Resovist, also known as DDM128. The samples have been arranged side by side at the same height, at different heights and directly above each other with different heights. Figure 3 shows the measurement results of the MRX area scan. The raw data of the measurements were made available to the group from Ilmenau. A key goal is to reconstruct the z position with the new algorithms.

In order to investigate the applicability of spatial resolved magnetic relaxation measurements for the determination of the signals from small samples consisting of magnetic nanoparticles, a measurement system was realised, that allows a spatially resolved detection of the relaxing magnetization of magnetic nanoparticles with a minimum size of (3×5×5) mm^3. The detection limit of the measurement system for a homogeneous distribution of MNP was found to be 0.3 nmol (17 ng) Fe.

Acknowledgement

We thank the European Union for the possibility of working in the European project Biodiagnostics 017002 (NMP4-CT-2005-017002). We are grateful for the good cooperation with the group of Prof. J. Haueisen from the Institute for Biomedical Engineering and Informatics (TU Ilmenau).

Literature

[1] E Romanus, M Höckel, C Groß, S Prass, W Weitschies, R Bräuer, P Weber, J Magn. Mag. Mater. 252 (2002) 387

Modulation anomaly of a SQUID-Gradiometer

U. Schinkel, C. Becker, K. Hoefer, A. Steppke[1], V. Grosse, S. Engmann, F. Schmidl, P. Seidel

[1]*now at: Max-Planck-Institut fuer Chemische Physik fester Stoffe, Noethnitzer Str. 40, D-01187 Dresden, Germany*

For the measurement of small magnetic fields, superconducting quantum interference devices, so called DC-SQUIDs are the most sensitive sensors. In many cases the spatial resolution of the magnetic field is an important information. Hence DC-SQUID gradiometers are measuring the orthogonal components of the magnetic field gradient. With the new layout shown in Fig. 1 we are able to measure four independent field gradients with four coupled gradiometers in two different directions. Thus the magnetic field differences $\Delta B_z/\Delta x$ and $\Delta B_z/\Delta y$ can measured Furthermore, the second order field gradient $\Delta^2 B_z/(\Delta x \Delta y)$ in the diagonal direction can be determined via a suitable software evaluation. We produced and characterized the behavior of the gradiometer [1, 3].

Fig. 2 shows the flux noise properties of the new gradiometer. In a magnetically unshielded environment the noise level increased by a factor of 8 compared to a single and double μ-metal shielding. To evaluate how an unshielded environment affects the functionality of the sensor we measured the voltage modulation of the DC-SQUID SQ1 at small fields generated with a coil placed under antenna A2. The results are illustrated in Fig. 3. Abnormal field dependences are observed. The current in the coil which induces the external magnetic field was swept from -1 mA to 0 mA. In the range from -1 mA to -0.7 mA a normal voltage modulation was observed.

However, between -0.7 mA and -0.2 mA the modulation disappears, to be recovered again in the range from -0.2 mA to -0.1 mA. The origin of this effect lies in the grain boundaries crossing the antenna structure, see Fig. 1. As the 30° grain boundary contacts have a reduced current density, we analyzed the parameter critical current in this area. The contact width of these large Josephson junctions $w_{largeJJ}$ amounts to 1200 μm. The current-voltage characteristics of the large junctions were measured by a four point contact method. For that purpose we cut one side of the antenna structure and separated the SQUID from this part. As result we get a single large Josephson junction.

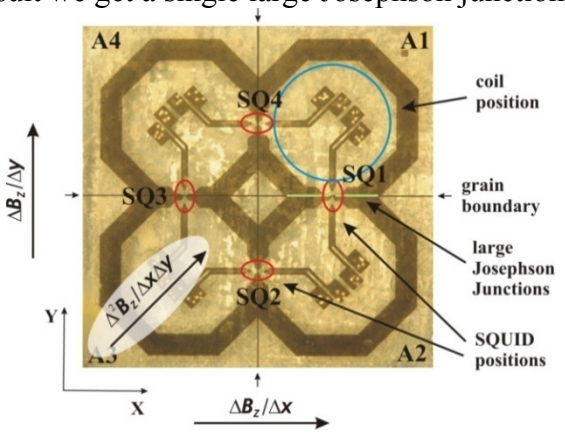

Fig. 1: *The photography shows the fabricated gradiometer. The positions of the DC-SQUIDs are marked with SQ1-SQ4 and the antennas are marked with A1-A4. The crossed bicrystal substrate has a size of 10x10 mm²*

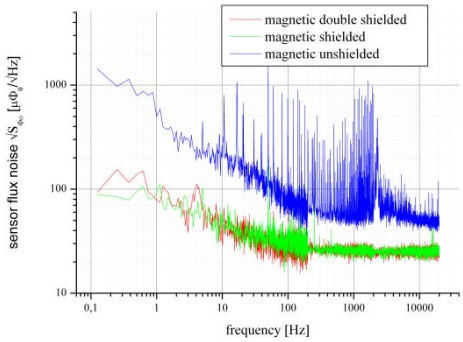

Fig. 2: Sensor flux noise for unshielded environment, with a single μ–metal shield and two μ–metal shields

The critical current density was determined to $(1.20\pm0.02)\times10^3$ A/cm². Furthermore, the influence of an external homogeneous magnetic field perpendicular to the grain boundary was investigated. The results are illustrated in Fig. 4. A asymmetric peak near ze-

ro magnetic field with a strong linear decreases of I_C on the right site were observed, indicating a typical behavior of a large Josephson junction [2]. Also beside many small asymmetric peaks are observed. Every peak present a vortex mode. By the large peak no vortex is in the junction. We calculated the ratio of the junction width *w* and the Josephson penetration length λ_J to be $w/\lambda_J \sim 100$. The voltage modulation of a DC-SQUID depends on the incoupling current through the SQUID loop. For an ordinary gradiometer on a single bicrystal substrate this current is identical to the difference in the two antenna screening currents $I_{Ant/1}$ and $I_{Ant/2}$. However, our new layout provides several paths in the whole antenna structure for a circulating screening current. So the incoupling current in a single DC-SQUID is influenced by the total distribution of the screening current in the gradiometer structure. As shown in Fig. 4 an external magnetic field reduces the critical current of a large Josephson junction formed by the grain boundary crossing the antenna. If the screening current exceeds the critical current of this junction it gets resistive.

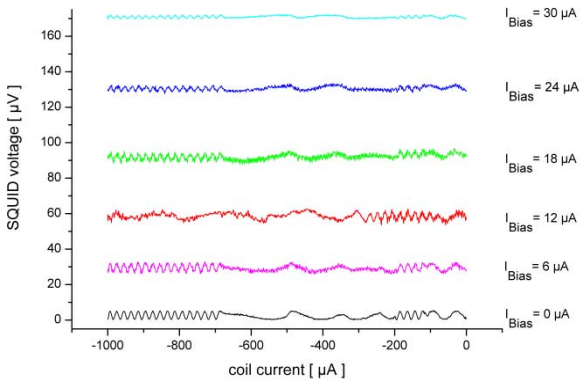

Fig. 3: *Voltage modulation anomaly of a SQUID measured for different bias currents I_{Bias}*

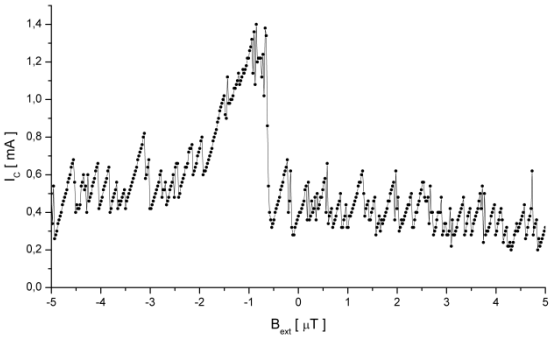

Fig. 4: *Critical current vs. external magnetic field of a large Josephson junction with $w/\lambda_J \sim 100$, which occurs as a parasitic junction within the antenna loop*

This leads to a redistribution of the screening currents and therewith the incoupling currents through the SQUID loop. This results in an abnormal voltage modulation depending on the coil current.

References

[1] A. Steppke, C. Becker, V. Grosse, L. Dörrer, F. Schmidl, P. Seidel, M. Djupmyr, and J. Albrecht, Appl. Phys. Lett., vol. 92, pp. 1122504-1- 122504-3, 2008

[2] J. Matisoo, J. App. Lett., vol. 40, pp. 1813-1820, 1968

[3] A. Steppke, Diploma thesis, Friedrich-Schiller-Universität, 2007

[4] U. Schinkel, Diploma thesis, Friedrich-Schiller-Universität, 2009

Fabrication and characterization of cobalt nanoparticles and carbon nanotubes using pulsed laser deposition and atomic force microscopy

M. Trautmann, J. Bergner, A. Bikowski, T. Schmidt, I. Sill, V. Grosse,
F. Schmidl and P. Seidel

Since their discovery in 1991 [1] carbon nanotubes (CNT) have been produced using a great variety of methods as arc discharge [2, 3], chemical vapor deposition [4] and laser ablation [5].

Besides the characterization of CNT concerning their structural, electrical and optical properties a great amount of applications, for example in nanoelectronical devices or as sensors have been reported.

Different growth modes of CNT have been discovered and different models as VLS or SLS were established to explain the growth of CNT from different carbon phases. One central factor determining the growth process is the catalyst which is necessary to dissociate and solve carbon. Different investigations showed that the liquid form of the catalyst is a basic condition for CNT growth [7, 8]. Typical growth temperatures (≈ 1000 °C) are significantly lower than the melting points of the catalyst materials (often metals as Co with T_{mb} = 1494 °C) so that this condition can only be fulfilled at low pressures or small dimensions of the catalyst particles.

In this work was used as catalyst material. The substrate material was silicon on which a 100 nm thick layer of silicon dioxide was deposited by argon sputtering because on pure silicon CNT growth is impossible due to the formation of cobalt silicide [8, 9]. In addition the oxide worked as isolating layer. A pulsed laser (KrF excimer with 248 nm wave length and 25 ns pulse duration) deposition system [10, 11] was used to prepare the cobalt layers. The cobalt layers were analyzed by XRD (information about surface roughness and thickness homogeneity), SEM (surface morphology) and AES/XPS (chemical composition). The rate of deposition Γ was determined for different laser energies, see table 1.

Laser energy [mJ]	Laser intensity [10^8 W cm^{-2}]	Γ [nm min^{-1}]
170	3.1	1.1
185	3.4	3.3
225	4.1	7.8

Table 1: Rate of deposition Γ for cobalt at different laser energies.

By annealing of the cobalt layers under vacuum conditions the formation of nanoparticles could be studied. For different initial layer thicknesses (1-10 nm), substrate materials (Si, Si-SiO_2) and annealing temperatures (300-1000 °C) the particle size distribution was determined. Therefore a special analysis technique was used. The

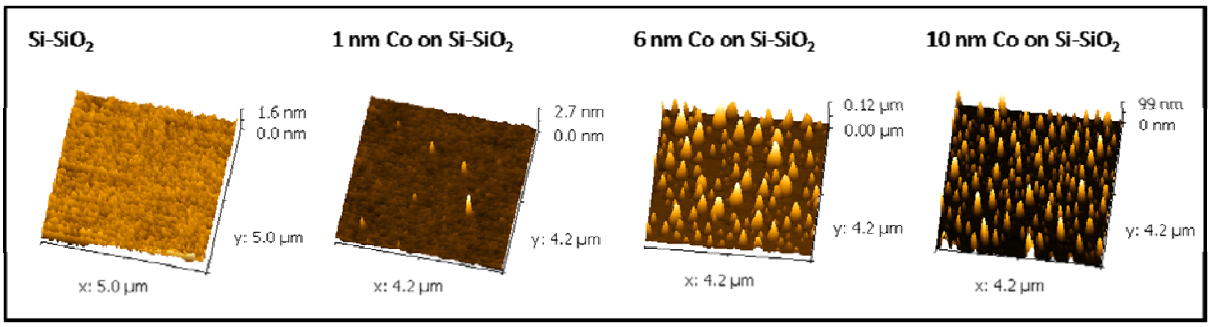

Fig. 1: AFM images of annealed cobalt layers.

surface of the annealed cobalt layers were investigated using an AFM (easyScan 2).

Figure 1 shows the surface of cobalt layers after annealing at 1000 °C. A special algorithm was used to determine the mean radii and heights of the nanoparticles. The results for a 6 nm thick cobalt layer are shown in figure 2.

There was also an investigation of surface roughness. The root-mean-square (RMS) value was measured at the different temperatures. As figure 3 represents there is a minimum of surface roughness for an initial layer thickness of 4 nm after annealing at 1000 °C which indicates a change of the layer growth mode.

No significant influence of the substrate material on the nanoparticle formation was found. Anyway, there is an influence on CNT growth. When 2 nm thick cobalt layers were given into a methane CVD reactor [12] CNT growth could only be observed on Si-SiO_2 substrate and not on pure Si. For CNT analysis Raman spectroscopy (figure 4), AFM and SEM and XPS for detection of cobalt silicide were used.

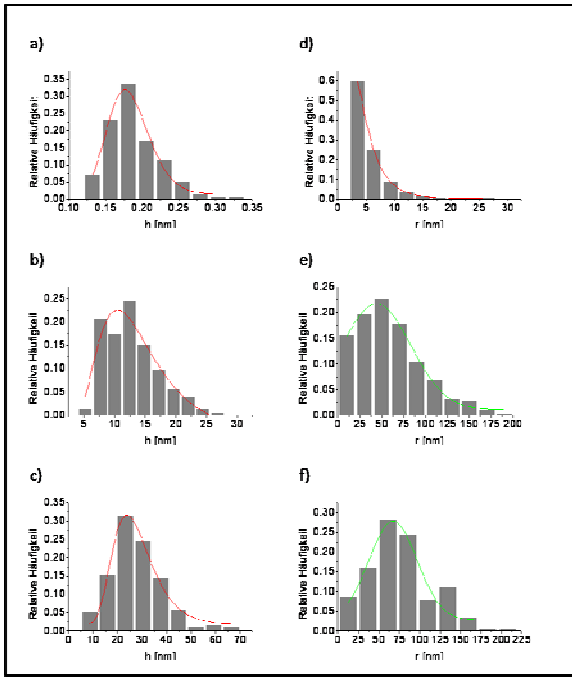

Fig. 2: Size distributions of cobalt nanoparticles (initial layer thickness 6 nm). a) Heights at 300 °C. b) Heights at 600 °C. c) Heights at 1000 °C. d) Radii

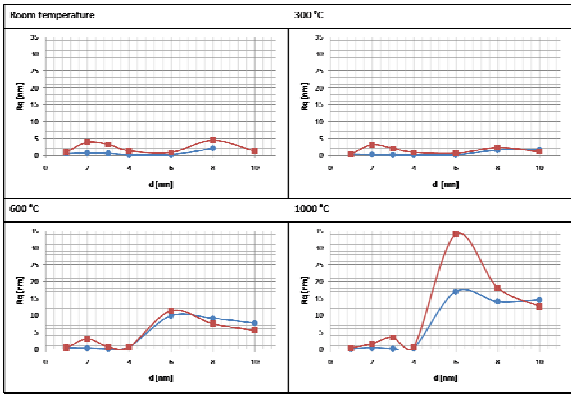

Fig. 3: RMS values Rq vs. initial layer thicknesses after different annealing steps. Blue: Co on Si-SiO_2. Red: Co on Si.

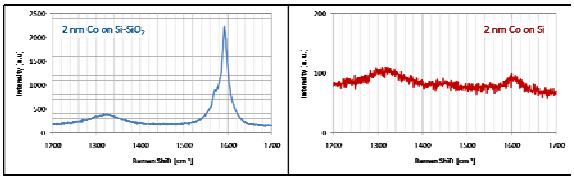

Fig. 4: Raman spectra measured on Co layers on Si-SiO_2 (left hand) and Si (right hand) after CVD.

To check the possibility of an *in-situ* growth of catalyst particles and CNT, cobalt layers were deposited and annealed in the PLD chamber and then a graphite target was ablated. The deposition rate for carbon was much higher than for cobalt at the available laser energies. The deposited carbon was analyzed by Raman spectroscopy. A nanocrystalline structure was found with a mean crystallite size of 3 nm [11, 13].

References:

[1] S. Ijima, Nature 354, 56 (1991)
[2] S. Ijima, T. Ichihashi, Nature 363, 603 (1993)
[3] D. S. Bethune et. Al., Nature 363, 605 (1993)
[4] M. José-Yacamán et. Al., Applied Physics Letters 62, 202 (1993)
[5] T. Guo et. Al., Chemical Physics Letters 243, 49 (1995)
[6] J. Meyer, Dissertation, Tübingen (2006)
[7] A. R. Harutyunyan et. Al., Applied Physics Letters 87, 051919 (2005)
[8] Y. Homma et. Al., Journal Physical Chemistry B 107, 12161 (2003)
[9] R. V. Seidel, Dissertation, Dresden (2004)
[10] C. Pansow, M. Trautmann, V. Große, F. Schmidl, P. Seidel, Annual Report (2007)
[11] M. Trautmann, Diplom Thesis, Jena (2008)
[12] T. Reichel, Master Thesis, Jena (2007)
[13] J. Bergner, Bachelor Thesis, Jena (2008)

Manipulation of quantum dots in Carbon Nanotubes by e-beam irradiation

P. Kossebau, H. Mühlig, F. Schmidl, P. Seidel

Due to the special electrical properties of carbon nanotubes (CNTs) [1], they are suitable for a lot of technical applications. An interesting field of exploration are single-electron-transistors. These structures are created by quantum dots (QDs) in carbon nanotubes. Quantum dots in CNTs are formed by defects or connection between CNTs and the metal contacts.
The measured devices are built and contacted in the group "Tieftemperaturphysik" and the CNTs are grown by CVD. The CNTs are contacted with Au. A contact is employed as a lateral gate. It is measured at 4.2 K. For the manipulation we use the focused electron beam of a scanning electron microscopy.

Experimental results

First, we measured the IV_{SD} characteristic lines for different gate-voltages and plotted the differential conductivity in a colour-scale graph (Fig 1).

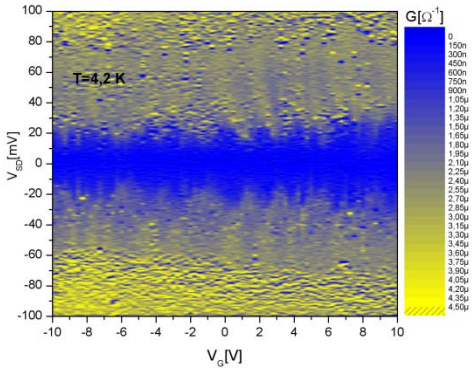

Fig. 1: Colour-scale graph of CNTs for different gate-voltages [4].

The gate-voltage V_G is located between -10 V and 10V, whereas the source-drain-voltage is applied between -100 mV and 100 mV.

In figure 1 the tips of the Coulomb-diamonds does not contact and it is built a gap of nearly 20 mV.
A possible assumption is the existence of multiple QDs in the CNTs. If the QDs have different energy levels, the tunnel-probability through the contacts is decreased and the measured current decline. The variation of the gate- voltage changes the distance of the energy-levels and the current can increase. Therefore we see the gap in the colour-scale graph.
We see a lot of tips in V_{SD}-direction, which are aperiodic in V_G-direction. The aperiodicity is typical for semiconductive CNTs or arrays of quantum dots [2]. The gap between the tips is nearly parallel and opened to greater gate-voltages.
After the irradiation by an e-beam for 20 minutes, the IV_{SD} characteristics are measured again.

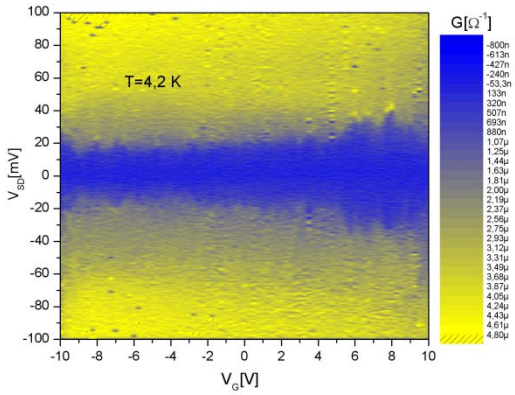

Fig. 2: Colour-scale graph of CNTs after electron irradiation [4].

The gap did not change its width or disappear, but the tips of the coulomb-diamonds are hardly visible or vanish. The coulomb-diamonds can theoretically described by the 'constant-interaction-model' [3]. We use this model to simulate a series connection of QDs (Fig 3).to compare the simulation with our measured results.

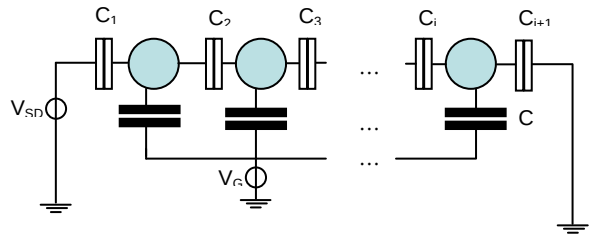

Fig 3. A series connection of quantum dots is used in the simulation

To see the occurrence of a gap in the order of millivolts for the source-drain-voltage like in our measurments, we have to use capacities in the order of 10^{-19} F to 10^{-17} F. In our simulation we use no exactly equal capacities C_1 to C_{i+1}. The result of the simulation with 8 QDs is shown in fig. 4.

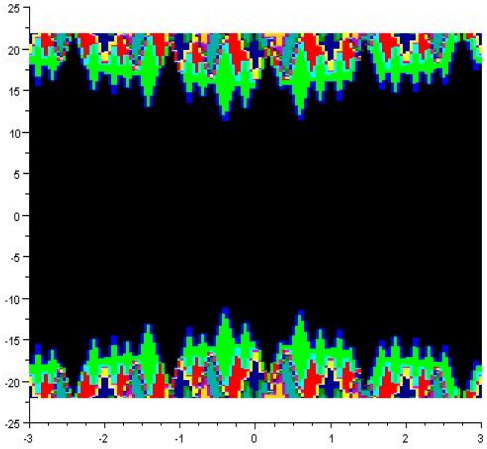

Fig. 4: Simulation of 8 QDs in series [4].

It is apparent, that a gap appeared where the differential conductivity is very small. This gap also opens to greater gate-voltages. For the notches and tips in colour-scale plot a periodicity is still visible, but the height differs. The width of the gap is depended amongst others on the number of QDs in series. Fig. 5 shows a colour-scale plot with only 4 QDs in series. The tips are more noticeable. The disappearance of tips in the V_{SD}-direction is caused by establishing of new QDs in the CNT. Our electrical measurements before and after the irradiation show the same development of a gap and a vanishing of dips.

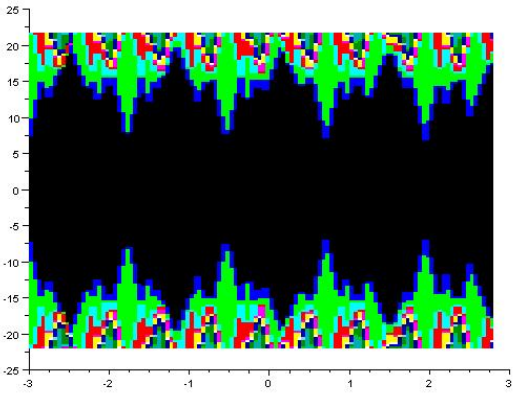

Fig. 5: Only 4 QDs in series with the same parameters as used in Fig. 4

Summary

We measured the colour-scale graph before and after the irradiation with electrons by scanning electron microscopy. The tips disappeared after the irradiation and a gap is always visible. Then we compared it with a simulation and used the ‘constant-interaction-model’. We saw, that the dips vanished with increasing quantum dot number in the simulation.

Acknowledgments

Dr. B. Schröter and the group “Dünne Schichten” are thanked for the growth of the CNTs.

References

[1] M. P. Anantram, F. Leonard., Reports on Process in Physics 69, 507 -561, 2006

[2] K. Ishibashi, M. Suzuki, S. Moriyama, T. Ida, Y. Aoyagi, Superlattices and Microstructures, Vol. 31, Nos 2–4, 2002

[3] J.M.Thijssen, H.M.S. van der Zant, physica status solidi (b) 245, No. 8, 1455–1470 (2008)

[4] P. Kossebau, Diplomarbeit, Friedrich-Schiller-Universität Jena, 2009

Application of LTS-SQUIDs in Nuclear Measurement Techniques

R. Geithner, A. Steppke, R. Neubert, W. Vodel and P. Seidel

For the upcoming FAIR (Facility for Antiproton and Ion Research) project [1] at GSI Darmstadt an improved LTS SQUID based cryogenic current comparator CCC should be developed.

In the CCC, an ion beam current I_b, which flows through a superconducting hollow cylinder, induces screening currents on the surface of the cylinder. A toroidal pick-up coil made of niobium with a ferromagnetic core is used to measure the magnetic field of these screening currents (see Fig. 1). The

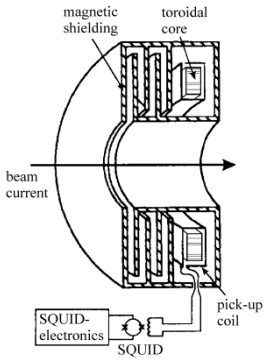

Fig. 1 Principle of a cryogenic current comparator.

signal from the coil is fed through the input coil of the readout DC SQUID *UJ 111* [2]. Extensive shielding is crucial to suppress external magnetic noise which would interfere with the magnetic signal [3], [4], [5]. In a CCC for ion beam measurements, the number of primary windings is fixed at one. Therefore, the sensitivity ultimately depends on the pick-up coil. We have shown [6] that the use of a ferromagnetic core leads to a possible optimization for better noise performance using materials with a high μ_r, as

$$B, L \propto \mu_r \Rightarrow \frac{I_s}{I_n} \propto \sqrt{\mu_r}. \qquad (1)$$

Because the signal to noise ratio is proportional to the permeability of the core, magnetic materials with high permeability, especially the nanocrystalline materials such as Vitroperm [7] and Nanoperm [8], may permit further noise reduction.

The magnetic properties of the above-mentioned materials are well characterized at room temperature, but not at temperatures down to 4.2 K. We therefore developed a setup to measure magnetic properties over a wide temperature and frequency range.

The serial inductance L_s and serial resistance R_s of the coils, made out of the differently sized toroidal-shaped cores, were measured using a commercial LCR-Measurement Bridge (Agilent E4980A). Sample temperatures in the range of 4.2 to 250 K can be adjusted using a dipstick in a helium dewar and changing the height over the liquid helium level. For a toroidal coil, the known sample geometry allows the calculation of the relative permeability μ_r from the measured L_s. We tested the temperature and frequency dependence of the relative permeabilities of both amorphous and nanocrystalline ferro-magnetic materials. Amorphous candidate core materials are the cobalt-based metallic glasses Vitrovac 6025F, and 6150F [7]. Nanocrystalline candidate core materials are the iron-based alloys Vitroperm 500F [7] and Nanoperm M033 [8].

The absolute relative permeability μ_r of our samples varied between 40,000 for Nanoperm M033 and 1,200 for Vitrovac 6150F

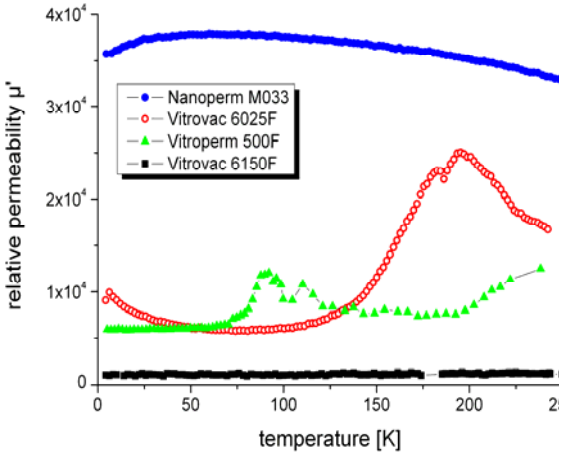

Fig. 2. Relative permeability μ_r at 100 Hz of the ferromagnetic core materials over a temperature range of 4.2 to 250 K.

(see Fig. 2). We observed different behavior for the materials during the cooling down process. We measured decreasing (Vitrovac 6025F and Vitroperm 500F) as well as increasing (Nanoperm M033) permeability with broad peaks at different temperatures. The permeability of Vitrovac 6150F was lowest and did not vary with temperature.

The frequency dependence of Nanoperm M033 and Vitrovac 6150F showed similar to the temperature dependence only small variations over a wide frequency range from 30 Hz to 100 kHz (see Fig. 3). For both Vitroperm 500F and Vitrovac 6025F the permeability decreases by at least three orders of magnitude between 30 Hz and 10 kHz.

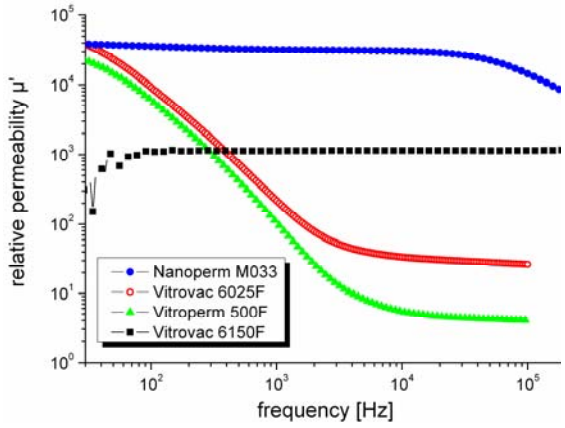

Fig. 3. Frequency dependence of the relative permeability μ_r at 4.2 K over a frequency range from 30 Hz to 100 kHz.

For the noise characterization we used superconducting niobium wires as the coil windings. The wires were connected to the input coil of a DC SQUID *UJ 111*, electrically and magnetically shielded with a lead cylinder against external fields. At 4.2 K the DC SQUID was used in flux-locked loop mode as a current sensor using a commercial SQUID electronics and the noise currents of the samples was recorded with a HP 35670A spectrum analyzer. The base noise level, measured with shunted input coil, shows no frequency dependence down to 5 Hz (see dashed line in Fig. 4). We found that both materials had a 1/f noise behavior with different slopes up to corner frequencies of 200 Hz for Nanoperm M033 and 1 kHz for Vitrovac 6025F (see Fig. 4). In the frequency range of 1 Hz to 1 kHz Nanoperm M033 has a significantly less total noise (7.1×10^{-3} V) compared to Vitrovac 6025F (10.4×10^{-3} V).

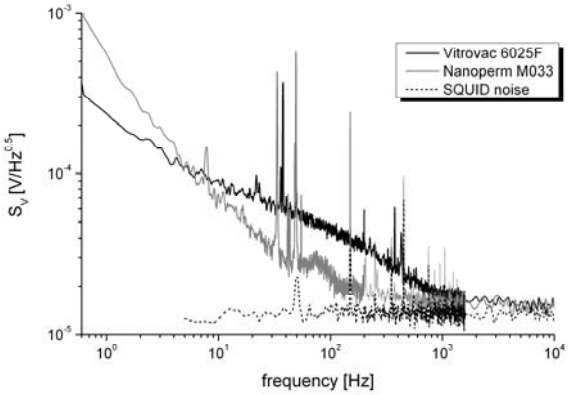

Fig. 4. Voltage noise at SQUID electronics output for Vitrovac 6025F and Nanoperm M033 cores connected to the SQUID input coil. The dashed line represents the SQUID noise level with a shunted input coil. The noise spectra were recorded with the sample and the SQUID at 4.2 K.

The properties of the ferromagnetic core material set the fundamental limits for noise reduction in a CCC. According to our measurements nanocrystalline alloys, such as Nanoperm, present significant advantages for the CCC due to their high permeability over a wide frequency range and low noise level at liquid helium temperatures. In further measurements we will complement these results with focus on samples with highest possible permeability currently available.

References

[1] Facility for Antiproton and Ion Research (FAIR), homepage. Available: http://www.gsi.de/fair/.

[2] W. Vodel, K. Mäkiniemi, *Meas. Sci. Technol.*, vol. 3, pp. 1155-1160, 1992.

[3] W. Vodel, R. Neubert, S. Nietzsche, K. Knaack, K. Wittenburg and A. Peters, *IEEE Trans. Appl. Superconductivity*, Vol. 17, 2007, pp. 621-624

[4] K. Grohmann, et. al., *Cryogenics* 16, July 1976, pp. 423-429.

[5] K. Grohmann, et. al., *Cryogenics* 16, October 1976, pp. 601-605.

[6] A. Steppke, R. Geithner, S. Hechler, R. Nawrodt, R. Neubert, W. Vodel, M. Schwickert, H. Reeg, and P. Seidel, *Applied Supercond. Conf.*, 2008, Chicago, USA

[7] VACUUMSCHMELZE GmbH & Co. KG, Gruener Weg 37, D-63450 Hanau, Germany.

[8] MAGNETEC GmbH, Industriestrasse 7, D-63505 Langenselbold, Germany.

Electric Field and Strain Effects on the Dielectric Properties of Epitaxial Strontium Titanate

V. Grosse, S. Engmann, F. Schmidl and P. Seidel

Nano-scaled ferroelectric materials offer a wide range of applications, e.g., as functional layer in tuneable microwave and memory devices or as high-k gate dielectric [1-3]. Thus, understanding their dielectric behaviour is a key topic of modern research. Strontium titanate (STO) as an incipient ferroelectric takes a special position among these materials. In bulk STO quantum fluctuations suppress the ferroelectric phase transition and it remains paraelectric down to temperatures below 0.035 K [4]. However, the dielectric properties of thin films are significantly influenced by boundary conditions and inhomogeneities such as misfit strain gradients and internal electric fields. Here we present an approach to model our temperature and field dependent measurements of the static dielectric permittivity of STO thin films.

Our samples were grown on $LaAlO_3$ single crystal substrates by pulsed laser deposition as a tri-layer system $YBa_2Cu_3O_{7-x}$/STO/Au. The STO layer was grown at 800°C in a 15 Pa oxygen atmosphere. The energy density of the KrF laser was 0.9 J/cm^2. Film thickness was varied in the range of 68 to 165 nm. X-ray diffraction proofed good epitaxy with an average rocking-curve width of 0.4°. However, this is almost double the value found for tri-layer systems deposited on STO substrates. We explain this effect by misaligned domains in the $LaAlO_3$ substrates due to twinnings. This negatively affects orientation of the $YBa_2Cu_3O_{7-x}$ (YBCO) and subsequently of the STO layer.

Compressive epitaxial misfit strain in the a-b plane leads to an enlargement of the c-axis of the STO layer by up to 0.7%. This strain relaxes exponentially with film thickness d, see figure 1. However, for d>130 nm an additional peak in the ω-2θ scan indicates a small highly strained volume fraction presumably emerging at the YBCO-STO interface.

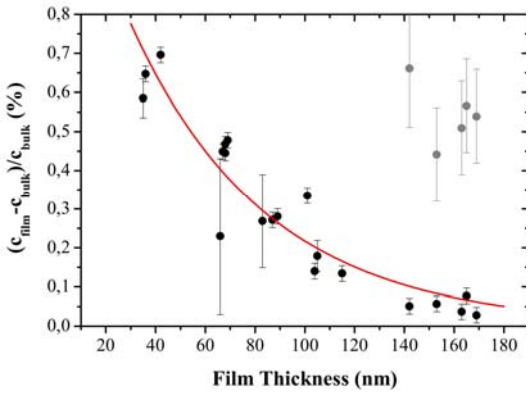

Fig. 1: Exponential relaxation of the c-axis of the STO layer with film thickness (•). Above 130 nm a thin highly strained layer emerges at the YBCO-STO interface (•).

After deposition the tri-layer system was patterned to parallel-plate capacitor like structures utilising standard photolithography and ion beam etching. The capacitance of this system was measured in the temperature range from 4.2 to 300 K using an Agilent 16056C LCR-meter. From this the dielectric permittivity ε_r can be derived by the well known relation $C=\varepsilon_0\varepsilon_r A/d$ (ε_0 - permittivity of free space, A - capacitor area).

To qualitatively describe this behaviour we used an order-disorder model for a two level system which was first proposed by Blinc and Zeks [5] and then applied to strain free STO single crystals by Hemberger et al [6]. Including an external electric field E this model yields an Ising-type Hamiltonian in the form:

$$\mathbf{H} = -\Omega\sum_i S_i^x - \frac{1}{2}\sum_{i,j} J_{i,j} S_i^z S_j^z - 2\mu E\sum_i S_i^z \quad ,(1)$$

Here S_i^α are the Pauli spin-operators, Ω is the tunnelling integral describing quantum mechanical fluctuations, $J_{i,j}$ is the dipole-dipole coupling constant and μ is the dipole moment.

Within the mean-field approximation one yields for the thermal average of S_i^z:

$$\left\langle S^z \right\rangle = \frac{1}{2} \frac{J_0 \left\langle S^z \right\rangle + 2\mu E}{H} \tanh\left(\frac{H}{2k_B T} \right) \qquad (2)$$

with $H = \sqrt{\Omega^2 + \left(J_0 \left\langle S^z \right\rangle + 2\mu E \right)^2}$.

The macroscopic polarisation then calculates to $P(E) = 2n\mu \left\langle S^z \right\rangle$ and the dielectric susceptibility can be derived as follows:

$$\chi = \frac{1}{\varepsilon_0} \frac{\partial P}{\partial E}. \qquad (3)$$

For high electric fields this model predicts a $\varepsilon_r(T)$ characteristic similar to that of our measurements showing a distinct maximum at a temperature that varies with the applied field. For our samples the origin of this field is a band alignment due to the difference in work function of the YBCO and Au electrodes. This assumption is confirmed by field dependent measurements of ε showing a maximum at bias voltages of 1 to 1.2 V were the internal fields are compensated.

However, the above introduced model does not explain the absolute values of the dielectric permittivity for our samples since it does not include structure imperfections and strain effects. The influence of an enlarged c-axis on the room temperature value of ε_r is shown in figure 2. It is important to note that we assumed the value of the strained interfacial layer in the cases of our samples with a film thickness d>130 nm since this layer dominates the dielectric behaviour in a series connection with the otherwise unstrained film.

These findings are contrary to the theoretical predictions of Pertsev *et al*. [7]. They propose a Curie-Weiss like increase of the dielectric permittivity with compressive in-plane strain. However, there are two possible scenarios which might explain this behaviour. First, the above mentioned band alignment leads to high electric fields at the YBCO-STO interface and

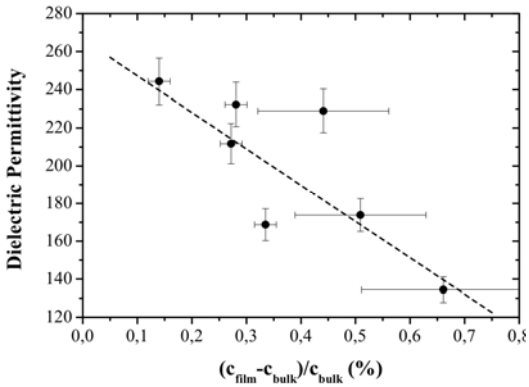

Fig. 2: Dependence of the dielectric permittivity at room temperature on the relative elongation of the STO c-axis

thus to a reduction of ε_r. The same field then originates the enlarged c-axis by a piezoelectric effect [8]. On the other hand a stress induced c-axis enlargement could cause a build-in electric field which saturates the dielectric permittivity [9].

In conclusion, we investigated the dielectric properties of STO thin films grown by PLD. The temperature and electric field dependence of the dielectric permittivity can qualitatively be described by a quantum mechanical Ising-type model. Deviations from this model can be attributed to strain and field induced enlargements of the STO c-axis.

References:

[1] Tagantsev AK, Sherman VO, Astafiev KF, Venkatesh J and Setter N 2006 *Journal of Electroceramics* **11** 5-66

[2] Scott JF 1998 *Annual Review of Materials Science* **28** 79-100

[3] Dawber M, Rabe KM and Scott JF 2005 *Review of Modern Physics* **77** 1083-130

[4] Müller KA and Burkhard H 1979 *Physical Review* B **19** 3593-602

[5] Blinc R and Zeks B 1972 *Advances in Physics* **21** 693-757

[6] Hemberger J, Lunkenheimer P, Viana R, Böhmer R and Loidl A 1995 *Physical Review* B **52** 13159-62

[7] Pertsev NA, Dittmann R, Plonka R and Waser R 2007 *Journal of Applied Physics* **101** 074102

[8] Lübcke A, Lötzsch R, Uschmann I, Grosse V, Schmidl F, Förster E and Seidel P, *to be published*

[9] Bouzehouane K, Woodall P, Marcilhac B, Khodan AN, Crété D, Jacquet E, Mage JC and Contour JP 2002 *Applied Physics Letters* **80** 109-11

Pulsed Laser Deposition of Superconducting Niobium

V. Grosse, C. Pansow, A. Steppke, F. Schmidl and P. Seidel

Today, niobium (Nb) thin films are basis for a wide range of superconducting applications such as RF cavities or superconducting quantum interference devices. They are commonly grown in high quality by electron beam evaporation or sputtering. However, these techniques have their drawbacks. For example, the mean free path of an electron is reduced for sputtered Nb thin films with respect to bulk material. It is expected that a higher ionisation state and energy of the evaporated particles will improve film quality [1]. This demand on the deposition process is perfectly met by pulsed laser deposition (PLD).

Here we present first results on the superconducting properties of Nb thin films grown by PLD on Si (001) substrates at room temperature. The deposition chamber was evacuated to a residual pressure of $2 \cdot 10^{-5}$ Pa. Laser pulses of a KrF excimer laser (wave length 248 nm, pulse duration ~25ns, repetition rate 10 Hz) were focused onto a Nb target to a spot size of 1.5×3 mm^2. The distance between target and substrate was 3 cm in an on-axis geometry.

From measurements of the growth rate dependence on laser fluence we can estimate the ablation threshold to be 5.7±0.5 J/cm^2. However, we achieved best superconducting properties with a critical temperature of up to 8.4 K for films grown at laser fluences of at least 7.1 J/cm^2. We attribute this effect to a reduced oxidation during film growth. Please note that in our set-up we were not able to achieve laser fluences of more than 8.9 J/cm^2.

For further characterisation of our films we measured the temperature dependence of the critical current density. The results in comparison with an electron beam evaporated (EBE) sample are shown in figure 2. Within the two-fluid model based on Ginzburg-

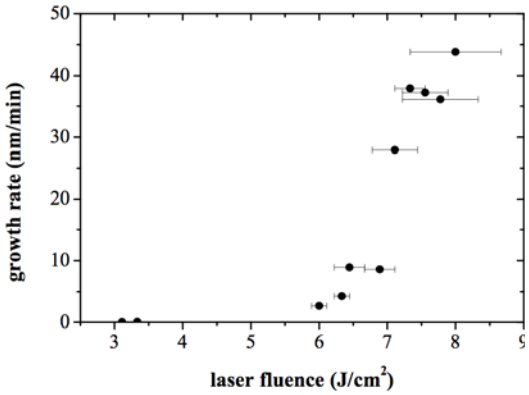

Fig. 1: Growth rate of Nb thin films in dependence on laser fluence. The ablation threshold is estimated to be (5.7±0.5) J/cm^2.

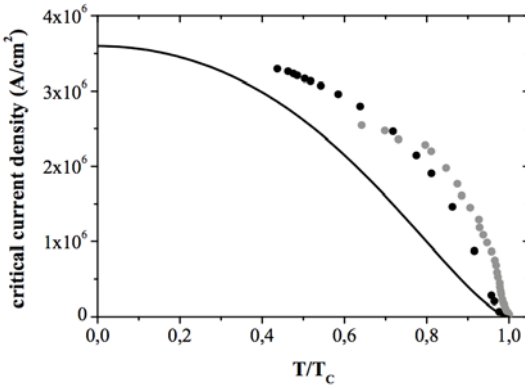

Fig. 2: Temperature dependence of the critical current density of a sample grown by PLD (●) and by electron beam evaporation (●). The solid line corresponds to the theoretical prediction given by equation (1) with a critical current density at zero-temperature of $j_C^0 = 3.6 \cdot 10^6$ A/cm^2.

Landau theory the $j_C(T)$ dependence is given by [3]:

$$j_C(t) = j_C^0 (1 - t^2)^{3/2} (1 + t^2)^{1/2}, \qquad (1)$$

with $t = T/T_C$. In contrast to the findings of Il'in *et al.* [2] our data for both samples does not follow theoretical predictions. Close to the phase transition the critical current density increases steeply with decreasing temperature and saturates at a zero-temperature value of $j_C^0 \approx 3.6 \cdot 10^6$ A/cm^2. This behaviour can be understood by assuming percolating currents in a granular structure. X-ray dif-

fraction measurements revealed a broad Nb (110)-peak suggesting that our samples are polycrystalline. We calculated the average grain size from the profile width of the (110) reflection to be 10±1 nm using the Scherrer formula [4]. The integral reflectivity for the EBE sample, however, is significantly lower than for the PLD samples. We attribute this to amorphous intergranular regions. The volume fraction of this amorphous Nb then is higher for the EBE sample.

In this special structure supercurrents cross regions of different critical temperature and critical current density. At boundary surfaces between these regions Josephson effects can be expected. Hence, the integral temperature dependence of the critical current in our samples is affected by several competing processes. Further theoretical analysis is necessary to explain our findings shown in figure 2.

The granular structure of our samples also affects the temperature dependence of the upper critical magnetic field $B_{C2}(T)$. In the dirty limit ($L_{eff} << \xi_0$), where L_{eff} and ξ_0 is the electronic mean free path and the intrinsic coherence length, respectively, $B_{C2}(T)$ can be written in the form [5]:

$$B_{C2}(T) = \frac{\phi_0}{2\pi[\xi_{GL}(T)]^2}, \qquad (2)$$

where ϕ_0 is the flux quantum. With the temperature dependence of the Ginzburg-Landau coherence length ξ_{GL} near the phase transition ($T \rightarrow T_C$):

$$\xi_{GL}(T) = 0.85\sqrt{\frac{\xi_0 L_{eff}}{1 - T/T_C}} \qquad (3)$$

B_{C2} is a linear function of temperature in the vicinity of T_C. Our measurements shown in figure 3 are in good agreement with this theory. Within this model the slightly increased slope of the $B_{C2}(T)$ dependence of the samples grown by PLD in comparison

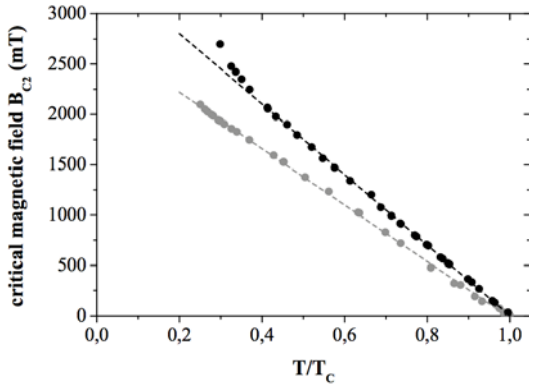

Fig. 3: Temperature dependence of the upper critical magnetic field B_{C2} of a PLD grown sample (●) and an electron beam evaporated sample (●). Dashed lines are linear fits to our data according to equations (2) and (3).

with the EBE sample can be related to a reduced mean free path caused by slightly smaller grains and niobium oxide phases within the film.

We should note that at low temperatures equation (3) looses its validity. It is thus not possible to explain the temperature dependence of the upper critical field for $T \rightarrow 0$. Models based on Ginzburg-Landau theory predict a saturation at finite values $B_{C2}(0)$ [6]. In contrast to that the $B_{C2}(T)$ characteristics of the PLD grown sample deviates from the linear dependence to higher values. It is therefore necessary to extend our measurements to lower temperatures to further investigate this behaviour.

References:

[1] Catani L *et al* 2006 *Physica* C **441** 130-3
[2] Il'in K, Siegel M, Semenov A, Engel A and Hübers H-W 2005 *Phys Stat Sol (c)* **2** 1680-7
[3] Skocpol W J, Beasley M R and Tinkham M 1974 *J Appl Phys* **45** 4054
[4] Warren B E 1969 *X-Ray Diffraction* (New York: Dover Publications) p 251
[5] Tinkham M 1996 *Introduction to Superconductivity* (New York: McGraw Hill)
[6] Helfand E and Werthamer N R 1966 *Phys Rev* B **147** 288-94

Electrical and Optical Properties of Single-Walled Carbon Nanotubes Characterised by Scanning Probe Microscopy and Raman Spectroscopy

H. Kleemann, B. Schröter

For nearly 20 years Carbon Nanotubes (CNTs) are in the center of scientific interest. Especially Single-Walled Carbon Nanotubes (SWCNTs) are an exciting one-dimensional quantum system with exceptional mechanical, electrical and optical properties. However, the determination of this properties and the chirality for an isolated SWCNT is still a problem with common techniques like Scanning Force Microscopy and Confocal Raman Spectroscopy.

We have grown high purity SWCNTs on various substrates like fused silica and silicon dioxide on silicon as well as on single crystalline surfaces like sapphire and quartz by chemical vapour deposition (CVD) using methane or ethanol as precursor gas. The CNT density can be varied by the temperature, precursor gas pressure and catalyst type. Isolated nanotubes on substrates of high purity without any amorphous carbon can be produced by this method.

Modified Atomic Force Microscopy (AFM) techniques are used to characterise the mechanical and electrical properties of such tubes. To investigate the CNT substrate interaction and the elastic modulus of the nanotubes we work with an AFM (N*anosurf easyscan II*) in contact mode. Low scan forces (<10nN) are necessary to prevent shifting the CNTs by the AFM tip. By a special linescan procedure we measure the height of a tube while increasing the scan force from 1nN up to 30nN. A radial deformation with increasing force is detected (see Fig. 1)

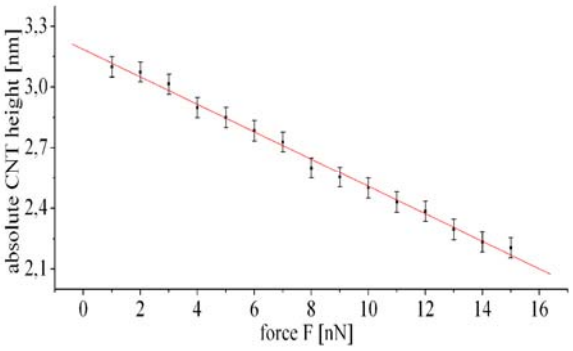

Fig. 1: Radial deformation of a CNT on fused silica, bending constant 0,07nm/nN [1]

The radial deformation of the tube diameter reaches up to 40% of the free tube diameter. The tubes show a linear, elastic deformation which is reversible (see Fig. 2.(a)). A bending constant is given by linear regression of the height-force-curve. The direct detection of the CNT deformation is possible because of the high cantilever constant (5nm/nN) and the incompressibility of the substrate.

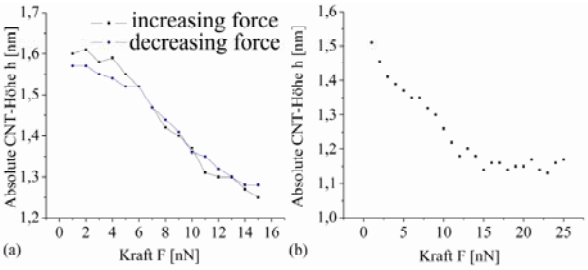

Fig. 2: Reversibility (a) and saturation (b) of radial deformation by forces up to 25nN [1]

A saturation effect, as shown in Fig. 2(b), is observed, when the tube height is smaller than 1.1nm. This effect is based on the π-electron repulsion, so that the CNT height cannot get below 0.6nm. As supposed by [2] the saturation height could be used to distinguish single-walled from double-walled CNTs. The bending constant versus the CNT height h is measured for tubes in the range from h=1.2nm up to h=5nm. The deformation is linear and the bending constants increase with increasing CNT height as shown in Fig. 3. The linear behaviour between the bending constant and the tube radius clarifies the instability of tubes with big diameter. Consequently, the preferred growth of CNTs with small diameter is not only affected by the size of the catalyst particles, but also by higher stability of small tubes. These measurements confirm that tubes on substrates are deformed just because of the CNT-substrate interaction forces which which can be as high as 30nN. This emphasizes the impact of the surface forces on the CNT properties. The technique used to measure the radial deformation is very sensitive to individual CNTs, the determined bending constants have small errors. The high radius of curvature of the AFM tips (>15nm) ensures

that the observed deformation is nearly unaffected by the geometric structure of the tip.
Furthermore, the characterisation of electric CNT properties by AFM is possible. We have coated standard AFM tips with palladium or nickel for direct electric measurements on individual tubes and indirect measurements of the polarizability.

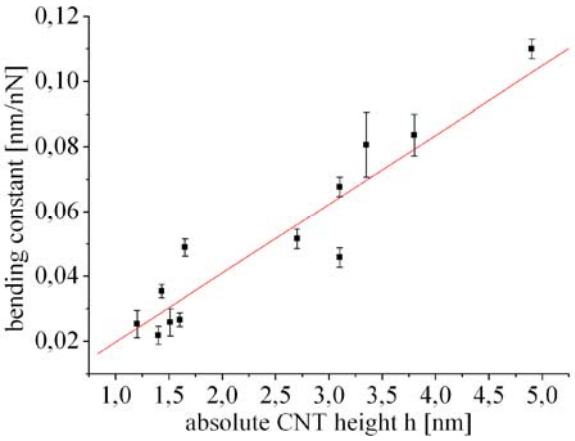

Fig. 3: Bending constant versus CNT height [1]

Based on the difference of the electrostatic polarizability between semiconducting and metallic CNTs it is possible to distinguish them by non-contact AFM with a static tip bias (-5...+5V) [3]. The local polarisation field and the polarisation charge is the reason for an increasing tip-CNT interaction. In consequence of that an apparently increasing tube height in constant-force mode is observed for semiconducting nanotubes. In contrast to that, metallic CNTs are unaffected by a tip voltage (see Fig. 4). The dependence of the tube height and the tip voltage is mainly influenced by the tube diameter, the chirality and especially the local polarizability of the substrate.

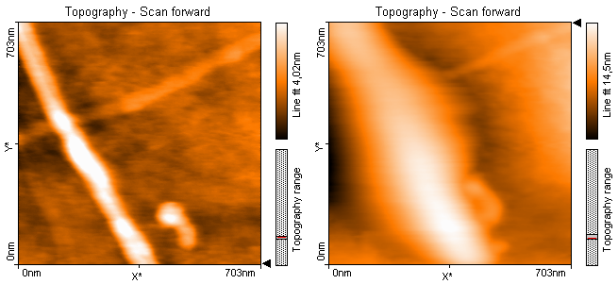

Fig. 4: Non-contact AFM (constant-force-mode) image of two CNT with 0V (left) and +6V (left) tip voltage, [1]

In contact- mode it is possible to investigate the current-voltage characteristic between the tip, the tube and another metallic contact. It is a good method to observe differences in the local conductivity with a spatial resolution of 10nm. First successful experiments for current detection by attached tip were made but further investigations especially on the CNT-tip contact are necessary.
The electric characterisation and the distinction between metallic and semiconducting tubes are interesting in combination with confocal Raman spectroscopy* for chirality assignment. This is possible because of chirality specific phonon features likes the D-Band. While theoretic models [4] predict that the D-band (a double-resonant process) is a typical mode for metallic tubes, we can show that also semiconducting CNTs have a D-Band.

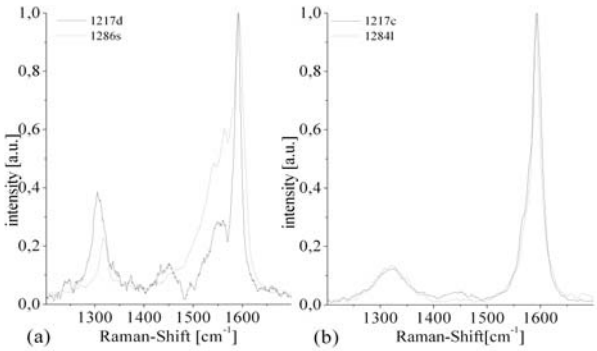

Fig. 5: Raman-Spectra of individual (a) metallic and (b) semiconducting CNTs, D-Band at 1300cm^{-1} and G-Band at 1550-1600cm^{-1}

But a fundamental difference in the D-Band width is observed for both kinds of tubes, as shown in Fig. 5. While metallic tubes show a small lorentzian D-Band (FWHM<50cm^{-1}), which is typical for a double-resonant process, semiconducting tubes have a D-Band with a larger width (70-120cm^{-1}), which indicates a principle difference in the excitation process. Non-resonant defect scattering could be a reason and is still under investigation.

References:

[1] H. Kleemann, Diploma Thesis, 2008
[2] T. DeBorde, J. C. Joiner, M. R. Leyden, E.D. Minot, Nanoletters 8 12 (2008)
[3] Wei Lu, Dan Wang, Liwei Chen, Nanoletters 7 2729-2733 (2007)
[4] J. Maultzsch, S. Reich, and C. Thomsen, Physical Review B, Volume 64 121407 (2001)

* We thank Harald Mutschke at the Astrophysics Institute for the possibility to accomplish Raman measurements.

Aligned growth of Carbon Nanotubes

F. Szillat, B. Schröter

The discovery of Carbon nanotubes in 1991 by Iijima [1] started a research that even to this day opened a wide ranged field of scientific interest. The remarkable mechanical, electronic and optical properties of single walled carbon nanotubes (SWCNT) implicate interesting applications, such as sensors or electronic devices. For the wide application of CNTs it is essential to grow them at preset positions and directions.

To achieve the aligned growth by using chemical vapor deposition (CVD) we employed pre-treated single crystalline sapphire substrates with pre-structured metal catalyst. During pretreatment of sapphire substrates they were annealed on air and subsequently characterized regarding surface quality, crystal and surface-step orientation.

The crystal orientation has been characterized by electron channeling pattern (ECP) as illustrated in figure 1 and correlated to X-ray diffraction (XRD) analysis. If this correlation is known for special crystal face, ECP is a fast and easy way to analyze surface quality and crystal orientation. These ECP measurements were done by using a scanning electron microscope (SEM). The ECP has been produced by backscattered electrons and their signal intensity change is generated via variation of angle between incident beam and the crystal lattice during scanning process.

Atomic force microscopy has been used to characterize the quality of the atomically flat terraces and the step direction on annealed sapphire.

After substrate pretreatment the deposition of catalyst has been carried out in our ultra-high vacuum multi-chamber arrangement (specified in [2]). Shadow masks allowed a structuring of the catalyst during the deposition. We used cobalt and iron as catalyst material on sapphire. The re-organization of the catalyst from thin film to particles happens during the initial stage of the CVD process [3].

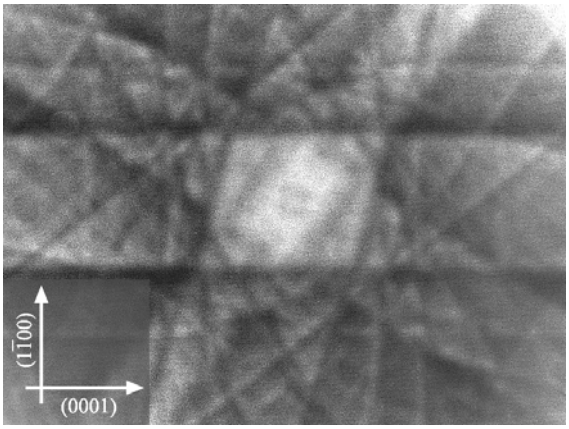

Figure 1:
ECP on a-plane sapphire after annealing on air: Characteristic for the Kikuchi pattern of an A-face surface is the main band parallel to the (0001) direction. The additional information about the y-axis is received by the band from top left to bottom right corner.

The process we run with sapphire substrates is close to that with silicon dioxide, which is described in [4]. The main difference is a lower process temperature, with 850°C for methane as carbon feedstock and is mainly caused by temperature dependent catalyst mobility. Furthermore, we added an ethanol source which even at lower temperatures (800°C) shows acceptable results. The alignment during growth process is a consequence of the interaction between SWCNT and the single-crystalline substrate surface. On pretreated A- and R-face of sapphire, (11$\bar{2}$0) or (1$\bar{1}$02), respectively, the arrangement of aluminum and oxygen atoms creates an electrostatic surface potential with a “line-grid” periodicity. The calculated surface potential of the a-plane shows these preferred growth directions (Fig 2.). In the following we confine our report to the experiments with A-face sapphire. To reach a maximum yield of aligned carbon nanotubes the catalyst is pre-structured as a cross or line grid.

After the CVD growth process we have proven the alignment of the CNTs by SEM analysis. However, the resolution is not as

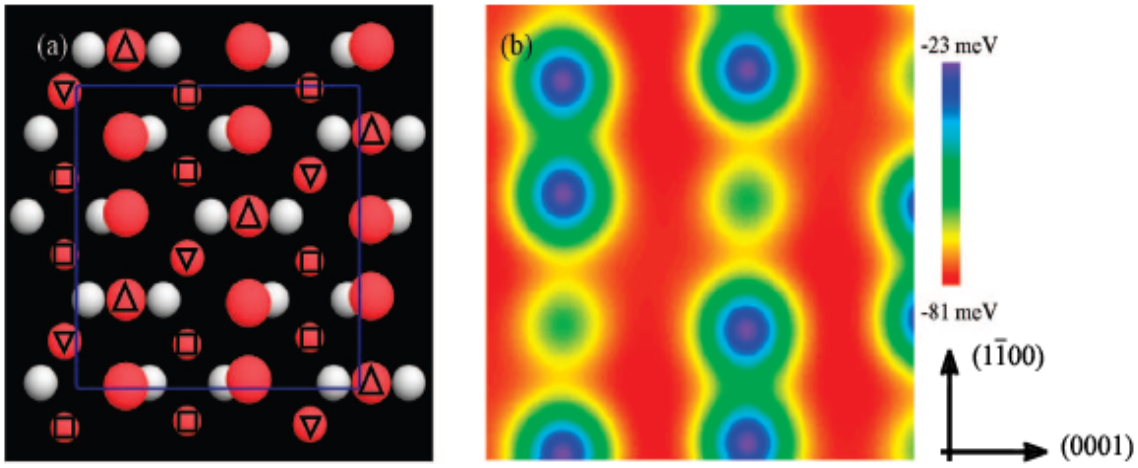

Figure 2: Crystal structure and calculated surface potential of an A-face sapphire [5];
(a) grey balls represent aluminum, red balls oxygen (without symbol and Δ above aluminum; □ and ∇ under aluminum) **(b)** surface potential calculated from the blue square in (a)

good as to determine the CNT diameter by these measurements hence we use Raman spectroscopy[1] to identify our tubes as SWCNTs.

The number density of CNTs on these substrates depends on the process parameters and has shown a maximum of 20 per (100x100) µm^2. Therefore, it is possible to grow separate SWCNTs that are not interacting with other tubes. The main parameters to control the density are the process temperature, the catalyst and hydrogen/precursor gas amount. The length of the nanotubes grown varies between 5 and 50µm. The three expected growth directions are shown in figure 3b: (1$\bar{1}$00), (2$\bar{2}$01) and (0001) which is towards surface steps on our substrates (0001).

The CNT growth behavior is rather different on sapphire in comparison to a growth on silicon dioxide [4]. Using a prestructured catalyst substrate as described above, an optimum substrate arrangement and growth temperature during CVD we reach an enhancement of the alignment. Furthermore, the (1$\bar{1}$00) direction is dominant in CNT alignment and it is possible to suppress other growth directions.

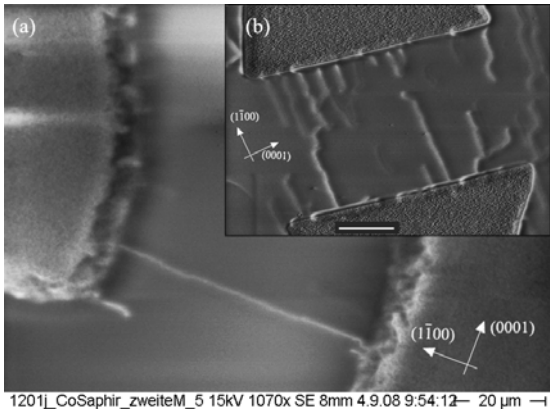

Figure 3:
SEM image of aligned CNTs on sapphire A-face:
(a) catalytic CVD with ethanol precursor and cobalt catalyst cross grid; on the catalyst pads (seen on left and right side of fig. 3) we detect high-density grown SWCNTs by Raman spectroscopy
(b) CVD with methane precursor and iron catalyst cross grid (white bar: 20µm)

[1] We thank Harald Mutschke and the Astrophysics Institute for the possibility to accomplish Raman measurements.

References:

[1] Iijima et al., Nature 354 (1991) 56.
[2] M. Blech, Annual Report IFK 2007.
[3] M. Blech, Diploma Thesis "*Kontrolliertes Wachstum und Analyse metallischer Nanopartikel ls Katalysatoren für Kohlenstoffnanoröhren"* (2008), Jena.
[4] M. Steglich, Annual Report IFK 2007.
[5] X. Liu, et al., J. Phys. Chem. C 112 (2008) 41.

The application of carbon nanotubes in chemical sensors

P. Zeigermann, B. Schröter

Carbon nanotubes (CNTs) are one-dimensional carbon allotropes with very promising physical properties in regard of their use in sensor configurations.
Some of these outstanding properties include their high electrical and thermal conductivity and their high mechanical and chemical stability [1]. The electrical conductivity of semiconducting CNTs is easily modified by applying a gate potential or by charge transfer to the CNT from adsorbed molecules. The latter can utilized in CNTs sensor devices.
We used chemical vapour deposition (CVD) to grow single-walled CNT mats on silicon dioxide substrates coated by a thin catalyst layer [2]. Electrical contact patterns were structured using a standard photolithographic process described elsewhere [3].

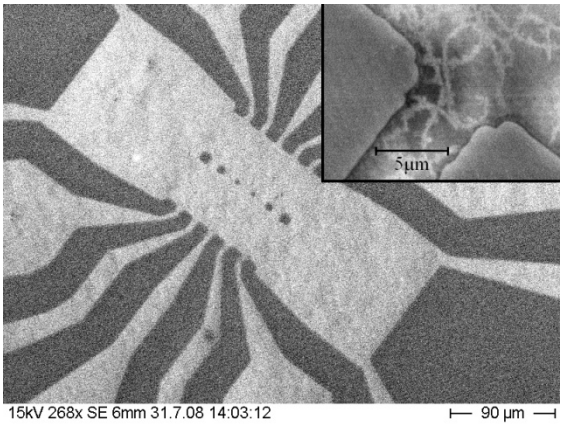

Fig. 1: Contact structure (dark) on CNTs

We have tested several metals (Au, Co, Ni, Pd) in regard of their contact resistance by comparing the 2-point resistance on similar CNT mats. The best metal-CNT contacts were generally achieved with Palladium despite of its lower specific conductivity (Fig. 2).
The conductivity of the CNT mats showed no gate-dependence, indicating a metallic behavior.

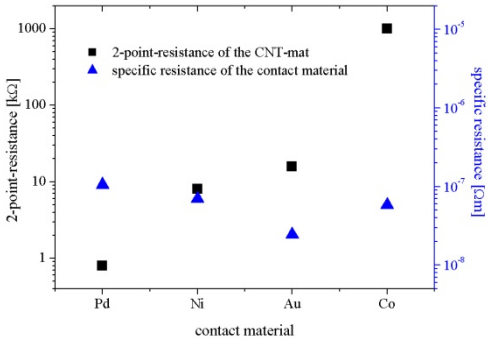

Fig. 2: two-point resistance of a CNT mat contacted with different materials

The sensor properties were determined by measuring the conductance G of the CNT devices in well-defined test environments, which were prepared in a special vacuum chamber. The effect of several gases and vapours can be studied down to the mbar level in vacuum or in carrier gases.
Among other gases, we studied the conductance change of the CNT mats under the influence of different partial pressures of ethanol vapour, hydrogen and air. The conductance of the CNT device drops when ethanol vapour is let into the previously evacuated chamber. Thus, the conductivity of the originally p-type CNT is reduced by the electron charge transfer from the adsorbed ethanol to the CNT. The conductance change of the CNT device after adding ethanol vapour to the chamber is proportional to the partial pressure of added ethanol (Fig. 3). The regeneration of the CNT sensor could be done by moderately heating the device (up to 150°C) or by simply evacuating the chamber for some hours.
If we used no inert carrier gas for the ethanol vapour, the conductance-time curves were best described by two exponential decays with a fast and a slow time constant. We tentatively attribute this to a fast adsorption of the ethanol at the surface and a slow diffusion into CNT-bundles or the slow down of the diffusion due to impurities. No saturation of the

conductance change was observed within several hours, thus the response (rel. conductance change $\Delta G/G_0$) of the CNT device was determined at a fixed time after adding ethanol to the vacuum chamber.

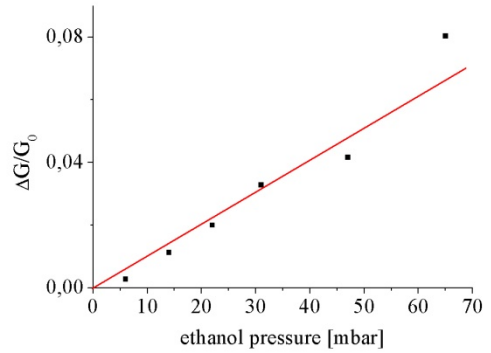

Fig. 3: Response ($\Delta G/G_0$) of CNT device after adding ethanol

However, when Argon was used as carrier for the ethanol a saturation of the conductance-change was observed after some minutes. This effect of the use of carrier gas is still unclear and needs further investigations.

As sensors are commonly to be used in atmospheric environments, we measured the effect of air on the conductance of the CNTs. While the main components of dry air (nitrogen, oxygen, carbondioxide, argon) show almost no measurable effect on the conductance of the CNT device, we found it to be sensitive to water vapour (Fig. 4). Hence the humidity is a crucial factor when measuring electric properties of CNTs in air. CNT devices could also be used for humidity detection.

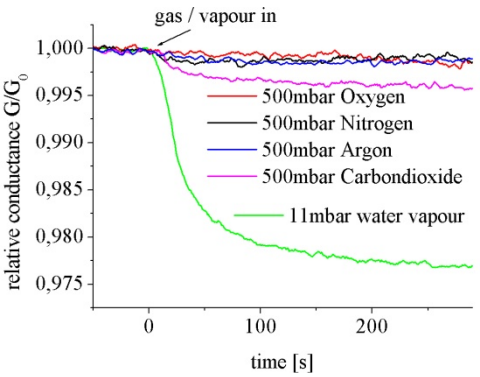

Fig. 4: Relative conductance of a CNT device after adding several air components to the vacuum chamber

The use of palladium contacts allows the detection of hydrogen with our CNT device. Figure 5 shows the relative conductance of a gold contacted and a palladium contacted CNT mat after hydrogen is let into the vacuum chamber. While there is no measurable effect with the gold contacted device, palladium contacts catalyze the dissociation of the molecular hydrogen. The atomic hydrogen induces an electric field at the CNT-palladium interface and therefore increases the contact barrier between palladium and CNT. Thus the conductance of the CNT device drops. However, no regeneration could be done by evacuating the chamber and annealing the sensor up to 150°C.

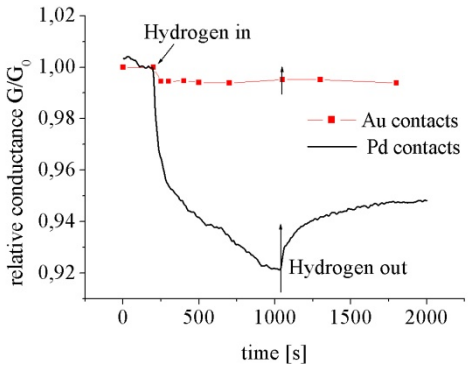

Fig. 5: Relative conductance of a Au contacted and a Pd contacted CNT-mat while adding hydrogen to the chamber

References:

[1] Mildred S. Dresselhaus, Gene Dresselhaus, and Phaedon Avouris: *Carbon Nanotubes - Synthesis, Structure, Properties and Applications.* Springer Berlin, 2001.
[2] Matthias Steglich: Diploma thesis, FSU Jena, 2007.
[3] Philipp Zeigermann: Diploma thesis, FSU Jena, 2008.

We highly appreciate the technical support by Frank Perner from the Institute of Optics and Quantum Electronics and the Dept. of Low Temperature Physics.

Semitransparent CdTe solar cells

C. Kraft, M. Hädrich, C. Löffler, U. Reislöhner, H. Metzner, W. Witthuhn

CdTe is a promising solar cell material with a high potential for further improvements. Laboratory cells reach more than 16% conversion efficiency. On an industrial scale CdTe based modules yield more than 10% efficiency. However those modules have absorber thicknesses of typically 5-10µm, while 2µm CdTe thickness is sufficient for 99% light absorption [1]. Thick absorber layers are necessary to avoid the formation of pinholes while thinner layers would result in less material consumption, lower production cost and even improved solar cells [2]. Further reduction of the absorber layer thickness to less than 1.5µm results in semitransparent solar cells, which are transparent for red and infrared light and hence could be used in tandem cell concepts.

A typical CdTe solar cell consists of a transparent conducting oxide (TCO) that is employed as front contact, a CdS buffer layer as the n-doped heteropartner to the p-doped CdTe absorber layer. A low ohmic back contact completes the solar cell of which an SEM cross-section micrograph is shown in Figure1.

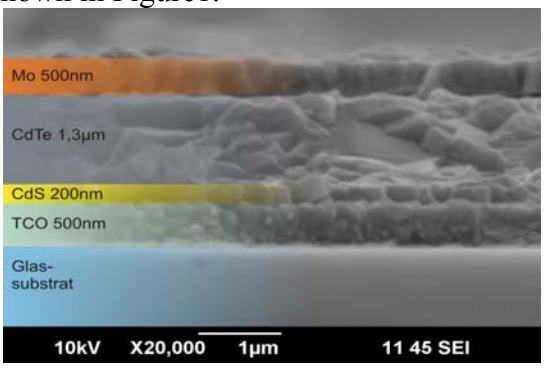

Figure 1 Cross section SEM micrograph.

The formation of the back contact is crucial for the solar cell performance. Usually a chemical etch (NP-etch) is applied to obtain a tellurium rich intermediate layer for a better back contact formation. When thin absorbers are applied, chemical etching is no longer suitable, since it leads to pinholes due to preferred etching at the grain boundaries. Instead of etching, we employed a back contact that consists of a very thin primary copper-gold contact (3nm Cu, 20nm Au) and a secondary back contact (about 500nm) consisting of molybdenum [3]. Another alternative for back contact formation is a plasma etching procedure, in which a tellurium rich surface layer is formed by selective removal of Cd atoms by an argon ion plasma.

The solar cells were produced in our own baseline. A detailed description of the cell preparation methods can be found in [4].

In this work three kinds of back contact formation and their influence on thin absorbers up to semitransparent layers were evaluated: NP-etching, plasma etching and the Cu-Au back contact.

Figure 2 shows SEM images of CdTe film surfaces with some microns thickness after different back contact methods were applied.

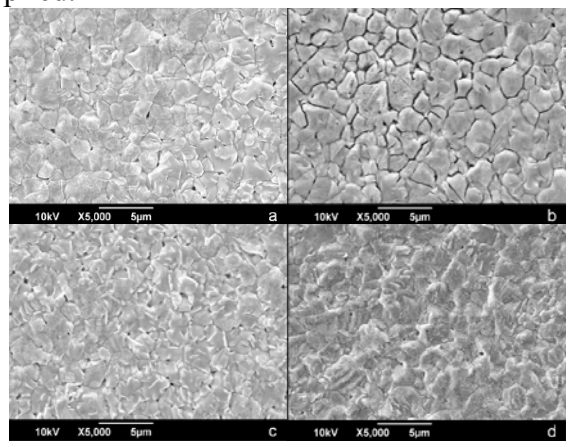

Figure 2 CdTe surface after application of different back contact treatments: a) no back contact, b) NP-etching, c) plasma-etching, d) Cu-Au evaporation.

Especially in case of the NP-etching significant cracks appear as a result of the NP-treatment. In case of the Cu-Au bilayer a homogeneous and compact surface is found. The surface structure after the

plasma etching is similar to the morphology without any treatment and solar cells that were produced with a plasma etched back contact showed considerable results (see Table 1).

V_{OC} [mV]	j_{SC} [mA/cm²]	FF	η [%]
701	23.1	0.44	7.1

Table 1 Characteristics of a solar cell with plasma etched back contact ($d_{CdTe} \approx 10\mu m$).

However, the surface became contaminated during the plasma etching process. The impurities on the surfaces were detected by EDX measurements (Table 2). The untreated cell has as much Te as Cd at its surface, while the NP-etched one has an excess of Te. The Na and Mo impurities on the plasma etched cell are the results of a contaminated reaction chamber.

back contact	relative surface composition					
	Cd	Te	Na	Mo	Cu	Au
(a) none	1.0	1.0				
(b) NP-etched	1.0	1.5				
(c) plasma etched	1.0	1.0	0.2(1)	0.1		
(d) Cu-Au	1.0	1.0			0.2(1)	0.2(1)

Table 2 EDX analysis of CdTe surfaces after application of different back contact treatments.

On the one hand we showed for NP-etched solar cells, that the efficiency decreases with decreasing CdTe absorber layer thickness (10µm down to 3.5µm) due to pinholes. On the other hand the efficiency of solar cells with a primary Cu-Au back contact was increased with decreasing CdTe thickness [2]. This is because thinner films allow more carriers to pass the material within their lifetime without recombination. Thus, the Cu-Au back contact remains as the most promising approach for solar cells with less than 2µm absorber thickness. By further improvements of the morphology, the deposition parameters and the post-deposition treatment of the cell, the CdTe thickness was further reduced to about 1.3µm. Table 3 shows the properties of the solar cell that was produced with that thin CdTe layer. In Figure 3 the transparent cell is demonstrated in front of a light source. This image was taken before back contact formation.

V_{OC} [mV]	j_{SC} [mA/cm²]	R_S [Ωcm²]	R_P [Ωcm²]	FF	η [%]
588	18.0	12.2	280	0.49	5.2

Table 3 Characteristics of a solar cell with a 1.3µm thin CdTe absorber layer and Cu-Au back contact.

Figure 3 Semitransparent CdTe solar cells.

Our results show that a decrease of the CdTe absorber layer to less than 2µm is possible by using Cu-Au back contacts. Solar cells that were produced with semitransparent absorbers show acceptable solar cell characteristics and are hence interesting as a part of tandem or multi-junction solar cells.

[1] C.S. Ferekides, D. Marinskiy, C. Viswanathan,B. Tetali, V. Palekis, P. Selvaraj, D.L. Morel, Thin Solid Films 261-362 (2000), 520.

[2] M. Hädrich, C. Kraft, C. Löffler, H. Metzner, U. Reislöhner, W. Witthuhn, Thin Solid Films (2008), in press.

[3] A.D. Compaan, A. Gupta, S. Lee, S. Wang, J. Drayton, Solar Energy 77 (2004) 815.

[4] M. Hädrich, N. Lorenz, H. Metzner, U. Reislöhner, S. Mack, M. Gossla, W. Witthuhn, Thin Solid Films 515 (2007).

Morphology of $CuInS_2$ absorbers for thin film solar cells

J. Cieslak, C. Weiss, H. Metzner

The chalcopyrite semiconductor $CuInS_2$ (CIS) is a promising material to be used as an absorber in thin-film solar cells. The advantages of CIS include the direct fundamental band gap of 1.52 eV [1], which is close to the optimum band gap for single-junction solar cells [2], as well as the absence of any toxic elements. CIS solar cells reach efficiencies up to 11.4% [3]. We prepared polycrystalline CIS thin-film absorbers on soda lime glass by means of a two-stage process and examined the morphology of the absorbers. The preparation process consists of cleaning of the substrate, sputtering of the molybdenum back contact, deposition of the Cu-In precursor and sulfurization of the precursor. In order to provide good adherence to both the substrate and the absorber layer, a special three-layer molybdenum back contact was used [4]. For the precursor deposition, 11 alternating layers of copper and indium (99.99% purity) were sputtered. The composition was controlled by the sputtering times. For the sulfurization process, the precursor was placed together with the sulfur (99.9995% purity) in a petri dish with a quartz glass cover. This container was placed in a vacuum chamber and heated to 500°C with a defined heating rate. After 30 min the sample was cooled down with 10 K/min. In this paper, the precursor composition and the heating rate were varied. The morphology of the CIS absorbers were examined by means of Scanning electron microscopy (SEM) employing a JSM-6490 (JEOL).

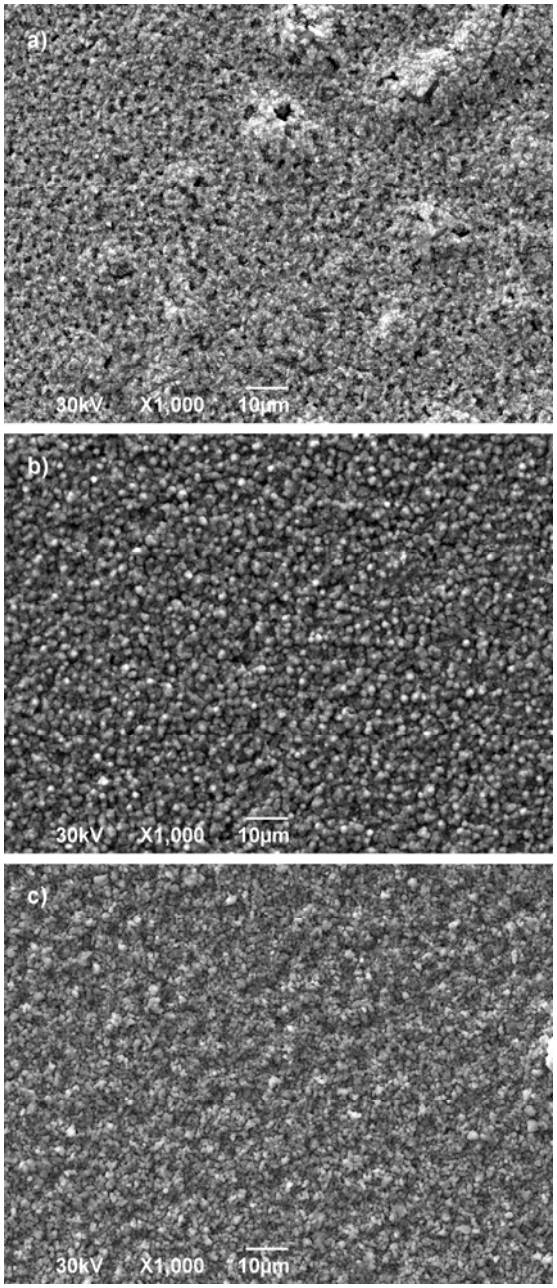

Fig. 1: SEM images of polycrystalline $CuInS_2$ films; precursor Cu/In ratio varies from a) 1.2 to b) 1.6 and c) 1.8.

I. Variation of the precursor composition:

Figure 1 shows SEM images of three CIS absorbers from precursors with varying composition. A strong dependence of the adherence of the CIS layer to the substrate on the Cu/In ratio of the precursor is observed. As the CIS films from the precursors with medium and high Cu/In ratio well adhere to the substrate (figs. 1b and 1c), the CIS film from the only slightly Cu-rich precursor exhibit only poor adherence (fig. 1a).

Thus, precursors with high copper excess are essential for adhesive and covering CIS absorber layers.

II. Variation of the heating rate

Figure 2 illustrates the impact of the heating rate during the sulfurization process on the growth of the CIS layer. To avoid peeling of the CIS layer, a precursor composition of $Cu_{1.8}In$ was chosen. Hence, the sulfurized samples are covered with a copper sulfide layer [5]. The film grown with the lowest heating rate of 20 K/min (fig. 2a) consists of large separated grains. The gaps between the grains would lead to shunts in the finished device and dramatically reduce its conversion efficiency. A heating rate of 40 K/min (fig. 2b) led to smaller grains with gaps between them, too. The highest heating rate of 80 K/min resulted in a compact CIS layer with densely packed grains, which is a good starting point for solar cells.

In conclusion, we prepared polycrystalline $CuInS_2$ absorber layers for thin-film solar cells and performed SEM measurements to investigate the morphology of the CIS samples. We found a strong dependence of the adherence between CIS layer and back contact on the precursor composition. Furthermore, a dependence of the grain size as well as roughness on the heating rate during the sulfurization was observed. High Cu-excess and high heating rate appears to be basic requirements for production of $CuInS_2$ solar cells.

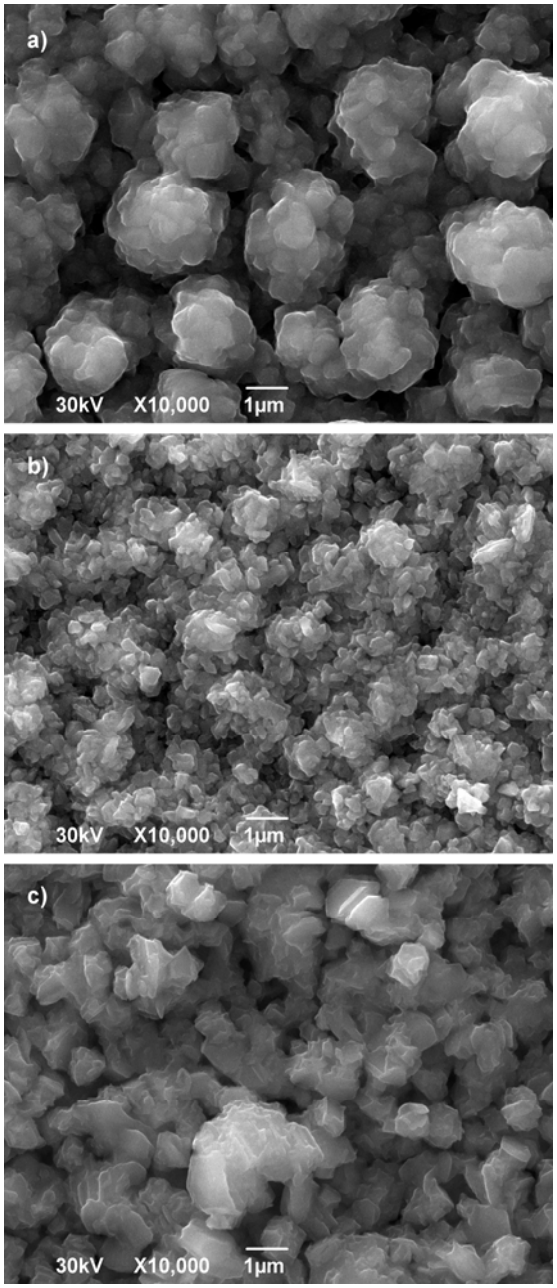

Fig. 2: SEM images of CIS films; heating rate during sulfurization varies from a) 20 K/min to b) 40 K/min and c) 80 K/min.

References

[1] R. Scheer, R. Klenk, J. Klaer, and I. Luck, Solar Energy **77** (2004), 777

[2] C.H. Henry, J. Appl. Phys. **51** (1980), 8

[3] R. Klenk, J. Klaer, R. Scheer, M.Ch. Lux-Steiner, I. Luck, N. Meyer, and U. Rühle, Thin Solid Films **480-481** (2005), 509

[4] M. Oertel, T. Hahn, H. Metzner, and W. Witthuhn, *$CuInSe_2$ solar cells by sequential absorber layer processing*, Phys. Status Solidi C, accepted for publication

[5] J. Alvarez-Garcia, A. Perez-Rodriguez, A. Romano-Rodriguez, L. Calvo-Barrio, B. Barcones, J.R. Morante, K. Siemer, I. Luck, and R. Klenk, Thin Solid Films **387** (2001), 219

Interface design in Cu(In,Ga)Se_2 solar cells by Cd-implantation

J. Haarstrich, M. Oertel, C. Wolf, T. Rissom*, H. Metzner

** HZB für Materialien und Energie Berlin, Glienickerstr. 100, 14109 Berlin*

Motivation

The chalcopyrite semiconductor Cu(In,Ga)Se_2 is successfully used as an absorber material in thin film solar cells both in laboratory scale and in commercial modules. In the standard configuration, a CBD-CdS buffer and a sputtered ZnO:i/ZnO:Al window layer are used for the formation of the p-n-junction. Much effort has been made to find an alternative for the CBD-CdS buffer layer leading to new materials such as zinc sulfide and indium sulfide as well as to other deposition techniques (sputtering, ILGAR) [1,2] which are on the way to reach equal efficiencies in laboratory as well as commercial production.

But CBD-CdS is still the most reliable choice for a robust interface design in Cu(In,Ga)Se_2 solar cells although its beneficial functionality is not fully understood yet. It has been shown that Cd ions remain in the Cu(In,Ga)Se_2 surface when the CBD-CdS is etched off with diluted HCl after deposition [3]. This leads to the idea that Cd-ions in the Cu(In,Ga)Se_2 surface might be responsible for some of the beneficial properties of the CBD-CdS buffer layer. It is known that in slightly Cu-poor Cu(In,Ga)Se_2-films a highly Cu-poor surface of unknown thickness develops which itself influences the junction formation. The low Cu concentration suggests that the Cd atoms could be a donor on a formerly vacant Cu-site (Cd_{Cu}). This in turn would cause a slight move of the p-n-junction position from the CdS-Cu(In,Ga)Se_2 interface into the absorber material which is known as an inverted interface and should be beneficial for charge carrier separation [4].

In this contribution, low energy Cd-implantation into the Cu(In,Ga)Se_2 surface is described as a new approach to investigate the influence of Cd on the junction formation. This approach opens up the possibility to vary both the absolute Cd concentration as well as its depth distribution independently in the whole range of interest. First results will be presented.

Simulation

Simulations with the SRIM-code [5] have been performed concerning ion range, damage creation and surface sputtering. Figure 1 shows the implantation profiles which have been calculated for ion energies ranging from 1 to 30 keV. This way it can be shown that energies ranging from 100 eV to 100 keV are necessary to cover the depth interval from 1 nm to 30 nm (Fig. 2, right scale). Homogeneous implantation profiles are accessible by means of implantations at different ion energies.

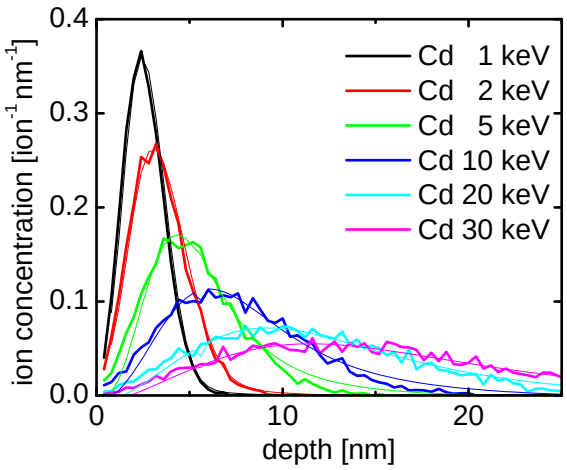

Figure 1: Near-surface implantation profiles of Cd in Cu(In,Ga)Se_2-films for various energies (SRIM)

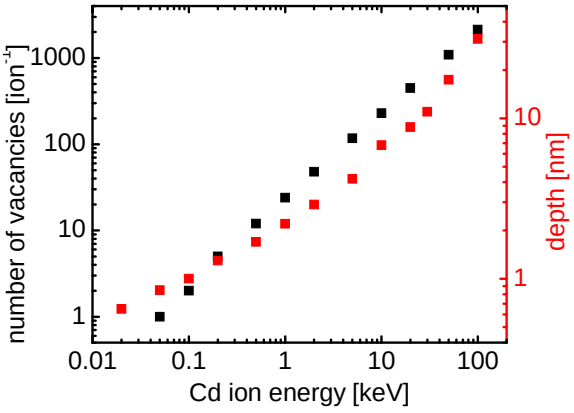

Figure 2: Number of vacancies (left scale) per ion and ion range (right scale) as a function of the ion energy (SRIM)

Furthermore, the formation of defects was estimated using SRIM calculations. As an example the number of vacancies produced per ion is plotted in Fig. 2 as a function of ion energy. It shows a linear correlation between ion energy and damage creation.
Assuming a sputtering yield of around 7 atoms per implanted ion (SRIM-calculation), a surface layer in the range of 1 nm has been estimated to be sputtered for an ion fluence of 10^{15} cm^{-2}. This must be considered in further analyses because the thickness of the highly Cu-poor surface layer might be influenced strongly.

Experiments

$Cu(In,Ga)Se_2$ absorber layers are deposited on Mo-coated soda lime glass by either a co-evaporation process at the HZB in Berlin or a two stage process of our lab. The 400kV-implanter ROMEO is used for the implantation of ^{114}Cd 20 keV with fluences ranging from 10^{13} cm^{-2} to 5 x 10^{15} cm^{-2}. The absorber surfaces are analyzed by scanning electron microscopy (SEM), photoluminescence (PL) and x-ray photoelectron spectroscopy (XPS). Additionally solar cells fabricated from implanted absorber layers are analyzed by j-V-characteristics and quantum efficiency measurements. Subsequent annealing in air at temperatures up to 300°C is applied to reduce the number of defects induced by implantation.

Results

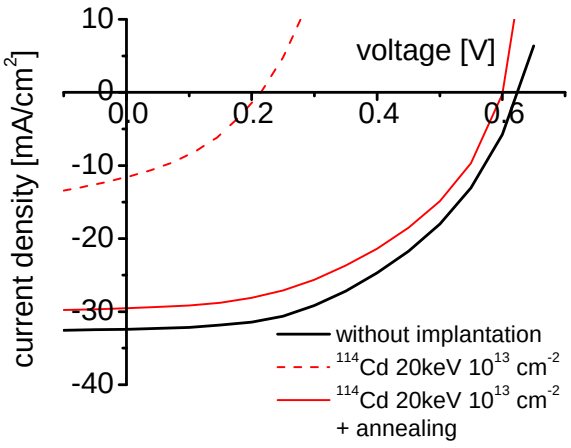

Figure 3: j-V-curve of unimplanted and implanted solar cells, showing that the recovery of solar cell properties is possible by annealing in air.

The very first results can be presented here.
The influence of implantation damage can be detected very clearly. Already for the smallest fluence applied the cell performance deteriorates completely (efficiencies below 1%, see Fig. 3).
Annealing in air up to 300°C can recover a reasonable cell performance for all implantation fluences (comparable with reference without implantation) as shown in Fig. 3.

Conclusion and plans

It has been shown by simulation and experiment that near-surface Cd implantation in $Cu(In,Ga)Se_2$ thin films can be done at ROMEO at the IFK in Jena. First analyses show a strong influence of implantation damage on the cell performance which can be recovered by annealing in air. Surface sputtering must be considered as a possible side effect to influence the solar cell properties.
Further experiments without a CdS buffer layer will have to show if it is possible to create an inverted interface by low energy Cd implantation.

Acknowledgements

We thank the Bundesministerium für Umwelt, Naturschutz und Reaktorsicherheit for financial support.

References

[1] N.A. Allsop et al., Thin Solid Films 515 (2007) 6068
[2] R. Saez-Araoz et al., Physica Status Solidi A 205 (2008) 2330
[3] D. Liao and A. Rockett, Journal of Applied Physics 93 (2003) 9380
[4] R. Klenk, Thin Solid Films 387 (2001) 135
[5] J.F. Ziegler, J.P. Biersack and U. Littmark, Pergamon, New York (2003)

Structural metastability and photoluminescence of $CuInS_2$

J. Eberhardt, J. Cieslak, H. Metzner, Th. Hahn, R. Goldhahn[1], F. Hudert[1], J. Kräußlich[2], U. Kaiser, A. Chuvilin, U. Reislöhner, and W. Witthuhn

[2] *Institut für Physik, Technische Universität Ilmenau, PF 100565, 98684 Ilmenau, Germany*
[3] *Institut für Optik und Quantenelektronik, FSU Jena, Max-Wien-Platz 1, 07743 Jena, Germany*

$CuInS_2$ (CIS) is a ternary chalcopyrite semiconductor with a direct fundamental band gap of 1.56 eV at 4.2 K [1]. Hence, CIS is employed as an absorber material in thin-film solar cells. Fig. 1 shows the crystal structure of the ground-state of CIS,

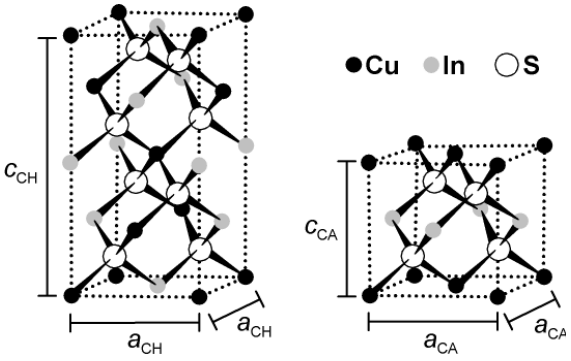

Fig. 1: Sketch of the relevant tetragonal lattice structures of $CuInS_2$: ground-state chalcopyrite (CH) structure (left) and metastable CuAu-type (CA) structure (right).

i.e. the tetragonal chalcopyrite structure (CH). CIS may also assume a metastable tetragonal structure in which the metal atoms show a CuAu-ordering (CA), also shown in Fig. 1. The possibility to grow lattice matched $Cu(In,Ga)S_2$ thin films epitaxially on Si substrates [2] could lead to high-efficient CIS devices. However, the efficiencies for epitaxial CIS absorbers are hitherto limited to 3.2% [3], while polycrystalline CIS solar cells reached 11.4% [4]. When these data are combined, it is found that the occurrence of the metastable CA ordering in CIS layers is accompanied by the absence of excitonic transitions and the appearance of a high density of electrically active intrinsic defects.

Both, epitaxial and polycrystalline CIS layers were deposited in the same molecular beam epitaxy (MBE) vacuum system as described elsewhere [5, 6]. X-ray diffraction (XRD) measurements were performed in order to study the crystal structure. The epitaxial samples were measured at the Rossendorfer beamline ROBL of the European Synchrotron Radiation Facility (ESRF) in Grenoble (France) [7]. In Fig. 2 typical low-temperature PL spectra of epitaxial and polycrystalline CIS layers are depicted. Both types of materials show strongly different recombination mechanisms. Epitaxial films in the as-grown state

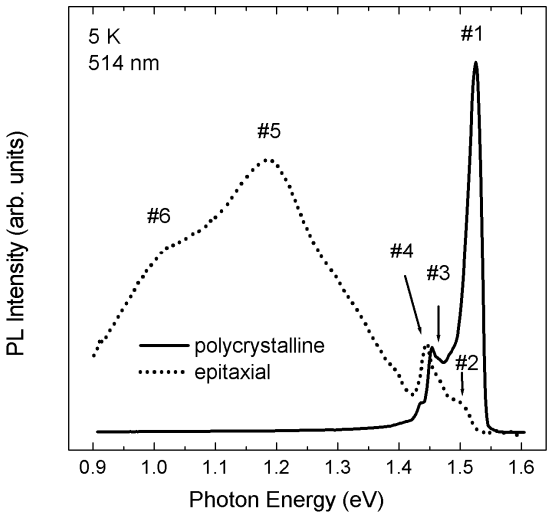

Fig. 2: Comparison of typical PL spectra of epitaxial and polycrystalline CIS layers on Si substrates. The PL lines #1 to #6 have already been identified in our previous work [8,9].

show defect related luminescence only [8]. This contrasts sharply with the PL spectra of polycrystalline CIS samples, where an excitonic line at 1.53 eV (#1) dominates the luminescence [9]. Also, the broad PL

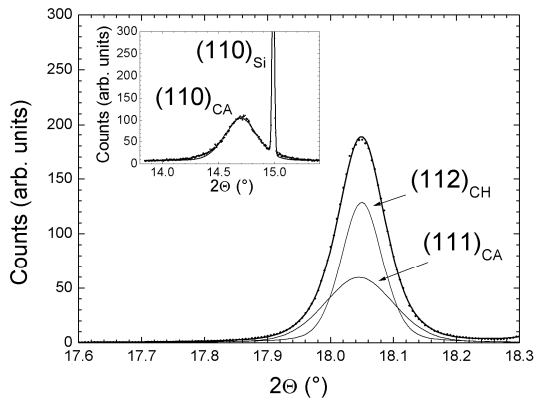

Fig. 3: X-ray-diffraction pattern of an epitaxial CIS film on Si(111). The film shows two reflections, which correspond to the chalcopyrite phase, i.e. $(112)_{CH}$, and the CuAu-phase, i.e. $(111)_{CA}$. The volume fractions are (79±6) % for the CH-phase and (21±6) % for the CA-phase. The inset shows the $(110)_{CA}$ reflection together with the forbidden $(110)_{Si}$ reflection which appears due to multiple scattering processes.

lines around 1.2 or 1.3 eV which are typical for polycrystalline CIS solar-cell material [10], were not observed. The outlined PL results reveal the optoelectronic quality of polycrystalline CIS to be superior to that of epitaxially grown CIS. This is a remarkable difference particularly with regard to the nearly identical growth conditions and suggests a structural origin rather than an impurity induced effect. Fig. 3 shows a X-ray-diffraction pattern of an epitaxial CIS film on Si(111). Here, both types of ordering, the CH and CA-type, can be detected [11]. The inset shows the (110) reflection, which is exclusively due to the CA structure. This clearly proves the existence of the latter, while the two reflections showing up between 18.0° and 18.1° are a clear manifestation of the coexistence of both ordering schemes. Selected-area-electron diffraction (SAED) confirms the coexistence of the ground-state CH and metastable CA ordering in epitaxial CIS. Typical $\omega/2\Theta$ scans of polycrystalline CIS samples (not shown here) show chalcopyrite reflections of CIS only and the observed chalcopyrite splitting indicates a high crystalline quality [12]. In previous investigations, using XRD [5] and TEM [6], we showed the epitaxial CIS layers to contain planar defects, but the films did not reveal any sign of polycrystallinity.

Our results show the coexistence of the CH and CA phases in epitaxial layers always to be accompanied by a high density of deep defects, which cause the defect-related transitions in the PL together with the absence of excitonic emissions. Grain boundaries as easy diffusion paths for excess Cu and S do not exist in epitaxial CIS and so the CA phase is kind of frozen in which leads to an inferior structural and optoelectronic quality when compared to the polycrystalline CIS films.

The authors thank the Stiftung Nagelschneider, the DFG, the TKM, the BMWi, and the ESRF (Grenoble) for their generous support.

References

[1] M.V. Yakushev et al. Appl. Phys. Lett. **88** (2006) 011922.
[2] H. Metzner et al. Appl. Phys. Lett. **83** (2003) 1563.
[3] Th. Hahn et al. J. Phys. Chem. Solids **66** (2005) 1899.
[4] K. Siemeret al. Sol. Energy Mater. Sol. Cells **57** (2001) 159.
[5] H. Metzner et al., Thin Solid Films **403-404** (2002) 13.
[6] Th. Hahn et al. Appl. Phys. Lett. **72** (1998) 2733.
[7] W. Matz et al. J. Synchrotron Radiat. **6** (1999) 1076.
[8] J. Eberhardt et al. Thin Solid Films **480-481** (2005) 415.
[9] J. Eberhardt et al. Thin Solid Films **515** (2007) 6147.
[10] E. Rudigier et al. Thin Solid Films **480-481** (2005) 327.
[11] J. Cieslak et al. Phys. Rev. B **75** (2007) 245306.
[12] J. Eberhardt et al. J. Appl. Phys. **102** (2007) 033503.

Formation of CdS_xTe_{1-x} at the pn-junction of CdS-CdTe solar cells

M. Hädrich, C. Kraft, H. Metzner, U. Reislöhner, C. Löffler, and W. Witthuhn

In CdTe solar cells, CdS is commonly used both as n-type heteropartner and as buffer layer on the front side. Intermixing of CdTe with CdS leading to CdS_xTe_{1-x} alloy formation is known to occur especially in the thermal activation treatment during solar cell processing [1]. In this work [2], the impact of intermixing on the optical and electronic properties of solar cells is elucidated with regard to the thickness of the CdTe film, the application of the CdS film and the activation treatment. To this end, the bandgap and chemical composition of the alloy were determined by optical and external quantum efficiency (EQE) measurements.

CdS_xTe_{1-x} alloys exhibit a parabolic dependence of the bandgap energy E_G on the composition parameter x [1]. A miscibility gap in the phase diagram restricts x to the interval between 0 and 0.06 on the tellurium rich side and between 0.97 to 1 on the sulphur rich side for temperatures of about 400°C, as applied in the activation treatment [1]. This corresponds to the shadowed area in Fig.1.

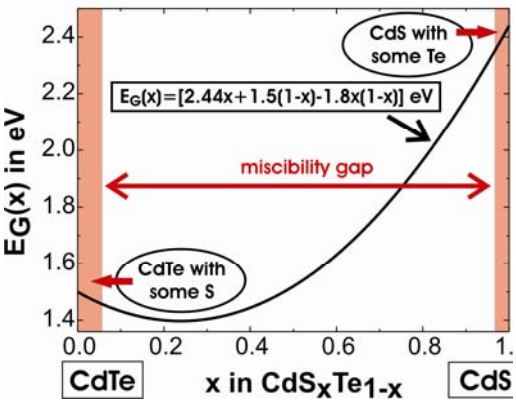

Figure 1 $E_G(x)$ curve of CdS_xTe_{1-x}. The phases occurring in the solar cells are restricted to the shadowed areas (see text).

Optical measurements of 3.7 µm CdTe films deposited with or without CdS film show the bandgap of pure CdTe (approx. 1.50 eV), independent of whether the samples were activated or not (Table 1).

Table 1 Optically measured E_G values of CdTe films deposited with or without CdS layer.

d_{CdTe}	CdS layer	Acti-vation	E_G CdTe [eV]	x in CdS_xTe_{1-x}
3.7µm	None	No	1.497(2)	0.00(1)
3.7µm	None	Yes	1.499(2)	0.00(1)
3.7µm	200nm	No	1.497(2)	0.00(1)
3.7µm	200nm	Yes	1.497(2)	0.00(1)
230nm	100nm	No	1.496(2)	0.00(1)
230nm	100nm	Yes	1.462(7)	0.05(1)

However, when thin CdTe films (230 nm) are deposited on CdS, a significant bandgap decrease is measured after the activation. According to the $E_G(x)$ diagram in Fig. 1, this corresponds to intermixing of CdTe with CdS up to the solubility limit of approx. 5 to 6% throughout the CdTe film, as illustrated in Fig. 2.

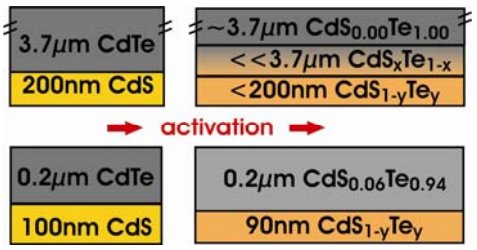

Figure 2 Intermixing model for the CdS-CdTe-interface. CdTe side: sulphur content 0<x<0.06 CdS side: tellurium content 0<y<0.02, y=1-x.

Moreover, a thickness loss of the CdS film of about 10 nm is determined by the optical measurements. The formation of an intermixed phase of some 100 nm thickness is also assumed for the 3.7 µm CdTe films. As the intermixed region is thin compared to the thickness of the CdTe

film, it is not detected. The results indicate that the intermixed phase gains importance in the case of thin CdTe films.

The EQE spectra of solar cells with 9.5 µm CdTe thickness and different CdS thicknesses or without CdS film (Fig. 3) show the CdS film to be crucial for the electronic properties of the solar cell.

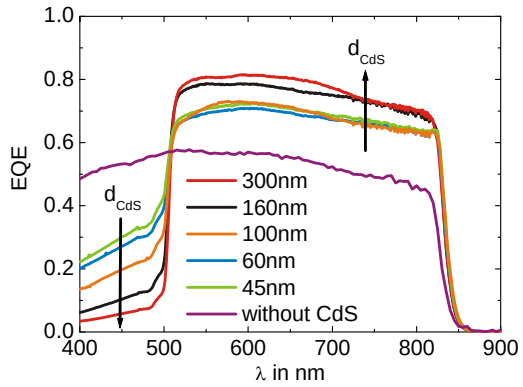

Figure 3 EQE of solar cells with different CdS thicknesses or without CdS film.

The EQE is systematically increasing between 550 and 800nm for increasing CdS thickness. The decrease below 500nm for increased CdS film thickness is due to exponential light absorption in CdS which is believed not to contribute to the photocurrent. The cell without CdS buffer layer shows consistent results yielding the lowest EQE in the long and the highest EQE in the short wavelength range. The former reflects the poor performance of a cell without CdS buffer layer while the latter is due to the missing light absorption in CdS.

Table 2 Bandgap (+/-2meV) and tellurium content y=1-x (+/-0.002) of CdS films with different thicknesses measured by EQE.

CdS nm	45	60	100	160	300
E_G /eV	2.411	2.413	2.418	2.430	2.431
y	0.011	0.010	0.008	0.004	0.003

The CdS bandgap was determined by EQE measurements (see Table 2). A significant bandgap decrease is visible for decreasing CdS thickness indicating that diffusion of Te into CdS is more pronounced for thin CdS films because of a higher relative Te fraction.

The J-V-characteristics and properties of solar cells with 45 or 300 nm and without CdS film are shown in Fig. 4 and Table 3.

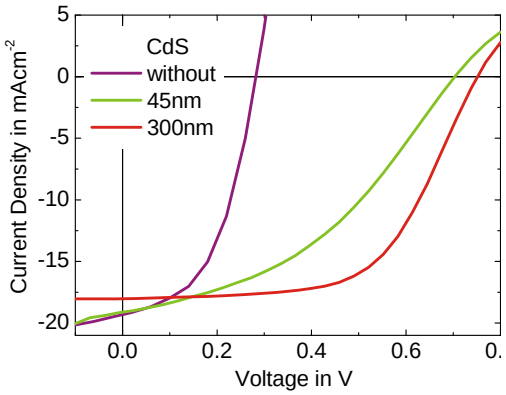

Figure 4 J-V characteristics of CdTe solar cells with 45 nm, 300 nm CdS and without CdS film.

Table 3 Properties of the solar cells in Fig. 4 with and without CdS film.

d_{CdS} [nm]	V_{oc} [mV]	R_{sh} [kΩcm²]	FF	η [%]
0	280	0.1	0.50	2.7
45	705	0.1	0.40	5.5
300	751	1.9	0.60	8.1

The solar cell properties improve for increasing CdS thickness. Applying a CdS buffer layer thereby seems mandatory to obtain high open-circuit voltages V_{oc} above 700 mV. The high shunt resistance R_{sh} of the cell with thick CdS demonstrates thick CdS films to avoid shunting.

References:

[1] B.E. McCandless and J.R. Sites, in: Handbook of Photovoltaic Science and Engineering, Eds. A. Luque and S. Hegedus, Wiley 2002.

[2] M. Hädrich, C. Kraft, H. Metzner, U. Reislöhner, C. Löffler, W. Witthuhn, phys. stat. sol. (a) (2009), in press.

CIGS solar cell process line completely scaled up to 10x10 cm^2 form factor

M. Oertel, J. Haarstrich, C. Wolf, T. Hahn and H. Metzner

In the annual report of the Institute of Solid State Physics (IFK) of 2007, we reported our first results of the preparation of $CuInSe_2$ solar cells by a sequential process [1]. The first step of the sequential or also called two-stage process is the sputtering of the molybdenum back contact and a variable number of copper and indium layers onto a substrate, normally cheap soda lime glass (SLG). In the second step, this precursor is reactively annealed in a selenium atmosphere where the gaseous selenium can be provided by different methods [2,3,4]. The limitation in our process was the small sample size of 2.5x0.7 cm^2 due to the small diameter of the tube furnace in which the selenization was accomplished. Thus edge effects often influenced the results of our experiments. Also, the process of fusing the samples in fused silica tubes was quite difficult and had some parameters which were only hard to control.

Within comCIGS-project [5], we are responsible for building up a process line with a sample size of 10x10 cm^2. Funded by this project, a Pfeiffer Classic 570 SP high vacuum (HV) sputter coating system (Fig. 1) was ordered in February 08 and delivered in October 08. The HV chamber has a base pressure of $< 5.0x10^{-7}$ mbar and is equipped with three 15 cm diameter AJA ST 60 sputter sources for sputtering molybdenum, copper or CuGa, and indium. Four 10x10 cm^2 soda lime glass (SLG) substrates can be coated with the back contact and the metallic precursor in one working step. The substrates are cleaned by means of plasma etching which is also done in the HV chamber. Additionally, the system serves to sputter font grids onto the top of a solar cell. Sputter pressures from $2.0x10^{-3}$ mbar up to $5.0x10^{-2}$ mbar are adjustable by controlling the argon flux and each of the two Maris GS30 dc power supply units has a nominal output power of 3 kW. Thus the new coating system gives us the possibility to vary the sputter parameters in a wide range for the molybdenum back contact as well as the $CuIn_xGa_{1-x}$ precursor ($0 \leq x \leq 1$) on a substrate area of 10x10 cm^2.

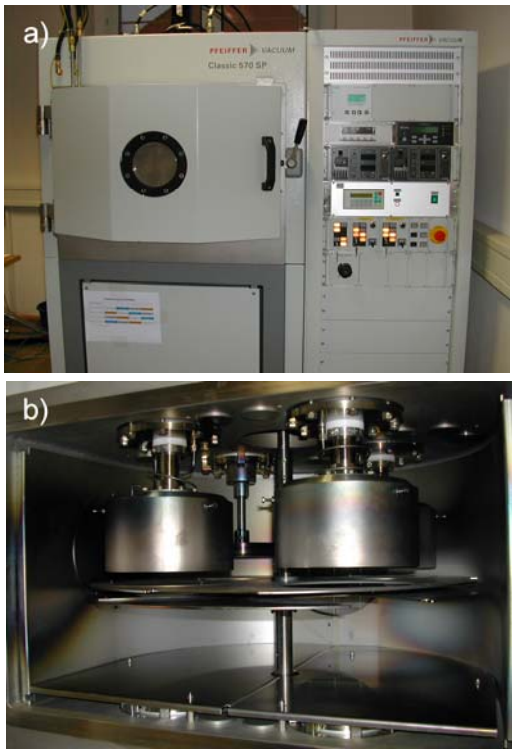

Figure 1: a) front of the Pfeiffer Classic SP 570
b) Inside of the sputter chamber

For the selenization of samples with the size of 10x10 cm^2 we received a Balzers ULS 400 HV-co-evaporation system (Fig. 2) as a permanent loan from the Institute of Physical Electronics (IPE) in Stuttgart. The high vacuum system with a base pressure $< 1.0x10^{-7}$ mbar is equipped with Createc effusion sources for evaporation of copper, indium and gallium, one IPE Knudsen-type source for evaporation of selenium and one EPI cracker source for evaporation of sulfur. The samples are heated by a boron ni-

tride heating element which is characterized by high temperature homogeneity over the whole area and heating rates up to 2.5 Ks^{-1}. The process control is carried out by a Balzers QMA 400 mass spectrometer. The sequential process with the 10x10 cm^2 sized samples can be carried out in two different ways in the ULS 400. The first is to deposit a selenium layer onto the precursor surface which is followed by the annealing step, the so called stacked elemental layer process (SEL) [4]. The second is to evaporate selenium directly during the annealing step without previous selenium deposition (in-beam). Furthermore, with the sulfur source we have the ability of sulfurization of the precursors or $CuIn_xGa_{1-x}Se_2$ absorber layers ($0 \leq x \leq 1$) to increase the absorber's band gap and thus the open-circuit voltage of the solar cells [6]. Beside the sequential process, in the ULS 400, the absorber layer could also be processed by co-evaporation.

Figure 2: Balzers ULS 400

So with this new equipment for sputtering back contacts, precursors and front grids and selenization, the Pfeiffer Classic 570 SP HV-coating system and the Balzers ULS 400 HV-co-evaporation system and the already existing equipment for chemical bath deposition (CBD) of CdS and rf-sputtering of the ZnO front contact in the 4Tec HV-rf-sputter chamber the whole process line for processing CIGS solar cells on a 10x10 cm^2 substrate is available.

Figure 3 shows U-j-curves of $CuInSe_2$ solar cells differently processed in this line. One was selenized with SEL process the other with the in-beam-process. For comparison, the curve of one of the best cells processed in the tube furnace with a sample size of only 2.5x0.7 cm^2 is shown. These first promising results indicate some potential for further improvements of the solar cell performance.

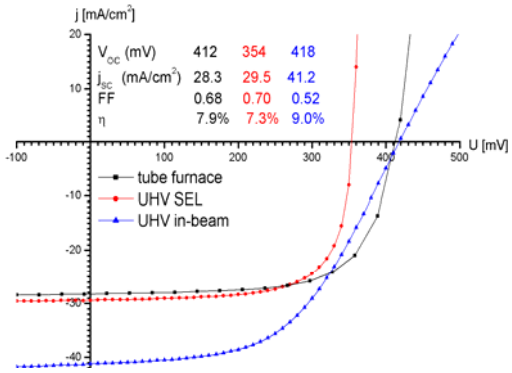

Figure 3: Solar cell performances of differently processed absorber layers

Acknowledgement

The authors specially thank the Bundesumweltministerium (BMU) for its financial support and the Institut für physikalische Elektronik (IPE) Stuttgart for the loan of the Balzers ULS 400.

[1] M. Oertel, Th. Hahn, H. Metzner, W. Witthuhn; Institue of solid state physics annual report 2007

[2] V Alberts; Semiconductor Science and Technology **19**, p. 65 (2004)

[3] T. Pisarkiewicz, H. Jankowski; Vacuum **70**, p. 435 (2003)

[4] V. Probst, W. Stetter, W. Riedl, H. Vogt, M. Wendl, H. Calwer, S. Zweigart, K.-D. Ufert, B. Freienstein, H. Cerva, F. H. Karg; Thin Solid Films **387**, p. 262 (2001)

[5] Bundesumweltministerium comCIGS projekt

[6] C. J. Sheppard, V. Alberts, W. J. Bekker; physica status solidi (a) **201**, p. 2234 (2004)

$Si_{1-x}Ge_x$ nanocrystals: Synthesis by laser-induced pyrolysis and photoluminescence properties

L. B. Ma, T. Schmidt, and F. Huisken

Silicon-based nanocrystals (NCs), also referred to as silicon quantum dots (QDs), are promising candidates for a variety of potential applications not only in optoelectronics and photonics, but also in the field of biology and medicine. It is the quantum confinement effect (QCE) which plays an essential role in the light emission of silicon-based NCs, allowing one to obtain flexible control over the efficiency of optical radiative transitions and their energy. Many techniques such as laser pyrolysis, magnetron sputtering, silicon ion implantation, PECVD *etc*. have been developed to synthesize Si NCs, among which laser pyrolysis is preponderant in producing free silicon-based NCs with controllable size. The photoluminescence (PL) of Si NCs located in the visible and near infrared spectral range (below 1.1 μm) has been demonstrated by many researchers in the past two decades. However, light emission at around 1.5 μm is required for currently used optical fiber communication systems where the fiber losses have their minimum. At the same time, germanium (Ge) with a bulk band gap of 0.66 eV (1.88 μm) at 300 K will enable light emission at longer wavelengths and thus comply with fiber optics demands. Furthermore, by introducing Ge into Si NCs with different atomic concentrations and by changing the NC sizes, their band gap can, in principle, be tailored so that the NCs emit at any desired wavelength between ~600 nm and 1.8 μm. Finally, as predicted by theory [1], a shorter PL lifetime can be expected from $Si_{1-x}Ge_x$ NCs. Therefore, the investigation of efficient synthesis of $Si_{1-x}Ge_x$ NCs and the study of their PL properties are of significant scientific importance.

Using a pulsed CO_2 laser (20 Hz repetition rate, 10.6 μm wavelength) to decompose a mixture of silane (SiH_4) and germane (GeH_4) in a flow reactor, $Si_{1-x}Ge_x$ NCs can be synthesized therein. By varying the process parameters, such as laser power, working pressure, and flow rates of the reactive gases, $Si_{1-x}Ge_x$ NCs with different fractional compositions of germanium and different particle sizes can be produced. The as-grown $Si_{1-x}Ge_x$ NCs can be deposited on substrates as thin films employing size-selected cluster beam deposition or, alternatively, they can be collected in a filter mounted into the exhaust line of the flow reactor.

The atomic ratios in as-prepared $Si_{1-x}Ge_x$ NCs were determined by means of Rutherford backscattering spectroscopy (RBS). High-resolution transmission electron microscopy (HRTEM) was applied to examine the microstructure of the $Si_{1-x}Ge_x$ NCs. The main focus, however, was directed to the PL wavelength and time dependence, enabling us to characterize the PL properties and to clarify its origin.

Single-crystalline $Si_{1-x}Ge_x$ particles with high quality were revealed by HRTEM examination. Figure 1 shows typical images of $Si_{1-x}Ge_x$ NCs under HRTEM. The particles were found to posses perfect spherical shape; therefore, they have minimum surface-to-volume ratio which means that the existence of non-radiative defect centers at the surface are maximally avoided. The higher-resolution image also displayed in the figure reveals the high-quality lattice structure of the $Si_{1-x}Ge_x$ NCs, indicating that the NC cores are essentially defect-free. Thus, regarding the PL properties, an optimistic perspective can be given.

The 4th harmonic of a Nd:YAG laser (266 nm or 4.66 eV) was used to explore the PL properties of the $Si_{1-x}Ge_x$ NCs. Figure 2 shows a set of PL spectra measured from the same $Si_{0.9}Ge_{0.1}$ NC sample as a function of time, starting one day after synthesis. A continuous blueshift of the PL curves was observed as time proceeded, due to the natural oxidation of the $Si_{1-x}Ge_x$ NCs in ambient air. Generally, the fresh particles can hard-

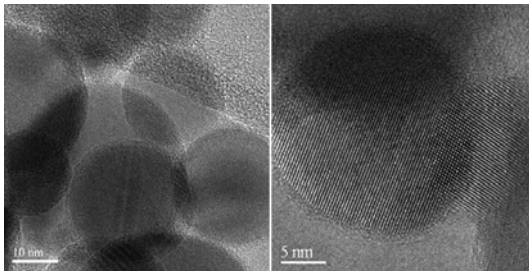

Fig. 1: Single-crystalline $Si_{1-x}Ge_x$ NCs of high quality with perfect spherical shape as revealed by HRTEM measurements.

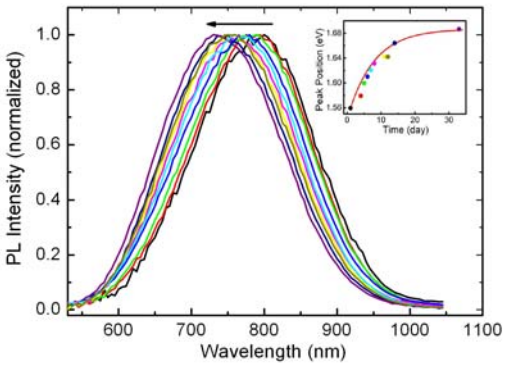

Fig. 2: The evolution of PL spectra from as-deposited $Si_{0.9}Ge_{0.1}$ NCs was monitored for more than 30 days with continuous blueshift due to the aging effect. The inset shows the peak positions as a function of time together with a fit (red curve).

ly emit photons because non-radiative surface defect centers will annihilate the light emission. Natural oxidation will provide a passivation layer enwrapping the $Si_{1-x}Ge_x$ NCs and eliminating non-radiative defect centers from the surface. As a result of the oxidation, the size of the inner crystalline core is continually reduced as time goes by. After approximately 30 days, the blueshift of the peak position seems to stop as shown in the inset of the figure. A similar behavior is also observed for the full width at half maximum of the PL spectra which increases from 350 to 450 meV during the first ten days. These results, which are in perfect agreement with earlier studies on pure Si NCs [2], suggest that radiative recombination of quantum-confined excitons are responsible for the PL mechanism. Furthermore, besides the strong PL in the red-NIR spectral range, we also observed weak PL around 400-500 nm, which, however, should be assigned to defect states in the passivation layer.

Time-resolved PL analyses were parallelly performed on the luminescent $Si_{0.9}Ge_{0.1}$ NC sample. During the first ten days, the lifetime continuously increased, eventually reaching stable conditions due to the successful passivation of initial defects. Figure 3a shows the decay curves measured at different wavelengths after thirty days when the decay curves stopped changing. As observed for porous silicon and pure silicon NCs [3], the nanoparticles emitting at longer wavelength (lower energy) reveal slower decay (see Fig. 3a). It was also found that, at any given wavelength, the decay in $Si_{1-x}Ge_x$ NCs was more rapid than in pure Si NCs produced under the

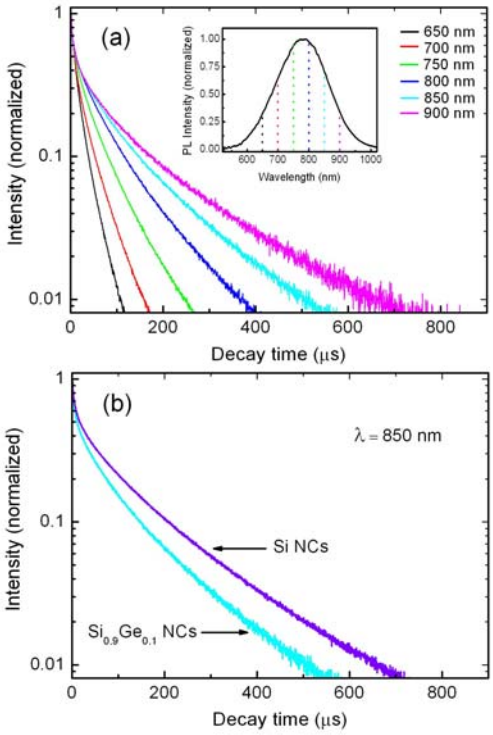

Fig. 3: (a) PL decay curves measured at various wavelengths for the $Si_{0.9}Ge_{0.1}$ NC sample. Higher emission energies are associated with shorter lifetimes. (b) Comparison between Si NCs (violet) and $Si_{0.9}Ge_{0.1}$ NCs (cyan) decays at 850 nm.

same conditions. This is demonstrated in Fig. 3b. It should be noted that the decay curves cannot be fitted by single exponential functions; instead one has to take stretched exponentials. This behavior is well-known for indirect semiconductor QDs.

The present work demonstrates that $Si_{1-x}Ge_x$ NCs are promising candidates for light-emitting nanostructures in photonic and optoelectronic applications. More detailed studies are in progress

Acknowledgments

This work was supported by a cooperation between the Max-Planck-Institut für Astronomie and the FSU Jena as well as by the Deutsche Forschungsgemeinschaft.

References

[1] H.-Ch. Weissker, J. Furthmüller, F. Bechstedt, Phys. Rev. B **69**, 115310 (2004).

[2] G. Ledoux, J. Gong, F. Huisken, Appl. Phys. Lett. **79**, 4028 (2001).

[3] F. Huisken, G. Ledoux, O. Guillois, C. Reynaud, Adv. Mater. **14**, 1861 (2002).

UV absorption spectroscopy of jet-cooled carbon clusters: The linear C_3 molecule

M. Arold, G. Rouillé, Th. Henning, and F. Huisken

A number of molecular species, such as polycyclic aromatic hydrocarbons (PAHs), are claimed to be present in interstellar clouds, and thus they will contribute to the interstellar absorption features in the visible and ultraviolet range. To prove this, laboratory UV/vis absorption spectra have to be measured for such species under astrophysically relevant conditions, *i.e.*, in a collision-free environment and at low temperature. We use cavity ring-down laser absorption spectroscopy (CRDS), a highly sensitive technique, to probe supersonic expansions of rare gases seeded with the species under study, for such expansions mimic the conditions found in the interstellar medium. The principal means of transferring solid samples to the gas phase is heating. Unfortunately, this method is too inefficient for very large PAHs and, in addition, it is not suitable for species which decompose at the elevated temperatures. To overcome this difficulty, laser vaporization (or laser ablation) of solid samples is being explored as a means to seed supersonic jet expansions with such molecules in a quantity suitable for absorption spectroscopy.

Last year, we reported on our first experiments regarding the possible combination of laser vaporization and CRDS [1]. For these experiments, we built a relatively simple laser vaporization source where the vaporization took place outside of the pulsed valve but very close to its nozzle exit. Compared to our heated source, this source led to higher rotational and vibrational temperatures. To obtain lower rotational and vibrational temperatures, the laser-vaporized molecules should be mixed with the carrier gas before it starts to expand, *i.e.*, inside the nozzle. During the last year, we have developed such source where the laser vaporization occurs inside the nozzle.

In this new source, the solid sample, in the form of a rod, is placed inside the jet source in close contact to its expansion channel, following a design by Neubauer *et al.* [2]. The setup used in the present study is sketched in Fig. 1. When the valve (General Valve Series 9) opens, the carrier gas (Ar) flows through the channel passing the surface of the sample rod. At the same time, the focused beam from a pulsed Nd:YAG laser (Continuum NY 61-20) is directed through the nozzle onto the surface of the rod. As a result, molecules are ejected and mixed with the carrier gas. At the exit of the nozzle, the mixture expands adiabatically into the vacuum and the molecules are cooled via collisions. At a variable distance x from the nozzle exit, the molecules are probed by CRDS. In this technique, the decay of the radiation from a pulsed tunable laser at the exit of a high-quality resonator is measured. The decay time can be directly converted to an absorption cross section. Even though the quality of the resonator provides a decay time of about 20 – 30 µs, it is sufficient to probe the sample molecules for only 4 – 5 µs. This can be easily achieved although the laser pulse has a duration of only 10 ns. To obtain stable vaporization conditions over a long time, the sample rod is translated and rotated.

To test the new source, we used a commercial graphite rod. Upon laser vaporization, among others, the carbon cluster C_3 is formed which is used as a test molecule. We measured absorption spectra in the wavelength range of 386 – 399 nm. In this range, we could observe many absorption bands related to C_3 which are already known from the literature. In Fig. 2, we compare our CRDS spectrum (red curve) with

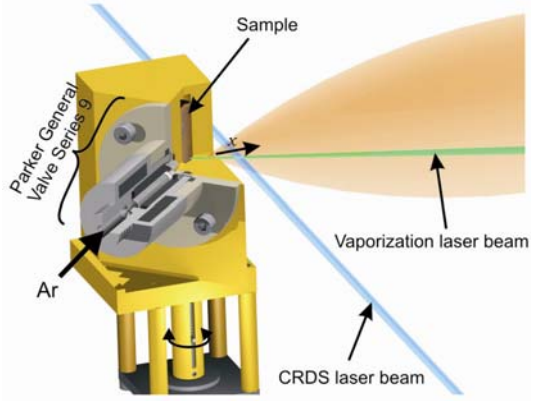

Fig. 1: Laser vaporization source with the sample (brown) inside the source body (yellow) attached to a electromagnetically driven pulsed valve (gray).

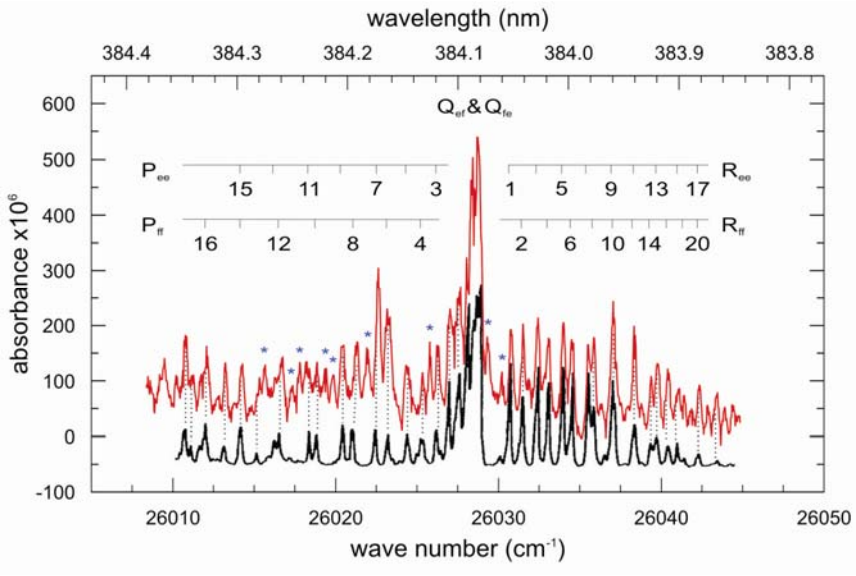

Fig. 2: Comparison of our CRDS spectrum of C_3 produced by laser vaporization of graphite at 532 nm (red curve) with a literature spectrum [3]. The lines marked with blue asterisks cannot be seen in the literature spectrum and are either due to other bands of C_3 or another carbon cluster. The assignments of the lines are taken from the literature.

the LIF spectrum of jet-cooled C_3 reported by Balfour *et al*. [3] (black curve). In the spectrum, one can observe all three rotational branches (P-, Q-, and R-branch) with rotational quantum numbers up to $J \approx 20$. The labeling of the bands (shown in the figure) is taken directly from the publication of Balfour *et al*. In our measurement, various lines appear which are not observable in the literature spectrum. These lines are marked with asterisks in Fig. 2. They can possibly be explained by nearby bands of C_3 belonging to transitions from a different vibrational level or, less likely, by bands from bigger carbon clusters. There exists a lot of literature on C_2 and C_3 in a larger-wavelength range and it is known that C_2 has no band in the range displayed in Fig. 2. In the literature, just a few spectra of bigger carbon clusters in the UV/vis wavelength range can be found. Except of the marked lines, our spectrum shows a very similar intensity pattern compared to the literature spectrum. Therefore, it can be concluded that the rotational temperatures are similar in both experiments.

The detection of C_3 in space was already reported in 1988 [4]. Therefore, carbon clusters are of principal astrophysical interest and, since then, several laboratory studies have been initiated. Also our group wants to contribute to the study of carbon clusters. It was found that the present laser vaporization source can also be used to create bigger carbon clusters. This conclusion could be drawn from matrix isolation spectroscopy measurements on carbon clusters produced in a similar setup. In the IR wavelength range we could identify carbon clusters with up to 25 carbon atoms. The UV/vis absorption properties of many of these aggregates are still unknown. For example, the spectrum of the cyclic C_6 is well known in the IR but not in the UV/vis [5]. Another carbon cluster, which was up to now not studied in the gas phase by direct absorption in the UV/vis, is the linear C_9. We believe that we can produce these clusters in concentrations high enough to measure their absorption spectra in the jet.

Acknowledgments

This work was supported by a cooperation between the Max-Planck-Institut für Astronomie and the FSU Jena as well as by the Deutsche Forschungsgemeinschaft.

References

[1] M. Arold, G. Rouillé, Th. Henning, and F. Huisken, Annual Report of the Institute of Solid State Physics 2007, Friedrich Schiller University (2008) p. 50

[2] P. Neubauer-Guenther, T. F. Giesen, U. Berndt, G. Fuchs, and G. Winnewisser, Spectrochim. Acta A **59**, 431 (2002)

[3] W. J. Balfour, J. Cao, C. V. V. Prasad, and C. X. W. Qian, J. Chem. Phys. **101**, 10343 (1994)

[4] K. W. Hinkle, J. J. Keady, and P. F. Bernath, Science **241**, 1319 (1988)

[5] S. L. Wang, C. M. L. Rittby, and W. R. M. Graham, J. Chem. Phys. **107**, 6032 (1997)

3. Technical reports and equipment

Operation of the Ion-accelerator JULIA and the Ion-implanter ROMEO

U. Barth, F. Jehn, G. Lenk, W. Wesch, C. Ronning

The 3 MV high current tandetron accelerator **JULIA** (***J***ena ***U***niversity ***L***aboratory for ***I***on ***A***cceleration) went in operation end of 1996. Since the beginning of the routine-operation in 1997 it has been used for different types of experiments requiring a broad spectrum of ion-beams. With the exception of helium, where the duoplasmatron ion-source followed by a lithium exchange channel was used, all ions were extracted from a sputter-type ion-source. The beam-on-target-time of 1272 h was in the same order of magnitude as in the preceding years. The 400 kV ion-accelerator **ROMEO** is in routine operation since 1998, here the beam-on-target-time of 1210 h was higher than in 2007.

Both accelerators can be operated separately or in combination. The ion-beams produced until 2008 are summarized in table 1. The ion-beam currents quoted are typical values of the ion source currents used for the experiments, the maximum currents available are significantly higher for most ions.

In 2008 some components of the 3 MV-Tandetron accelerator „JULIA" and of the 400 kV Ion-Implanter „ROMEO" were further developed:

1. The +30° beam line of the ion accelerator „JULIA" as well as the chamber for PIXE-analysis were integrated into the central computer-control station of the accelerator. New hard- and software specifically developed for this purpose permit control of the beam current and geometry. Connection of the vacuum control to the central control station now allows convenient monitoring and controlling of the vacuum.

2. A new computer program was developed to simplify crystal orientation. The software allows finding crystal axes after supplying the coordinates of the detected planar channeling dips.

Table 1. Ion-beams accelerated during 2008. The currents given are measured at the Q-Snout-Faraday-cup after the low-energy mass separator (JULIA) and at the target position (ROMEO), respectively.

Period	Element	Julia	Romeo
1	Hydrogen (H)	5 µA	4 µA
	Helium (He)	0,2 µA	4 µA
2	Lithium (Li)	2 µA	1 µA
	Boron (B)	0,2 µA	5 µA
	Carbon (C)	9 µA	10 µA
	Nitrogen (N)	10 µA	4 µA
	Oxygen (O)	17 µA	2 µA
3	Sodium (Na)	-	6 µA
	Magnesium (Mg)	-	5 µA
	Aluminium (Al)	-	4 µA
	Silicon (Si)	16 µA	4 µA
	Phosphorus (P)	-	4 µA
	Argon (Ar)	-	200 µA
4	Calcium (Ca)	-	5 µA
	Titanium (Ti)	0,7 µA	-
	Vanadium (V)	0,2 µA	1 µA
	Manganese (Mn)	0,017 µA	5 µA
	Chromium (Cr)	0,2 µA	3 µA
	Iron (Fe)	0,8 µA	2 µA
	Cobalt (Co)	-	3 µA
	Nickel (Ni)	-	6 µA
	Zinc (Zn)	1 µA	6 µA
	Gallium (Ga)	1 µA	3 µA
	Germanium (Ge)	1,6 µA	4 µA
	Arsenic (As)	0,4 µA	10 µA
	Selenium (Se)	0,5 µA	15 µA
	Bromine (Br)	19 µA	8 µA
	Krypton (Kr)	-	10 µA
5	Rubidium (Rb)	0,075 µA	1 µA
	Zirconium (Zr)	0,3 µA	1,5 µA
	Rhodium (Rh)	0,2 µA	-
	Palladium (Pd)	0,095 µA	10 µA
	Silver (Ag)	-	10 µA
	Cadmium (Cd)	-	4 µA
	Indium (In)	5 µA	8 µA
	Tin (Sn)	-	3 µA
	Antimony (Sb)	-	4 µA
	Tellurium (Te)	-	2 µA
	Iodine (I)	3 µA	-
	Xenon (Xe)	-	10 µA
6	Praseodymium (Pr)	-	1 µA
	Samarium (Sm)	0,01 µA	1,5 µA
	Europium (Eu)	0,035 µA	2 µA
	Gadolinium (Gd)	0,03 µA	-
	Erbium (Er)	0,04µA	2µA
	Tantalum (Ta)	0,2µA	2 µA
	Tungsten (W)	0,3µA	0,01µA
	Osmium (Os)	0,05 µA	-
	Iridium (Ir)	0,3µA	6 µA
	Platinum (Pt)	0,2µA	-
	Gold (Au)	24µA	20µA
	Lead (Pb)	0,035 µA	15µA
	Bismuth (Bi)	-	3µA

[1] Beam current behind LE-mass separator in Q-Snout-Faradaycup
[2] Beam current on target

As in the preceding years the ion-beam facility was used by external research groups:

3MV-Tandetron „JULIA”

University Jena
University Canberra (Mr. Hussian)
University Freiberg (Dr. Bollmann)
IPHT Jena (Dr. Diegel)
Firma Layertec (Dr. Hülsen)

400kV Implanter „ROMEO“

University Jena
Helmholtz-Zentrum Berlin (Dr. Nickel)
Universität Halle (Dr. Dubiel)
University Canberra (Mr. Hussian)
University of Pretoria (Prof. Malherbe)

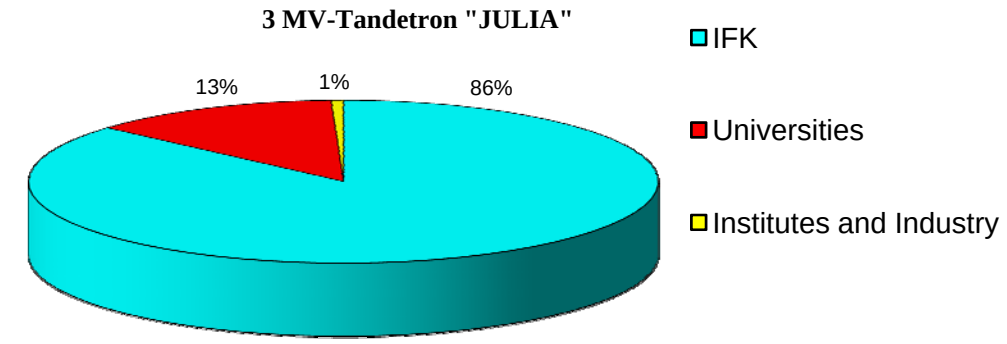

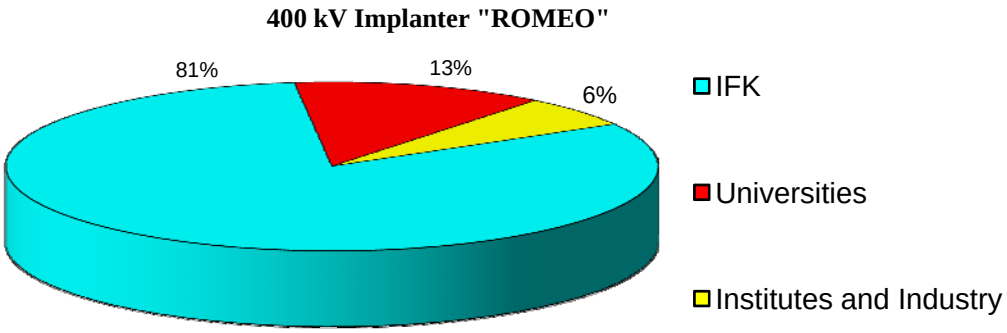

Low energy ion implanter “Mr. JIM Stringer”

R. Niepelt, J. Sommerfeld, C. Borschel, S. Geburt, M. Gnauck, M. Kozlik, C. Ronning

Ion beam techniques have a long tradition at the Institute of Solid State Physics in Jena. In autumn 2008 the ion beam equipment of the institute has been expanded with a new low energy accelerator, named “Mr. JIM Stringer” (see figure 1). This implanter complements the ion beam facilities in Jena giving access to the so far unapproachable low ion energies between a few 10 eV and some 10 keV.

Today ion beam techniques are featuring a wide range of applications in industry and science. Thereby, different physical processes are utilized for different tasks. The diversity of applications is correlated with a diversity of physical processes resulting from the usage of different ion energies. The new implanter deals with ion energies from 10 eV up to 30 keV. Possible applications in this energy field are mass selected ion beam deposition (MSIBD) of thin films, surface modification due to sputtering processes, and near surface ion implantation for surface passivation or semiconductor doping. In particular, low energy ion implantation gives access to selective doping of semiconductor nanowires, thin films and photovoltaic functional layers.

Before arriving in Jena, the accelerator has been in use at the University of Göttingen since 1998. The name of the device, Mr. JIM Stringer, is a combination of its old name used in Göttingen, Mr. Stringer, and its new second forename JIM, which stands for **J**ena **I**on i**M**planter.

The implanter features a modular design as showed in figure 2. It has a penning ion source with nearly no limits for the choice of ion species. The beam form and focus can be adjusted with several capacitors, einzel and quadrupole lenses. Mass separation is carried out by a 90 degree sector magnet, which leads to a mass resolution $m/\Delta m$ of 50 or higher allowing monoisotopic ion beam implantation. A raster scan unit allows a uniform irradiation of a 1x1 sq in sample. The installation of a quick exchange sample holder is planned for the future. The whole system is under high vacuum with a final pressure of $\sim 1 \cdot 10^{-6}$ mbar, supported by 2 new installed turbomolecular pumps.

Fig. 1 Mr. JIM Stringer in Jena, January 2009. Viewing direction goes from the deposition chamber (in the lower left of the picture) to the ion source (covered by the red box in the background).

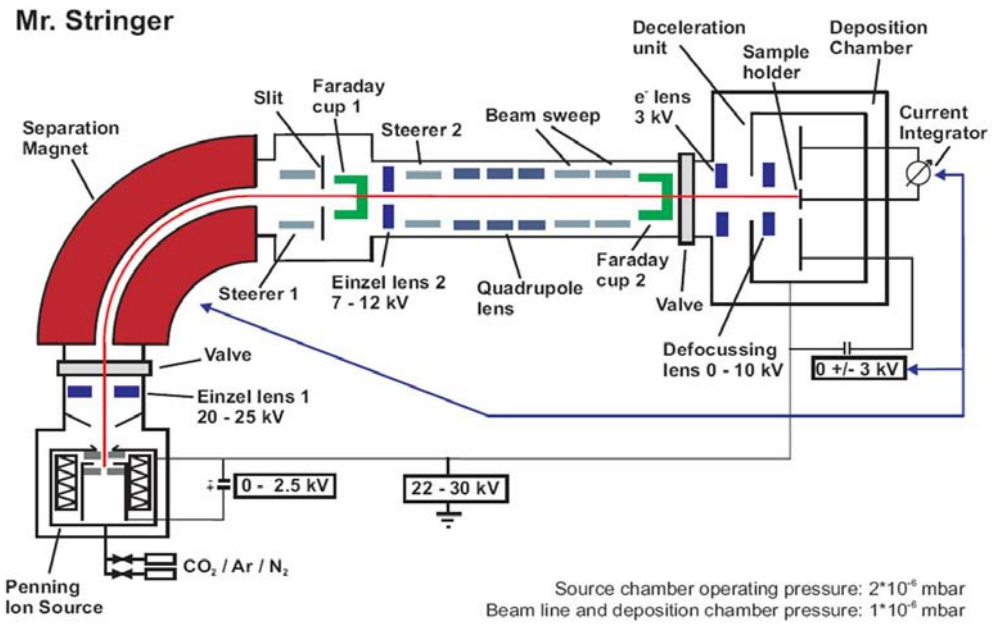

Fig. 2 Beam path and peripheral devices of ion beam implanter Mr. JIM Stringer *[Diploma Thesis H. Zutz 2006]*

The first beam with the new setup is planned to take place in February; first experiments are planned for April or May.

The main focus of attention in the first time will be on thin film synthesis and low energy ion implantation. However, there is enough space for new ideas and applications, and our group is happy about requests.

Cryogenic Services

All in-house customers of cryogenic liquids, which are all faculties of natural sciences, the medical division of the university, including several hospitals, and other external scientific institutes (e.g. Institute for Physical High Technology Jena, , Leibniz Institute Hans-Knöll Jena) as well as some private customers like the Innovent e.V. Jena or some medical practices were provided with liquid helium (LHe), high purity gases (He, N_2) and with liquid nitrogen (LN_2) by the Cryogenic Services. More than 93.000 litres of LN2 were delivered by the cryogenic services this year.

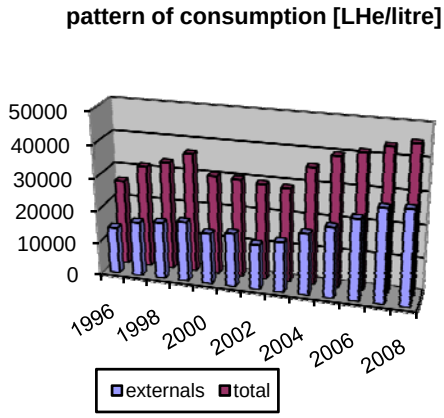

Fig. 1.: Consumption of liquid helium

As illustrated in Figure 1, the production of LHe has increased in 2008 again. The growth rate in 2008 was caused especially by high LHe- demands of the clinical users. The consumption of the scientific departments of the university kept approximately constant.
Roughly 43.500 litres of LHe were delivered which is by far the highest amount ever reached with the installed liquefier LINDE LR-20 equipment. These results were achieved by the staff in spite of expanded reconstruction periods.
In 2008 our focus was on rebuilding the main helium liquefier. The following sub-steps of the reconstruction were all accomplished on time:

- reconstruction of the water supply facility
- rebuilding of the electrical installation of the whole property
- workings on the building structure
- insertion of the 3.000 litre LHe-dewar
- mounting of a more powerful cycle compressor
- adjustment of the automatic process-oriented sequential control to implement the new components
- placement of the L70 cold-box, helium-purifier system, and plant control system
- pipe installation

After we had completed all these tasks according to our plans up to November 2008 the seller commenced the start up of the installation.

Despite of all efforts the seller hasn't been able to accomplish the commissioning of the equipment until now. Therefore the commissioning date is delayed which is in no part fault of the buyer.
We acknowledge gratefully the financial backing of the reconstruction by the administration of the Free State of Thuringia with an amount of more than 1.2 mill €. The scheduled amount of money which still has to be spend in 2008 was realised according to the financial scheme.
We were able to gain 44.000 € as a financial heightening for these project at a very late point in October 2008. This amount was used to reconstruct our refuel areas according to the legal requirements of the German Technical Inspection Authority and to expand the volume of the high pressure tanks. Both projects were completed in 2008.

Fig. 2: Assembly of the 3000 litre LHe-dewar

Fig.3 Installation workings

Equipment

Preparation of thin films and devices

- HV evaporation facilities for thermal evaporation and rf-sputtering with oxidation system
- UHV evaporation facilities, including electron gun and in situ RHEED system
- Equipment for laser deposition of thin films and material systems, especially high temperature superconductors (KrF excimer laser, $\lambda = 248$ nm)
- Molecular Beam Epitaxy (MBE) facilities:
- MBE for silicon carbide (RIBER EVA 32 R&D)
- dc and ac sputtering systems for thin films and multilayers
- Ion beam etching with Ar ions at sample temperatures down to 80 K
- Reactive ion beam etching with sample diameters up to 6 cm
- Ultrasonic wire bonder
- Equipment for photolithographic patterning

Surface analysis systems

- AUGER electron spectrometer
- Surface analysis system UNISPEC with XPS, UPS, AES, LEED, STM
- Atomic force microscopes (AFM and Microstructure Measuring Device VERITEKT 3 with needle sensor)
- Surface profilometer DEKTAK 100
- Scanning electron microscopes

Electrical and optical measurement techniques

- Electrical transport measurements (resistance, critical current density, point contact and tunneling spectroscopy)
- Hall-effect and Four-point probe equipment
- Current-voltage characteristics ($2\ K < T < 300\ K$, $B \leq 5\ T$)
- Current-voltage characteristics by microwave irradiation ($2\ GHz < f < 300\ GHz$)
- Noise measurements (frequency range 60 µHz - 100 kHz) at low temperatures
- LTS-SQUID characterization at 4.2 K (current-voltage, flux-voltage, noise, screening properties)
- HTS-SQUID characterization up to 100 K (current-voltage, flux-voltage, noise)
- 2 Deep level transient fourier spectrometers (temperature range 80 K - 690 K, 30 K - 330 K)
- 3 Admittance spectrometers (frequency range 40 Hz - 100 kHz, 20 Hz - 1 MHz and 75 kHz - 30 MHz, temperature range 30 K - 690 K)
- Optical microscopes
- Optical spectrometers, wavelength region 200 nm to 20 µm
- Low temperature photoluminescence spectroscopy
- Microwave signal generator (frequency range 1 - 20 GHz, resolution: 1 kHz)
- Electrical and optical characterization of high power diode laser arrays

Equipment for thermal treatment

- Furnace for conventional thermal treatment in inert gas atmosphere or vacuum (temperatures up to 2050 K)
- RTA apparatus (double graphite strip heater) for short time annealing

(annealing time in the order of seconds, temperature range 1000 K to 1950 K, temperature rise rate 100 K s^{-1})

Ion beam techniques

3 MV Tandetron accelerator "JULIA", equipped with

- Sputter ion source and Duoplasmatron source
- Universal beam line for ion implantation and ion beam analysis
- Second beam line for ion beam analysis, combined with implantation chamber of 400 kV implanter
- Irradiation chamber with cooled and heated sample holder and four axis goniometer

Application:

- Ion implantation: energy range 500 keV - 12 MeV, temperature range 15 K - 1500 K
- Ion beam analysis: RBS and PIXE in combination with channeling, ERDA

400 kV implanter "ROMEO", equipped with

- Hot filament, hollow cathode ion source
- Irradiation chamber with cooled and heated sample holder and four axis goniometer, combined with beam line of 3 MV Tandetron accelerator

Application:

- Ion implantation: energy range 20 keV - 400 keV, temperature range 15 K - 1500 K
- Ion implantation at low temperatures and subsequent RBS analysis using H- or He-ions from 3 MV Tandetron accelerator

Low Energy implanter "LEILA", equipped with

- Colutron Ion source 100-Q
- Colutron Ion Gun System G-2-D
- Irradiation chamber with heated sample holder

Application:

- Implantation of Hydrogen: energy range sub-keV, temperature range 300 K - 750 K

Nuclear probe technique

- 2 HP Ge-spectrometers

Low temperature measuring equipment

- He-4 cryostats for temperatures down to 4.2 K
- He-4 refrigerator for the temperature range 1.3 K - 4.2 K
- He-3 cryostat for temperatures down to 300 mK
- He-3/He-4 dilution refrigerator with a base temperature of 35 mK
- He-3/He-4 dilution refrigerator with a base temperature of 7 mK
- Electronic equipment for characterization of cryoelectronic devices
- SQUID sensor systems for magnetic measurements under unshielded conditions
- SQUID sensor system for spatially resolved magnetorelaxometry
- Cryostats (2 K < T < 300 K; optical window; magnetic field)
- Cryocoolers (Gifford-McMahon and Stirling)
- Pulse tube refrigerators (for sensor cooling)

CIS-LAB

- MBE system NEBULA for Cu(In,Ga)S_2 layers on 4'' substrates including RHEED setup
- Two HV systems for closed-space sublimation (CSS)
- Solar simulator (AM 1.5) with Current-Voltage measurement
- RF reactive sputtering system for transparent conducting oxides (TCO's) and molybdenum
- DC sputtering system for copper and indium
- UHV system ULS400 for Cu(In,Ga)(Se,S)$_2$ on (100x100) mm^2 substrates
- Scanning electron microscope JEOL JSM-6490 with LaB_6-cathode
- Quantum efficiency measurements of solar cells
- Wet chemical processing and chemical bath deposition of photoactive layers

SQUID application laboratories

- Measurement system for non-destructive evaluation in unshielded environment based on high-T_C-SQUID gradiometers
- Heart monitoring system for biomagnetic investigation in unshielded environment based on high-T_C-SQUID gradiometers
- High precision position detection system based on low-T_C-SQUIDs
- Magnet-Relaxation-Measuring System in unshielded environment based on low-T_C SQUID gradiometers

Clean room (number of particles/cu/t < 100)

- Foto lithography
- Wet chemical etching
- minimum lateral resolution: few micrometers

Shielded rooms

- Faraday room
- Magnetic shielded room

Radionuclide laboratory

- for handling of radioactive substances

Laboratory for cryogenic measurement of mechanical quality factors of gravitational wave detector components

- room temperature stability of ± 0.2 K at best
- vibration isolation (decoupled foundation)
- acoustic isolation
- remote controlled operation of the measurement equipment
- separated room for disturbing machines (e.g. pumps)
- full supply of technical media to perform cryogenic measurements

4. Current research projects

(A) Supported by the Bundesministerium für Bildung, Wissenschaft, Forschung und Technologie (BMBF), Bundesministerium für Wirtschaft und Arbeit (BMWi), and Bundesministerium für Umwelt, Naturschutz und Reaktorsicherheit (BMU)

Characterization of irradiated GaN and ZnO
Prof. Dr. W. Wesch, Prof. M. Hayes 39.6.L1A.6.B 01/04 – 06/07

Ioneninduzierte Strukturumbildungs- und Ausheilprozesse in Halbleitern
Teilprojekt 4 im Verbund Hochauflösende in-situ-Charakterisierung der Strukturumbildungsprozesse in Halbleitern
Verbund Forschung mit Sonden und Ionenstrahlen im Gesamtverbund Erforschung der kondensierten Materie mit Großgeräten
Prof. Dr. W. Wesch 05KK7SJ1 07/07 – 06/10

Computational Materials Science gestützte Optimierung des Wirkungsgrades von CIGS-Dünnschichtsolarzellen
Prof. Dr. W. Wesch 0327665E 06/07 – 05/11

CdTe-CdS-Solarzellen hoher Effizienz für eine verbesserte Modul-Produktionstechnologie
Prof. Dr. W. Wesch, Prof. Dr. W. Witthuhn 0329881A 09/08 – 08/11

(B) Supported by the Deutsche Forschungsgemeinschaft (DFG)

Vertical, strained 1D silicon nanostructures and devices
Dr. E. Wendler WE 1648/6-1 04/05 – 06/08

Strukturierungsverfahren für mikro- und nanooptische Elemente in Lithiumniobat
E.-B. Kley, F. Schrempel KL 1199/2-1 05/07 – 04/09

Characterization of structural and optical properties of $Si_{1-x}Ge_x$nanocrystals produced by laser-induced pyrolysis and by ion implantation
Prof. Dr. Fr. Huisken, Prof. Dr. W. Wesch HU 474/19-1 09/07 – 08/09

Gütemessungen bei kryogenen Temperaturen
(Teilprojekt C 4 im SFB/TR 7 „Gravitationswellenastronomie“)
Prof. Dr. P. Seidel, Dr. W. Vodel, Prof. A. Tünnermann DFG–SFB/TR7 01/03 – 12/10

Ion beam doping of semiconductor nanowires
Fortsetzung des DFG-Projektes im Rahmen des Schwerpunktprogramms 1165: Nanodrähte und Nanoröhren: Von kontrollierter Synthese zur Funktion
Prof. C. Ronning Ro1198/7-2 07/06 – 06/10

(C) Support by the EU

Biological diagnostic tools using microsystems and supersensitive magnetic detection (BIO-DIAGNOSTICS)
Prof. Dr. P. Seidel, Prof. Dr. J. Haueisen EU (6. Rahmenprogramm) 11/05 – 10/08

(D) Supported by the Thüringer Kultusministerium (TKM)

Ionenstrahlmodifikation und -analyse von Titanoberflächen
Prof. Dr. W. Wesch 02/9125 IBA Heiligenstadt 05/02 – 12/08

Dünnschicht Solarzellen der dritten Generation: transparente Dünnschicht Solarzellen/Tandem-Solarzellen
Prof. Dr. W. Wesch B 515-06012 10/06 – 09/08

Heliumverflüssigungsanlage
Prof. P. Seidel TKM 10/07 – 03/09

Ortsaufgelöste Kathodenlumineszenz-Untersuchungen an Halbleitern
Prof. Dr. C. Ronning B 715-08010 06/08 – 09/09

(E) Supported by other institutions

Experimente zur Labor-Astrophysik
Prof. Dr. Fr. Huisken MPI Heidelberg 01/02 – 05/12

Kryostromkomperator für DESY Hamburg
Dr. W. Vodel DESY Hamburg 01/01 – 12/09

Zerstörungsfreie Strahldiagnose für Linear- und Ringbeschleuniger
Dr. W. Vodel GSI Darmstadt 01/07 – 12/09

The experimental, analytical and numerical investigation of the current – voltage characteristics of intrinsic Josephson junctions under microwave radiation
Prof. Dr. P. Seidel, Dr. Yu. M. Shukrinov Heisenberg-Landau Programm 01/05 – 12/08

Elektronenspektroskopische Untersuchungen der Oberflächen von Laserbauteilen
Dr. B. Schröter LASOS GmbH Jena 02/07 – 02/09

Analyse von Schichtsystemen mittels Auger-Elektronen-Spektroskopie
Dr. B. Schröter TU Berlin 12/07 – 11/08

Untersuchungen von CIGS-Photovoltaikzellen, hergestellt im Non-Vakuumverfahren
Prof. Dr. W. Wesch KF0314502DA6 09/06 – 12/09

5. Publications

5.1 Publications in scientific journals

M.A. Zimmer, D. Stichtenoth, C. Ronning, Wei Yi, V. Narayanamurti, T. Voss, F. Capasso
Scalable Fabrication of Nanowire Photonic and Electronic Circuits Using Spin-on Glass
Nano Letters Vol. 8, No. 6 (2008) 1695-1699

A. Colli, A. Fasoli, C. Ronning, S. Pisana, St. Piscanec, A. Ferrari
Ion Beam Doping of Silicon Nanowires
Nano Letters Vol. 8, No. 8 (2008) 2188-2193

H. Hartung, E.-B. Kley, A. Tünnermann, Th. Gischkat, F. Schrempel, W. Wesch
Fabrication of ridge waveguides in zinc-substituted lithium niobate by means of ion-beam enhanced etching
Opt. Lett. 33 (2008) 2320-2322.

D. Stichtenoth, K. Wegener, C. Gutsche, I. Regolin, F.J. Tegude, W. Prost, M. Seibt, C. Ronning
P-type doping of GaAs nanowires
Applied Physics Letters Vol. 92 (2008) 163107

M.A. Zimmler, J. Bao, F. Capasso, S. Müller, C. Ronning
Laser action in nanowires: Observation of the transition from amplified spontaneous emission to laser oscillation
Applied Physics Letters Vol. 93 (2008) 051101

M. Schumm, M. Koerdel, S. Müller, H. Zutz, C. Ronning, J. Stehr, D.M. Hofmann, J. Geurts
Structural impact of Mn implantation on ZnO
New Journal of Physics 10 (2008) 043004

T. Steinbach, F. Schrempel, Th. Gischkat, W. Wesch
Influence of ion energy and ion species on ion channeling in $LiNbO_3$
Physical Review B 78 (2008) 184106.

A. Kamarou, W. Wesch, E. Wendler, A. Undisz, M. Rettenmayr
Radiation damage formation in InP, InSb, GaAs, GaP, Ge, and Si due to fast ions
Physical Review B 78 (2008) 054111

J. Reinisch, F. Schrempel, Th. Gischkat, W. Wesch
Etching of Ion Irradiated $LiNbO_3$ in Aqueous Hydrofluoric Solutions
J. Electrochem. Soc. 155 (4) (2008) D298-D301.

D. Stichtenoth, J. Dürr, C. Ronning, L. Wischmeier, T. Voss
Characterization of the donar-acceptor-pair transition in Nitrogen-implanted zinc oxide
Journal of Applied Physics 103 (2008) 83513

K. Lauer, A. Laades, H. Übensee, H. Metzner, A. Lawerenz
Detailed analysis of the microwave-detected photoconductance decay in crystalline silicon
Journal of Applied Physics 104 (2008) 104503

S. Müller, M. Lorenz, Chr. Czekalla, G. Benndorf, H. Hochmuth, M. Grundmann, H. Schmidt, C. Ronning
Intense white photoluminescence emission of V-implanted zinc oxide thin films
Journal of Applied Physics 104 (2008) 123504

S. Geburt, D. Stichtenoth, S. Müller, W. Dewald, C. Ronning, J. Wang, Y. Jiao, Y.Y. Rao, S.K. Hark, Quan Li

Rare Earth Doped Zinc Oxide Nanowires
Journal of Nanoscience and Nanotechnology Vol. 8, 244-25, 2008

W.-Y. Wu, J.-M. Ting, H. Zutz, D. Lyzwa, I. Gerhards, C. Ronning, H. Hofsäss
Comparative study of self-assembling of multilayers using reactive sputter deposition and mass selective ion beam deposition
Diamond & Related Materials 17 (2008) 1494-1497

Juan Wang, Quan Li, C. Ronning, D. Stichtenoth, S. Müller, D. Tang
Nanomaterial electronic structure investigation by valence electron energy loss spectroscopy - An example of doped ZnO nanowires
Micron 39 (2008) 703-708

N. Bibic, V. Milinovic, M. Milosavljevic, F. Schrempel, M. Siljegovic, K.P. Lieb
Effects of the Ar ions pre-amorphization of Si substrateon interface mixing of Fe/Si bi-layers
J. Microsc.-Oxf. 232 (2008) 184106.

M. Katsikin, F. Pinakidou, E.C. Paloura, F. Boscherini, E. Wendler and W. Wesch
X-ray absorption fine structure study of In implanted GaN: Effect of annealing
Mater. Sci. Eng. B 152 (2008) 132-135

M. Dubiel, H. Hofmeister, E. Wendler
Formation of nanoparticles in soda-lime glasses by single and double ion implantation
J. Non-Cryst. Solids 354 (2-9) (2008) 607-611.

L. Chen, T. Niebling, W. Heimbrodt, P.J. Klar, D. Stichtenoth, C. Ronning
Energy Transfer and Dynamics of the Mn 3d5 Luminescence in Low Dimensional (Zn,Mn)S Nanostructures
Journal of the Korean Physical Society, Vol. 53, No.5, (2008) 2830-2834

F. Komarov, L. Vlasukova, W. Wesch, A. Kamarou, O. Milchanin, S. Grechnyi, A. Mudryi, A. Ivaniukovich
Formation of InAs nanocrystals in Si by high-fluence ion implantation
Nucl. Instr. and Methods B 266 (2008) 3557-3564.

F. Schrempel, T. Steinbach, Th. Gischkat, W. Wesch
Channeling irradiation of $LiNbO_3$
Nucl. Instr. and Methods B 266 (2008) 2958-2961.

Th. Gischkat, F. Schrempel, W. Wesch
Ion-beam induced effects at 15 K in $LiNbO_3$
Nucl. Instr. and Methods B 266 (2008) 2906-2909.
E. Wendler, K. Gärtner, W. Wesch
Comparison of ion-induced damage formation in <110> and <100> MgO
Nucl. Instr. and Methods B 266 (2008) 2872-2876.

K. Bharuth-Ram, H. Hofsäss, C. Ronning
Electric field gradients at ^{151}Eu sites in GaN
Hyperfine Interaction 184 (2008) 213-216

M. Hayes, F. Schrempel, S.M.M. Coelho, F.D. Auret, J.M. Nel, W. Wesch
RBS investigations of annealed gold layers on crystalline germanium
J. Phys. Conf. Ser. 100 (2008) 042005.

M. Hayes, A. Schroeter, E. Wendler, W. Wesch, F.D. Auret, J.M. Nel
Damage formation in Ge during Ar^+ implantation at 15 K
phys. stat. sol. (c) 5 (2008) 583-586.

A. Schüller, K. Gärtner, H. Winter
Interaction potential for fast Ne atoms in front of LiF(001) surface
EPL, 81 (2008) 37007

A. Martin, H. Armandula, C. Comtet, M.M. Fejer, A. Gretarsson, G. Harry, J. Hough, J.-M. M Mackowski, I. MacLaren, C. Michel, J.-L. Montorio, N. Morgado, R. Nawrodt, S. Penn, S. Reid, A. Remillieux, R. Route, S. Rowan, C. Schwarz, P. Seidel, W. Vodel, A. Zimmer
Measurements of a low-temperature mechanical dissipation peak in a single layer of Ta_2O_5 doped with TiO_2
Class. Quantum Grav. **25** 055005, 2008

C. Becker, A. Steppke, T. Koettig, J. Gerster, L. Dörrer, M. Thürk, F. Schmidl, P. Seidel
Operation of a high-T_c DC-SQUID-gradiometer on a non-metallic pulse tube refrigerator
Journal of Physics: Conference Series 97, 012039, 2008

A. Steppke, C. Becker, V. Grosse, L. Dörrer, F. Schmidl, P. Seidel, M. Djupmyr, J. Albrecht
Planar high-T_c superconducting quantum interference device gradiometer for simultaneous measurements of two magnetic field gradients
Appl. Phys. Lett 92 (2008) 122504

R. Nawrodt, A. Zimmer, T. Köttig, Ch. Schwarz, D. Heinert, M. Hudl, R. Neubert, M. Thürk, S. Nietzsche, W. Vodel, P. Seidel
High Mechanical Q-factor measurements on silicon bulk samples
Journal of Physics: Conference Series 122 (2008) 012008

P. Seidel, C. Becker, A. Steppke, U. Schinkel, K. Hoefer, V. Grosse, S. Engmann, F. Schmidl, L. Redlich
Higher Order HTSC Gradiometer for Measurements in Unshielded Environment
IEEE/CSC &ESAS European Superconductivity News Forum (ESNF), No. 6, 2008

J. Martin, F. Cichos, F. Huisken, Chr. von Borczyskowski
Electron-phonon coupling and localization of excitons in single silicon nanocrystals
Nano Letters 8, 656-660 (2008)

C. Jäger, H. Mutschke, I. Llamas-Jansa, Th. Henning, F. Huisken
Laboratory analogs of carbonaceous matter: Soot and its precursors and by-products
Organic Matter in Space, IAU Symposium and Colloquium Proceedings Series No. 251 (2008) pp. 425-432

A. Staicu, G. Rouillé, Th. Henning, F. Huisken, D. Pouladsaz, R. Scholz
S1 ← S0 transition of 2,3-benzofluorene at low temperatures in the gas phase

J. Chem. Phys. 129, 074302-1-10 (2008) .

G. Rouillé, C. Jäger, M. Steglich, F. Huisken, Th. Henning, G. Theumer, J. Bauer, H.-J. Knölker
IR, Raman, and UV/Vis spectra of corannulene for use in possible interstellar identification
Chem. Phys. Chem. 9, 2085-2091 (2008)

C. Jäger, H. Mutschke, Th. Henning, F. Huisken
Spectral properties of gas-phase condensed fullerene-like carbon nanoparticles from far-ultraviolet to infrared wavelengths
Astrophys. J. 689, 249-259 (2008) .

5.2 Invited talks and colloquia

C. Jäger
Laboratory analogs of carbonaceous matter - Soot, its precursor and by-products
International Astronomical Union Symposium 251 "Organic Matter in Space", February 18 – 22, 2008, Hong Kong, China

C. Borschel
RBS and Channeling measurements of Si/Y_2O_3/Si heterostructures
Institut für innovative Mikroelektronik (IHP), Seminar, Frankfurt (Oder), 10.03.2008

F. Huisken
Photoluminescence studies of silicon nanocrystals as free particles and embedded in quartz windows
NanoLum, European Workshop on Luminescent Nano-Objects, Les Houches, France, March 17 – 20, 2008

R. Nawrodt, C. Schwarz, D. Heinert, W. Vodel, A. Tünnermann, P. Seidel
Cryogenic loss measurements in bulk materials
GWADW 2008 – VESF meeting, Gravitational Wave Advanced Detector Workshop, LaBiodola, Isola d'Elba, Italy, Mai 2008

C. Ronning
Ionenimplantation in ZnO: Volumenkristalle und Nanodrähte
Freie Universität Berlin, Seminar AG Magnetismus, 04.07.2008

F. Huisken
Photoluminescence studies of free and embedded silicon nanocrystals in the frequency and time domain
15th International Conference on Luminescence and Optical Spectroscopy of Condensed Matter (ICL'08), Lyon, France, July 7 – 11, 2008

C. Ronning
Ion beam doping of semiconductor nanowires
Forschungszentrum Dresden-Rossendorf, Kolloquium Ionenstrahlphysik und Materialforschung, 10.07.2008

F. Huisken
Electronic spectroscopy of biological molecules in supersonic jets: The amino acid tryptophan
26th International Symposium on Rarified Gas Dynamics, Kyoto, Japan, July 21 – 25, 2008

W. Wesch, O. Picht, M. Steinert, U. Kaiser, J. Biskupek, A. Undisz, M. Rettenmayr, R. Rubinger, N.A. Sobolev
Ion beam synthesis of transition metal nanoclusters in silicon
20th International Conference on the Application of Accelerators in Research and Industry (CAARI), Fort Worth, USA, August 10 - 15, 2008

E. Wendler
Mechanisms of damage formation in semiconductors
23rd International Conference on Atomic Collisions in Solids (ICACS-23), Phalaborwa, South-Africa, August 17 to 22, 2008

C. Jäger
Analogs of cosmic dust
Cosmic Dust Near and Far, Heidelberg, Germany, September 08 – 12, 2008

W. Vodel
Cryogenic Q-factor measurements of optical materials
5th German Vietnam Summer School, Hanoi and Ho Chi Minh City, Vietnam, September 08 to 09, 2008

W. Vodel, R. Nawrodt
High precision LASER interferometer for application in gravitational wave detectors
International Workshop on Photonics & Applications, Nha Trang, Vietnam, 10.09.-14.09. 2008

F. Schrempel, Th. Gischkat, H. Hartung, E.B. Kley, A. Tünnermann, W. Wesch
Patterning of lithium niobate for the fabrication of novel micro- and nano-optical devices by means of ion beam enhanced etching
6th Fraunhofer IISB Lithography Simulation Workshop, Athens, Greece, 19.09.-20.09.2008

H. Metzner
CdTe-CdS-Solarzellen hoher Effizienz für eine verbesserte Modul-Produktionstechnologie
BMU Statusseminar Photovoltaik 2008, Berlin, 12.11.2008

D. Heinert, C. Schwarz, R. Nawrodt, W. Vodel, A. Tünnermann, P. Seidel
Loss measurements in bulk materials at low temperatures
ET-ILIAS GW meeting, Cascina/Italy, November 2008
C. Ronning
Halbleiternanodrähte: Eigenschaften und Dotierung
Forschungszentrum Dresden-Rossendorf, Symposium Nanostrukturen, December 12, 2008

5.3 Conference contributions

Frühjahrstagung der DPG, Dresden, Germany, February 25 - 29, 2008

H. Zutz, D. Lyzwa, I. Gerhards, C. Ronning, M. Seibt, H. Hofsäss
Carbon-Metal-Nanocomposites: Self-organization of multilayers during the co-deposition of energetic ions

K. Zhang, H. Hofsäss, F. Rotter, K. Jesiek, M. Uhrmacher, C. Ronning, J. Krauser
Morphology of ion-beam eroded Si surface: Sputtering at near normal and glancing incident angles

H. Zutz, D. Lyzwa, I. Gerhards, C. Ronning, M. Seibt, H. Hofsäss
Co-deposition of energetic carbon and Copper ions: Self-organization of multilayers

M. Brötzmann, H. Zutz, A.-K. Nix, C. Ronning, H. Hofsäss
Growth and electrical characterization of c-BN/ZnO-heterostructures

K. Wegener, S. Müller, D. Stichtenoth, W. Dewald, C. Ronning, C. Gutsche, A. Lysov, K. Blekker, W. Prost, F.-J. Tegude
Electrical integration of semiconductor nanowires

S. Müller, C. Ronning, MinJie Zhou, Quan Li
Optical and structural properties of transition metal implanted ZnO nanowires

K. Wegener, D. Stichtenoth, C. Ronning, C. Gutsche, W. Prost, F.-J. Tegude
Ion implanted GaAs nanowire pn junctions

A.-K. Nix, S. Müller, C. Ronning, A. Kanarou, E. Wendler, W. Wesch, C. Trautmann, H. Hofsäss
Swift heavy ion irradiation for recovery from implantation defects of GaN

J. Dürr, D. Stichtenoth, S. Müller, C. Ronning, A. B. Pinto, J. Malindretos, L. Wischmeier, T. Voss
Optical and electrical characterization of acceptors implanted into ZnO

S. Müller, C. Ronning, M. Lorenz, C. Czekalla, G. Benndorf, H. Hochmuth, M. Grundmann, H. Schmidt
White luminescence of vanadium implanted ZnO PLD films

L. Chen, S. Al-Azzaui, W. Heimbrodt, D. Stichtenoth, S. Müller, C. Ronning
Magneto-optical properties of ZnO with Mn ion-beam implantation

M. Koerdel, M. Schumm, F. Bach, H. Zhou, W. Szuszkiewicz, S. Müller, C. Ronning, J. Geurts
Study of the solubility limits and secondary phase formation for ZnO:TM (TM = V, Fe, Co, Ni) mixed crystals by Raman spectroscopy

M. Schumm, M. Koerdel, S. Müller, H. Zutz, C. Ronning, J. Stehr, D.M. Hofmann, J. Geurts

The structural impact of Mn implantation on a ZnO host lattice and the magnetic interaction of the implanted Mn ions studied by Raman scattering and Electron Paramagnetic Resonance

T. Niebling, M. Demper, Limei Chen, W. Heimbrodt, P. Klar, D. Stichtenoth, C. Ronning
Energy transfer and excitation dynamics in doped 1D- and 2D-nanostructures

Th. Gischkat, F. Schrempel, W. Wesch
Ion beam induced effects at 15K in z-cut $LiNbO_3$

T. Steinbach, F. Schrempel, Th. Gischkat, W. Wesch
Channeling irradiation of $LiNbO_3$

M. Steinert, A. Undisz, M. Rettenmayr, W. Wesch
Ion beam synthesis of Mn/Sb clusters in silicon

K. Lauer, A. Laades, A. Lawerenz, H. Übensee, H. Metzner
Measurement of interstitial iron content in multicrystalline silicon by microwave detected photoconductance decay

H. Kleemann, P. Zeigermann, M. Blech, M. Steglich, B. Schröter
Growth and characterization of single-wall carbon nanotubes for electronic and optical applications

P. Zeigermann, H. Kleemann, M. Janietz, M. Steglich, B. Schröter
Selective growth and treatment of carbon nanotubes on various substrates

Ch. Pansow, M. Trautmann, M. Büenfeld, V. Große, F. Schmidl, P. Seidel
Laser deposition of niobium as a refractory metal

M. Büttner, F. Schmidl, P. Seidel, M. Röder, P. Görnert, C. Lang, D. Schüler
Untersuchung von Magnetosomen mittels temperaturabhängiger Magnetorelaxometrie

M. Trautmann, Ch. Pansow, M. Büenfeld, V. Große, F. Schmidl, P. Seidel
Fabrication of Cobalt clusters by pulsed laser deposition
F. Schmidl, M. Büttner, Ch. Becker, A. Steppke, P. Kossebau, S. Prass, P. Seidel
Relaxationsmessungen mit SQUID Gradiometern

S. Engmann, U. Schinkel, V. Große, Ch. Becker, A. Steppke, F. Schmidl, P. Seidel
Electrical properties of thin $YBa_2Cu_3O_7$-X films with embeded gold nano clusters

U. Schinkel, Ch. Becker, V. Große, A. Steppke, F. Schmidl, P. Seidel
Two dimensional planar superconducting quantum interference device gradiometer on a $SrTiO_3$ bicrystal

René Geithner, Alexander Steppke, Ralf Neubert, Wolfgang Vodel, Paul Seidel
Measurements of amorphous and nanocrystalline ferromagnetic materials at low temperatures

Ch. Becker, A. Steppke, U. Schinkel, M. Büttner, V. Große, H. Schneidewind, F. Schmidl, P. Seidel
Planar flip-chip THSC Dc-SQUID gradiometers for nondestructive evaluations

D. Heinert, A. Schroeter, C. Schwarz, R. Nawrodt, R. Neubert, M. Thürk, W. Vodel, A. Tünnermann, P. Seidel
Mechanical loss mechanisms in crystalline quartz

C. Schwarz, R. Nawrodt, D. Heinert, A. Schroeter, R. Neubert, M. Thürk, W. Vodel, A. Tünnermann, P. Seidel
High Mechanical Q-factor Measurements on Silicon Bulk Material

S. Kroker, C. Schwarz, D. Heinert, R. Nawrodt, A. Schroeter, R. Neubert, M. Thürk, S. Nietzsche, W. Vodel, A. Tünnermann, P. Seidel
Measurement of the internal mechanical dissipation in dielectric thin films

NanoLum, European Workshop on Luminescent Nano-Objects, Les Houches, France, March 17 – 20, 2008

T. Schmidt
Luminescence studies on silicon- and germanium-based nanoparticles synthesized by laser-induced pyrolysis

J. Sommerfeld
Synthesis of pure Si and Si_xGe_{1-x} nanoparticles by laser-induced pyrolysis and related investigations on cluster beam intensities

Workshop Ionenstrahlphysik und Nanotechnologie, Darmstadt, Germany, April 11 to 12, 2008

F. Schrempel
Three-dimensional patterning of Lithiumniobat

W. Wesch
Structural modification of swift heavy ion irradiated amorphous Ge layers

M. Steinert
Ion beam synthesis of Mn/Sb clusters in silicon

International Conference on Isolated Biomolecules and Biomolecular Interactions (IBBI08), Valladolid, Spain, April 13 – 18, 2008

G. Rouillé
UV absorption spectroscopy of L-tryptophan in the gas phase

2nd International Conference on New Diamond and Nano Carbons (NDNC2008), Taipei, Taiwan, May 26 – 29, 2008

F. Huisken
Gas-phase condensation of nanometer- and subnanometer-sized carbon grains and polycyclic aromatic hydrocarbons

Workshop "Nanoelectronic Days", Aachen,Germany, May 13 – 16, 2008

C. Gutsche, I. Regolin, W. Prost, F.-J. Tegude, D. Stichtenoth, K. Wegener, M. Seibt, C. Ronning
Ion implanted GaAs-nanowires

E-MRS 2008 Spring Meeting, Strasbourg, France, May 26 – 30, 2008

J. Eberhardt, J. Cieslak, H. Metzner, Th. Hahn, R. Goldhahn, F. Hudert, J. Kräußlich, U. Kaiser, A. Chuvilin, U. Reislöhner und W. Witthuhn
Epitaxial and Polycrystalline $CuInS_2$ Layers: Structural Metastability and its Influence on the Photoluminescence

M. Hädrich, C. Kraft, C. Löffler, H. Metzner, U. Reislöhner und W. Witthuhn
Pathways to Thin Absorbers in CdTe Solar Cells

15th Workshop on Dielectrics in Microelectronics, Bad Saarow (Berlin), Germany, June 23 – 25, 2008

C. Borschel, C. Ronning, H. Hofsäss, A. Giussani, P. Zaumseil, C. Wenger, P. Storck, T. Schroeder
Structure and Defects of Epitaxial Si(111) Layers on Y_2O_3(111)/Si(111) Support Systems

TMS Electronic Materials Conference, Santa Barbara, USA, June 25 – 27, 2008

C. Gutsche, I. Regolin, F.J. Tegude, W. Prost, D. Stichtenoth, K. Wegener M. Seibt, C. Ronning
Electrical and structural characterization of ion implanted GaAs nanowires

ICEC 22 – ICMC 2008, International Cryogenic Engineering Conference, Seoul, Korea, July 21 – 25, 2008

R. Nawrodt
Cryogenic Setup for Q-factor Measurements on Bulk Materials for Future Gravitational Wave Detectors

20th International Conference on the Application of Accelerators in Research and Industry (CAARI), Fort Worth, USA, August 10 - 15, 2008

W. Wesch, O. Picht, M. Steinert, U. Kaiser, J. Biskupek, A. Undisz, M. Rettenmayr, R. Rubinger, N.A. Sobolev
Ion beam synthesis of transition metal nanoclusters in silicon

ASC 2008 – Applied Superconductivity Conference, Chicago, Illinois, USA, August 17 to 22, 2008

P. Seidel, C. Becker, A. Steppke, U. Schinkel, K. Hoefer, V. Grosse, S. Engmann, F. Schmidl, L. Redlich
Higher Order HTSC Gradiometer for Measurements in Unshielded Environment

A. Steppke, R. Geithner, R. Nawrodt, W. Vodel, M. Schwickert, H. Reeg, P. Seidel
Applikation of LTS-SQUIDs in Nuclear Measurement Technique

23rd International Conference on Atomic Collisions in Solids (ICACS-23), Phalaborwa, South-Africa, August 17 to 22, 2008

E. Wendler
Mechanisms of damage formation in semiconductors

E. Wendler, O. Bilani, K. Gärtner, W. Wesch, M. Hayes, F. D. Auret, K. Lorenz, E. Alves
Radiation damage in ZnO ion implanted at 15 K

International Conference on Ion Beam Modification of Materials (IBMM08), Dresden, Germany, September 01 – 05, 2008

C. Borschel, M. Schnell, C. Ronning, H. Hofsäss
A Computer Program for the Analysis of High Resolution RBS Spectra

H. Zutz, D. Lyzwa, I. Gerhards, M. Seibt, C. Ronning, H. Hofsäss
Self-organization of multilayers during co-deposition of energetic ions

R. Niepelt, C. Ronning, K. Zhang, H. Hofsäss
Surface evolution of crystalline ZnO and MgO induced by medium energy sputtering
Th. Gischkat, F. Schrempel, W. Wesch
Annealing behavior of He implanted $LiNbO_3$

M. Steinert, W. Wesch, A. Undisz, M. Rettenmayr, R. Borges, M. Godinho, R. Rubinger, M.C. Carmo, N.A. Sobolev
Ion beam synthesis of Mn/Sb clusters in silicon

W. Wesch, C.S. Schnohr, P. Kluth, Z.S. Hussain, L.L. Araujo, R. Giulian, D.J. Sprouster, A.P. Byrne, M.C. Ridgway

Structural modification of swift heavy ion irradiated amorphous Ge layers

Z.S. Hussain, C.S. Schnohr, E. Wendler, W. Wesch, G.J. Foran, M.C. Ridgway
Amorphisation of compound semiconductors – New insight into ternary compounds

F. Komarov, L. Vlasukova, O. Milchanin, A. Komarov, W. Wesch, A. Mudryi
Influence of ion implantation and annealing conditions on the growth of InAs nanocrystals in silicon

P. Gaiduk, A.N. Larsen, W. Wesch
Er^+ implantation in SnO_2:SiO_2 layers: Structure changes and light emission

Cosmic Dust Near and Far, Heidelberg, Germany, September 8 – 12, 2008

F. Huisken
Can silicon nanocrystals be the carrier of ERE?

G. Rouillé
Spectroscopic characterization of astrophysically relevant molecules

DPG Summerschool "Functional Nanostructures", Bad Honnef, Germany, September 15 – 19, 2008

T. Schmidt
Luminescence studies on single silicon nanoparticles synthesized by laser-induced pyrolysis

16th International Conference of Ternary and Multinary Compounds (ICTMC 16), Berlin, Germany, September 15 - 19, 2008

J. Cieslak, Th. Hahn, J. Kräußlich, H. Metzner, J. Eberhardt und W. Witthuhn
Twinning in Cu(In,Ga)S_2

M. Oertel, Th. Hahn, H. Metzner und W. Witthuhn
$CuInSe_2$ Solar Cells by Sequential Absorber Layer Processing

C. Kraft, M. Hädrich, H. Metzner, C. Löffler, U. Reislöhner und W. Witthuhn
Formation of CdTe1-xSx at the p-n Junction of CdS-CdTe Solar Cells
Poster award for M. Hädrich

Th. Hahn, J. Cieslak, J. Eberhardt, H. Metzner und W. Witthuhn
Hillock-formation in chalcopyrite thin films

34th International Conference on Micro and Nano Engineering (MNE), Athens, Greece, September 15 - 18, 2008

F. Schrempel, Th. Gischkat, H. Hartung, E.B. Kley, A. Tünnermann, W. Wesch
Micro- and nano-patterning of lithium niobate

Th. Gischkat, H. Hartung, F. Schrempel, E.B. Kley, A. Tünnermann, W. Wesch
Patterning of $LiNbO_3$ by means of ion irradiation and wet etching

6th Fraunhofer IISB Lithography Simulation Workshop, Athens, Greece, September 19 to 20, 2008

F. Schrempel, Th. Gischkat, H. Hartung, E.B. Kley, A. Tünnermann, W. Wesch
Patterning of lithium niobate for the fabrication of novel micro- and nano-optical devices by means of ion beam enhanced etching

5th International Workshop on ZnO and Related Materials, Ann Arbor, Michigan, USA, September 22 - 24, 2008

S. Müller, H. Zutz, M. Schumm, M. Koerdel, J. Geurts, C. Ronning
Structural impact of transition metal implantation on ZnO

S. Müller, M.J. Zhou, Q. Li, C. Ronning
Optical properties of transition metal implanted ZnO nanowires

Fall meeting of the Materials Research Society (MRS), Boston, USA, November 30 to December 05, 2008

C. Borschel, R. Niepelt, S. Geburt, C. Gutsche, I. Regolin, W. Prost, F.J. Tegude, D. Stichtenoth, D. Schwen, and C. Ronning
Ion beam alignment of semiconductor nanowires

T. Voss, J.-P. Richters, R. Imlau, S. Mueller, C. Borschel, R. Niepelt, C. Ronning
Changes of the Photoluminescence Properties in Metal-Coated ZnO Nanowires

M. A Zimmler, J. Bao, S. Müller, K. A Sunter, C. Ronning, F. Capasso
Laser Oscillation Thresholds for ZnO Nanowires

Workshop ”Towards Reality in Nanoscale Materials '08”, Levi, Finnland, December 03 to 05, 2008

C. Borschel, R. Niepelt, S. Geburt, C. Gutsche, I. Regolin, W. Prost, F.J. Tegude, D. Stichtenoth, D. Schwen, and C. Ronning
Ion beam alignment of semiconductor nanowires

2nd International Workshop on Semiconducting Nanoparticles – Photovoltaics and Optoelectronics, Duisburg, Germany, December 10 – 12, 2008

L. Ma
Photoluminescence studies of Ge_xSi_{1-x} nanocrystals produced by laser-induced pyrolysis

T. Schmidt
Luminescence studies on single silicon nanoparticles synthesized by laser-induced pyrolysis

5.4 Theses

Diploma Theses

Michael Blech	*Kontrolliertes Wachstum und Analyse metallischer Nanopartikel als Katalysatoren für Kohlenstoffnanoröhren*
Christian Borschel	*Analysis of Thin Films and Their Interfaces Using High Resolution Rutherford Backscattering Spectrometry* (extern Universität Göttingen)
Joachim Dürr	*Charakterisierung von Akzeptoren in Zinkoxid* (extern Universität Göttingen)
Sebastian Engmann	*Untersuchungen an $YB_2Cu_3O_{7-x}$-$SrTiO_3$ Metallkontaktsystemen auf $LaAlO_3$ Substraten*
Sebastian Geburt	*Lanthanoid-dotierte ZnO-Nanodrähte* (extern Universität Göttingen)
Manuela Janietz	*Untersuchungen zur Funktionalisierung sowie thermischer und chemischer Behandlung von Kohlenstoffnanoröhren auf Oberflächen*
Michael Kieschnick	*Formierung von Ge und GeSi-Nanoclustern In Quarzglas (a-SiO_2)*
Hans Kleemann	*Lokal aufgelöste Charakterisierung von Kohlenstoffnanoröhren*
Roland Koim	*Spurenelementanalyse in Milchzähnen mittels Teilcheninduzierter Röntgenemission (PIXE)*
Christian Lehmann	*Optimierung von laserkristallisierten Dünnschichtsolarzellen auf Siliziumbasis* (extern IPHT Jena)
Katharina Menzer	*Untersuchung der Grenzfläche zwischen Kohlenstoffnanoröhre und Polymeren*
Anne-Kathrin Meyer	*Electrical properties of nanostructures*

Raphael Niepelt	*Aufbau und Betrieb eines Mikroionenstrahls für Erosionsexperimente* (extern Universität Göttingen)
Gregor Oelsner	*Auslesen von Fluß-Qubits*
Christian Pansow	*Laserdeposition von Metallen*
Christiane Präfke	*Herstellung von sub-µm Strukturen für SAW-Bauelemente durch Reaktives Ionenätzen*
Frank Richter	*Thermodynamische Untersuchungen instationärer Strömungsformen an Komponenten Übergängen*
Thomas Schönau	*Magnetfeldsensoren mit hoher Dynamik für die luftgestützte Geomagnetik*
Maik Sode	*Charakterisierung von Fluor- und Argonplasmen sowie deren Anwendung in der Beschichtungstechnik* (extern Fraunhofer Institut Jena)
Jana Sommerfeld	*Charakterisierung von einzelnen Silizium-Quantenpunkten*
Markus Trautmann	*Herstellung und Untersuchung von Metallnanoteilchen*
Sebastian Wolf	*Demonstrationsmodelle zu Problemen des experimentellen Nachweises von Gravitationswellen* (Staatsexamen)
Roland Wolters	*Entwicklung einer Testsuite zur numerischen Simulation der Konvektion im Erdmantel*
Philipp Zeigermann	*Effekte der Funktionalisierung und Behandlung auf die elektronischen Eigenschaften von Kohlenstoffnanoröhren*

Bachelor Thesis

Jens Bergner	*Modifikation einer Vakuumanlage für die lasergestützte Kohlenstoffabscheidung*
Richard Leis	*Aufbau einer Anlage zur Herstellung von Kontaktierungsschichten*
Danny v. Nordheim	*Untersuchungen zum Rekristallisation von Strontiumtitanat*
Andrea Pätzolt	*Optimierung von Lackprozessen für Ätz- und Liftprozesse*
Alexander Thieme	*Bestimmung der Ätzparameter für eine Ionenstrahlätzanlage mit Kaumanquelle*
Simon Zoch	*Aufbau einer Vakuumanlage für die Optimierung von Strontiumtitanat*

PhD-Theses

Olivier Debieu	*Optical characterization of luminescent silicon nanocrystals embedded in glass matrices*
Torsten Köttig	*Dünnschichtsysteme für die effektive Tieftemperaturregeneration*
Mario Liehr	*Validierung biomagnetischer Verfahren bei isotroper und anisotroper Volumenleitung in einem Torsophanto*m
Ronny Nawrodt	*Kryogene Gütemessung an optischen Substratmaterialien für zukünftige Gravitationswellendetektoren*
Anja Schröter (Zimmer)	*Mechanische Verluste in Materialien für zukünftige kryogene Gravitationswellendetektoren*
Daniel Stichtenoth	*Dimensionseffekte in Halbleiternanodrähten* (extern Universität Göttingen)

6. Cooperations, guests and colloquia at IFK

The Institute of Solid State Physics collaborates with a large number of Institutes and Universities in Germany and around the world and has also close connections with several companies. In the framework of these wide spread contacts in 2008 a number of scientists from various countries visited our Institute to perform experiments, discuss scientific results obtained within joint projects and to give talks in the colloquium of the Institute of Solid State Physics.

6.1 Visiting scientists

Dr. Oscar Bomati	Universidad de Zaragoza, Spain
Prof. Dr. E. Friedland	University of Pretoria, Pretoria, Süd-Afrika
Prof. Dr. P.I. Gaiduk	Staatliche Belarussische Universität Minsk, Minsk, Belarus
Dr. Bill Graham	Texas Christian University, Fort Worth, Texas, USA
Dr. Alexander Grib	Kharkov National University, Physics Department
Dr. Olivier Guillois	CEA Saclay, Paris, France
Zohair Hussain	Australian National University, Canberra, Australien
Ms. Nayla El-Kork	Université Claude Bernard Lyon 1, Lyon, France
Prof. Dr. Johan Malherbe	University of Pretoria, Pretoria, Süd-Afrika
Dr. Shantanu Rastogi	Gorakhpur University, India
Claudia S. Schnohr	Australian National Laboratory, Canberra, Australien
Dr. Yuri Shukrinov	Joint Institute for Nuclear Research, Dubna, Bogoliubov Laboratory of Theoretical Physics
Prof. Dr. N.A. Sobolev	Université Aveiro, Aveiro, Portugal
Dr. Angela Staicu	National Institute for Laser, Plasma and Radiation Physics, Bukarest, Romania

6.2 Colloquia at the Institute of Solid State Physics

PD Dr. Konrad Gärtner (Universität Jena), 18.01.2008
MD-Simulation zur Defektakkumulation in Halbleitern

PD Dr. Carsten Ronning (Universität Göttingen), 08.02.2008
Ionenstrahlen und Nanostrukturen

Prof. Dr. W. Bolse (Universität Stuttgart), 09.05.2008
Instabilität und Musterbildung in dünnen Schichten bei hochenergetischer Ionenbestrahlung

Dr. Wolfgang Vodel (Universität Jena), 16.05.2008
SQUIDs für die Präzessionsmesstechnik

Prof. Dr. H. Kroemer (University of California), 19.05.2008
Heterostrukturen: Schlüsseltechnologie der Halbleiterphysik

PD Dr. Elke Wendler (Universität Jena), 30.05.2008
Experimentelle Untersuchungen zur Defektakkumulation in Halbleitern und ausgewählten Isolatoren
Christian Borschel (Universität Jena), 06.06.2008
Analyse von dünnen Schichten und deren Grenzflächen mit hochauflösender RBS

PD Dr. Silke Christiansen, (IPHT Jena), 18.07.2008
Herstellung und Charakterisierung von Silizium-Nanodrähten

Dr. Joachim Albrecht (Max-Planck-Institut Stuttgart), 20.06.2008
Magnetische Lawinen in Supraleitern

Dipl.-Ing. Hendrik Albrecht (ECM Engineering - Consulting & Management Ltd. Grünheide), 11.07.2008
Wechselstromtomografie - eine neue Methode für biomagnetische Untersuchungen und zerstörungsfreie Werkstoffprüfung

Dr. Tobias Voss (Universität Bremen), 07.11.2008
Zincoxid Nanowires - Material Properties and Nanophotonic Devices

Dr. Reiner Klenk (Helmholtz-Zentrum Berlin), 21.11.2008
Material Properties and Design of Chalcopyrite-Based Solar Cells and Modules

Prof. Dr. M. Schilling (TU Braunschweig), 05.12.2008
Magnetische Nanopartikel für Anwendungen in biochemischer Analytik und medizinischer Diagnostik

7. Teaching activities

7.1 Lectures

Ergänzende Kapitel der Festkörperphysik WS 2007/08 (Wahlpflichtvorlesung)	PD Dr. F. Schmidl
Experimentalphysik für Mediziner und Biochemiker WS 2007/2008,	Prof. Dr. W. Richter
Experimentalphysik IV: Struktur der Materie II (Physik-Diplom, Physik-Lehramt) SS 2008 (Wahlpflichtvorlesung)	Prof. Dr. P. Seidel
Experimentalphysik (Biologen,Ernährungswissenschaftler, Pharmazie, Biogeo) WS 2007/2008, WS 2008/2009	Prof. Dr. W. Wesch
Festkörperanalyse mit energiereichen Teilchen WS 2007/2008 (Wahlvorlesung)	Prof. Dr. W. Wesch, PD Dr. K. Gärtner, Dr. F. Schrempel
Halbleiter-Optoelektronik WS 2007/2008	Prof. Dr. W. Richter
Kern- und Elementarteilchenphysik (für Lehramt und techn. Physiker) SS 2008	Prof. Dr. C. Ronning
Kern- und Elementarteilchenphysik SS 2008	Prof. Dr. W. Wesch
Modul: Elektronik WS 2007/2008	PD Dr. F. Schmidl, Dr. W. Vodel
Modul: Exphysik I, Grundkurs Mechanik, Wärme SS 2008, WS 2008/09	Prof. Dr. C. Ronning
Modul: Exphysik I, Grundkurs Mechanik, Wärme WS 2007/2008	Prof. Dr. P. Seidel
Modul: Festkörperphysik SS 2008, WS 2008/2009	Prof. Dr. P. Seidel
Modul: Grundkurs Physik der Materie II WS 2007/08, SS 2008, WS 2008/2009	Prof. Dr. P. Seidel
Modul: Messtechnik WS 2007/2008, SS 2008, WS 2008/2009	PD Dr. F. Schmidl
Modul: Physik der Materie I WS 2007/2008, WS 2008/2009	Prof. Dr. W. Wesch
Nanophysik II: Nanoteilchen SS 2008	Prof. Dr. Fr. Huisken
Solarzellen- Grundlagen und Materialaspekte WS 2007/2008	PD Dr. H. Metzner

Wahlmodul: Optoelectronics WS 2007/2008	Prof. Dr. W. Richter
Wahlmodul: Supraleitung WS 2007/2008, WS 2008/2009	Prof. Dr. P. Seidel
Tieftemperaturphysik- und –technik SS 2008	Prof. Dr. P. Seidel, Dipl.-Ing. M. Thürk
Photovoltaik: Elektrische Energie aus Sonnenlicht Öffentliche Samstagsvorlesung 22.11.2008	PD Dr. H. Metzner

7.2 Seminars

Einführung in die Festkörperphysik WS 2007/2008, WS 2008/2009	PD Dr. F. Schmidl, Dipl.-Ing. M. Büttner
Elektronik (Lehramtsstudenten) WS 2007/2008, SS 2008, WS 2008/2009	Dr. W. Vodel
Elektronik WS 2007/2008, SS 2008, WS 2008/2009 (Physik-Diplom und Informatik)	Dr. W. Vodel, PD Dr. F. Schmidl
Ergänzende Kapitel der Festkörperphysik Materialwissenschaftler 5. Semester WS 2007/2008 (Wahlpflichtseminar)	PD Dr. F. Schmidl, Dipl.-Ing. M. Büttner
Experimentalphysik I für Physiker SS 2008	PD Dr. E. Wendler
Experimentalphysik I für Physiker WS 2007/2008	Dr. Ch. Hülsen
Experimentalphysik II für Physiker WS 2007/2008, SS 2008, WS 2008/2009	PD Dr. E. Wendler
Experimentalphysik II: Grundkurs Elektrizität, Optik WS 2007/2008, WS 2008/2009	Dr. F. Schrempel
Festkörperphysik.Nanomaterialien WS 2008/2009	Prof. Dr. C. Ronning, Dr. B. Schröter, PD Dr. F. Schmidl
Grundkurs Physik der Materie II WS 2007/2008	PD D. Schmidl
Institutsseminar WS 2007/2008, SS 2008, WS 2008/2009	Prof. Dr. P. Seidel
Kerne und Teilchen SS 2008	PD Dr. K. Gärtner
Nanostrukturen und Kohlenstoffnanoröhren WS 2007/2008, SS 2008,	Dr. B. Schröter, PD Dr. F. Schmidl
Nukleare Festkörperphysik WS 2007/2008, SS 2008, WS 2008/2009	Prof. Dr. W. Wesch

Physik der Materie I SS 2008	PD Dr. E. Wendler
Physik der Materie I WS 2007/2008	PD Dr. K. Gärtner
Physik für Biogewissenschaftler WS 2007/2008, WS 2008/2009	PD Dr. E. Wendler
Proseminar zum Fortgeschrittenenpraktikum WS 2007/2008, SS 2008, WS 2008/2009	Dr. B. Schröter
Tieftemperaturphysik und Supraleitung WS 2007/2008, SS 2008, WS 2008/2009	Prof. Dr. P. Seidel

7.3 Practica

Elektronikpraktikum WS 2007/2008, SS 2008, WS 2008/2009	Dr. W. Vodel (Leitung), PD Dr. F. Schmidl,
Fortgeschrittenen-Praktikum WS 2007/2008	Dr. B. Schröter (Leitung) Prof. Dr. C. Ronning
F-Praktikum (Kernphysik) WS 2007/2008, SS 2008, WS 2008/2009	Dr. U. Reislöhner, Dr. F. Schrempel
Grundpraktikum WS 2007/2008, SS 2008, WS 2008/2009	Prof. Dr. W. Wesch,
Messtechnik WS 2007/2008, SS 2008, WS 2008/2009	PD Dr. F. Schmidl, Dipl.-Ing. R. Neubert
Weihnachtsvorlesung WS 2007/2008	Prof. Dr. P. Seidel, Prof. Dr. W. Wesch
Weihnachtsvorlesung WS 2008/2009	Prof. Dr. C. Ronning Prof. Dr. W. Wesch

8. Personnel

Professors

Prof. Dr. habil. Carsten Ronning
Prof. Dr. habil. Wolfgang Richter (to 03/08)
Prof. Dr. habil. Paul Seidel (director)
Prof. Dr. habil. Werner Wesch
Prof. Dr. habil. Friedrich Huisken

Scientific Staff

PD Dr. habil. Konrad Gärtner
PD Dr. habil. Heinrich Metzner
PD Dr. habil Frank Schmidl
PD Dr. habil. Elke Wendler
Dr. Janko Cieslak
Dr. Jens Eberhardt (to 07/08)
Dr. Olivier Debieu
Dr. Ernst Glaser
Dr. Thomas Hahn (to 07/08)
Dr. Christian Hülsen (to 04/08)
Dr. Cornelia Jäger
Dr. Sergiy Krasnokutskiy
Dr. Libo Ma
Dr. Ronny Nawrodt
Dr. Sandor Nietzsche
Dr. Udo Reislöhner
Dr. Gaël Rouillé
Dr. Frank Schrempel
Dr. Bernd Schröter
Dr. Wolfgang Vodel

PhD Students

Marco Arold
Daniel Baumgarten (Biomagn. Zentrum)
Christoph Becker
Christian Borschel
Markus Büttner
Sebastian Geburt
Rene Geithner
Thomas Gischkat
Veit Große
Mathias Hädrich
Stefan Hechler (to 07/08)
Daniel Heinert
Christian Kraft
Mario Liehr (Biomagn. Zentrum)
Ronny Nawrodt
Raphael Niepelt
Michael Oertel
Katja Peiselt (IPHT Jena)
Jakob Reinisch
Kerstin Riedel (Fritz-Lipmann Institut)
Christian Schwarz
Tobias Steinbach
Michael Steinert
Mathias Steglich
Alexander Steppke

Diploma Students

Michael Blech
Sebastian Engmann
Martin Gnauck
Stefan Goetz
Robert Hähle
Christoph Heisler
Manuela Janietz
Hans Kleemann
Peter Kossebau
Michael Kotzlik
Stefanie Kroker
Pascal Macha
Katharina Menzer
Anne-Katrin Meyer
Gregor Oelsner
Christian Pansow
Peter Queitzsch
Frank Richter
Torsten Schmidt
Johannes Slotta
Jana Sommerfeld
Markus Trautmann
Reinhard Volkmer
Alexander Voigt (Strahlentherapie)
Martin Voitsch (BATOP GmbH)
Johannes Wagner
Mathias Weiß (OSRAM Opto)
Christian Wolf
Philipp Zeigermann
Gabriel Zieger

Technical Staff

Ulrich Barth
Uta Bornkessel
Uwe Eberhardt
Lutz Föllmer
Silke Frunzke (0,75)
Kristina Garlipp (0,5)
Dieter Hasler
Torsten Hilprecht
Frank Jehn
Gerald Lenk
Holger Mühlig
Anja Mittelstädt (0,9)
Ralf Neubert
Stefan Prass
Helga Rudolph
Sylvia Stender (0,75)
Matthias Thürk
Carmen Voigt